The Albedo Climate Effect of PV Systems

The bright side of solar energy

A.M.Schiereck

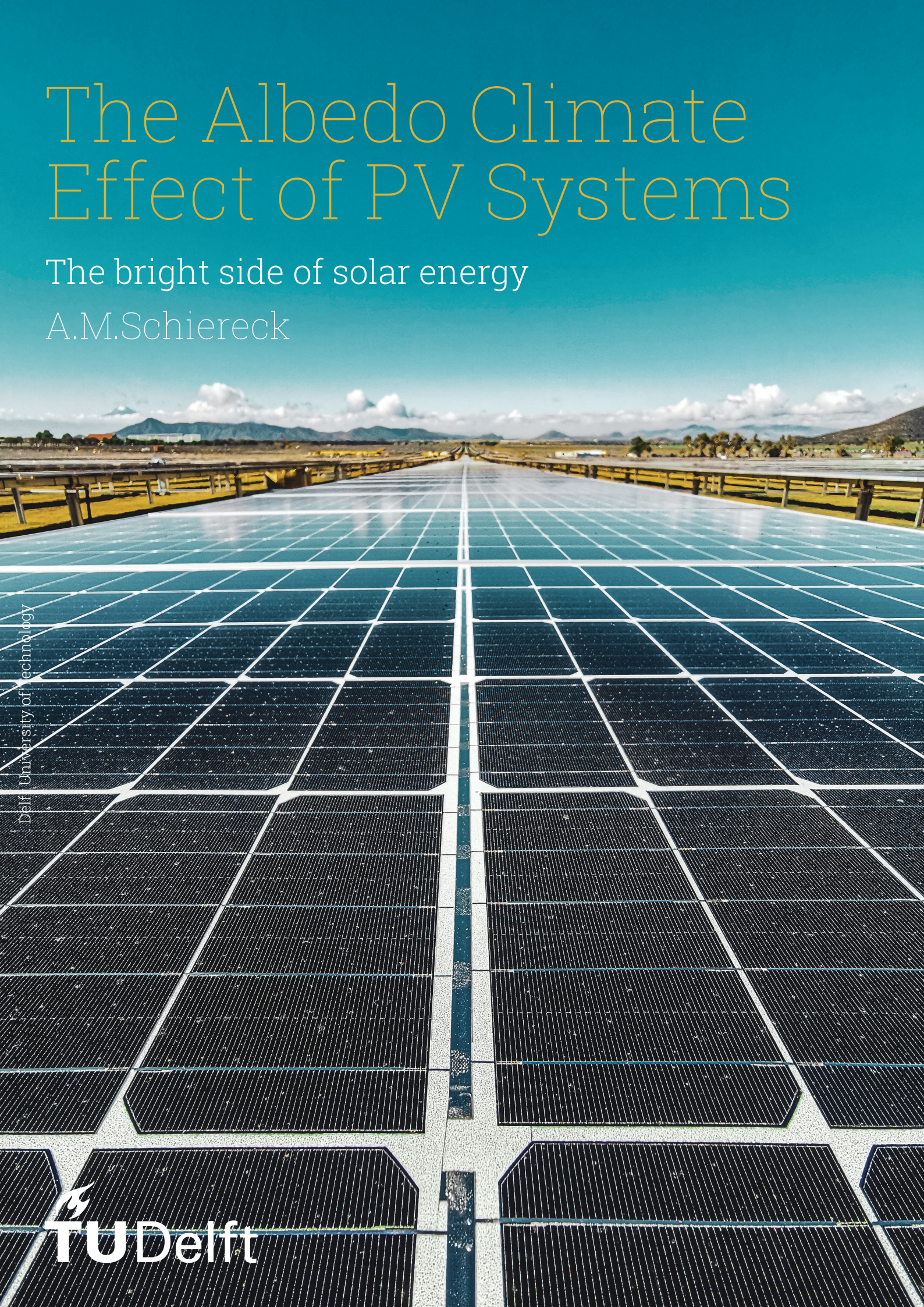

Delft University of Technology

TU Delft

The Albedo Climate Effect of PV Systems

The bright side of solar energy

by

A.M.Schiereck

to obtain the degree of Master of Science
at the Delft University of Technology.

Student number:	4612280	
Project duration:	April, 2025 – March, 2026	
Thesis committee:	Prof. dr. A. H. M. Smets,	EWI, TU Delft
	Dr. M. R. Vogt,	EWI, TU Delft
	Y. Blom,	EWI, TU Delft
	Prof. dr. ir. H. W. J. Russchenberg	CiTG, TU Delft
Research initiator:	Dr. H. Ziar	

Cover:	SEIA Solar + Storage dictionary cover, Adobe Stock by Jesus
Style:	TU Delft Report Style, with modifications by Daan Zwaneveld

An electronic version of this thesis will be available at `http://repository.tudelft.nl/`.

TU Delft

Abstract

As solar farms supply an increasing share of electricity, comprehending their overall impact on climate is becoming ever more critical. Solar farms typically alter the surface reflectance, as their reflective properties differ from those of the original ground where they are installed. However, in life cycle assessments, the climatic effects of surface albedo changes resulting from the installation of solar farms are not considered. Therefore, this research aims to determine the albedo-climate effect of solar farms globally. Since earlier studies did not account for solar farm degradation or the effective albedo, these factors will be included in this analysis.

In the first part of this research a model was developed to determine the surface albedo. The model relies on Sentinel-2 satellite imagery to obtain information on surface reflectance. The albedo is calculated using a linear combination of the available spectral bands. To validate this albedo estimation approach, radiative flux data from SURFRAD measurement station in the USA were employed. The results show that the model produces albedo estimates with a RMSE of 0.032. A bias correction was developed that depends on the solar zenith angle at the time the Sentinel-2 image was acquired. The bias correction was theoretically derived from the data and the anticipated error introduced by the assumption that the surface reflection is Lambertian. With this correction applied, the albedo estimation RMSE was reduced to 0.021. The findings highlighted how the Lambertian assumption affects the outcomes and confirmed that applying a bias correction is appropriate for improving the accuracy of the albedo estimates.

The second model developed in this study quantifies how albedo is altered by the installation of solar farms. The location of 500 solar farms were sourced from the Solar Asset Mapper dataset developed by Transition Zero. For the albedo change, the difference between the albedo of the PV area and that of the surrounding area is used. Google Earth Engine was employed to simplify satellite image processing and enhance computational capacity. The mean albedo difference observed was -0.0198. Seasonal variation in the PV region's albedo was detected, indicating that the solar farm boundaries are incorrectly defined, causing the surrounding area's seasonality to be introduced into the PV albedo. In addition, the results revealed problems associated with glare.

In the third model, the climatic impact of the albedo changes of solar farms was assessed. To remove low-quality measurements, for example those distorted by glare, the dataset was cleaned before conducting further analysis, resulting in a total of 157 farms. Here, the effective albedo of the PV area was calculated, and both the absolute and effective changes in albedo were applied throughout the remainder of the model. On average an absolute albedo change of -0.0299 and effective albedo change of 0.0496 was found for these 157 farms. The radiative forcing caused by the albedo change was calculated with the use of a radiative kernel dataset. The radiative forcing associated with the solar farm's avoided emissions was estimated based on the local electricity carbon intensity. The net radiative forcing was then obtained by the sum of these contributions together with the radiative forcing from embodied emissions. Based on this net radiative forcing, the carbon break-even time was determined for each farm. On average, a carbon break-even time of 7.79 yr was found when considering the absolute albedo change, whereas a much shorter average carbon break-even time of 0.41 yr was obtained for the effective albedo change. These results indicate that the effective albedo exerts a cooling, rather than warming, effect on the climate, thereby reducing the overall climate impact of solar farms.

AI statement

In preparing this text Writefull was used in Lateχ for paraphrasing suggestions. For python coding ChatGPT and GitHub Copilot were used.

Contents

1 Introduction

Climate change is the greatest challenge of our generation. Its consequences affect societies, economies, and ecosystems across the globe. As greenhouse gas (GHG) emissions continue, climate related extreme events will become increasingly complex and cascade across sectors and regions. However, the risks associated with climate change depend strongly on adaptation and mitigation policies [1]. Therefore, the United Nations (UN) agreed to limiting the rise in the global average temperature to 1.5 °C in the Paris Agreement [2].

Reaching the goals of the Paris Agreement requires substantial decarbonization of the global energy system. To do so, the Intergovernmental Panel on Climate Change (IPCC) determined that the net global CO_2 emissions in 2030 should be reduced to 48% of the modelled 2019 emissions [3]. Therefore, carbon-intensive energy sources like fossil fuels should be replaced with renewable energy sources. Solar energy is among the renewable energy sources with the highest potential for energy generation [3] [4]. Therefore, solar energy is a highly suitable candidate for decarbonising the energy mix.

Additionally, nearly all of the energy humans consume ultimately originate from the sun [5]. Through photosynthesis, solar energy is transformed into chemical energy stored in biomass, which in turn is the original source of coal, oil, and gas. Hydro power and wind energy also find their origin in the solar radiation trough evaporation and non-uniforms heating respectively. Electricity generation with photovoltaic (PV) panels is the most direct way to utilize the sun's radiative power.

However, all power plants, independent of their energy source, have an environmental impact [6]. Fossil fuel-based power generation releases greenhouse gases during the actual production of energy, whereas for PV and most other renewable energy sources, the majority of greenhouse gas emissions occur mainly during the manufacturing stage. Therefore PV based electricity is associated with a lower environmental impact [7] [8]. However, because PV-based electricity generation requires extensive land areas, it also alters the Earth's surface. These alterations to the Earth's surface are likewise linked to environmental impacts.

Between 2000 and 2024, the global installed PV capacity has increased exponentially, and has reached approximately 1.5 TW in 2024 [9] [10] [11]. As the overall installed PV capacity grows, the associated environmental impact also increases. Therefore, gaining a comprehensive understanding of the environmental effects of solar farms has become ever more important. In a life cycle analysis, the carbon footprint as well as the carbon intensity of the electricity produced, of a solar panel is determined. However, these analyses do not take into account how land-use changes from solar farm deployment influence the global energy flux balance and, in turn, the climate. In this study, we model how large-scale deployment of solar farms alters the global energy flux balance and analyse the resulting impacts of this change on the climate.

This chapter presents the theoretical background of this research. First, the theory of climate physics and solar energy relevant for the effect of land-use change on climate is presented. Next, the albedo-climate effect is defined, and the metric of radiative forcing is explained. To illustrated the relevance of the albedo-climate effect for solar farms, it's scale is determined. In addition, previous work is presented together with the research gap. And finally, the research questions addressed in this thesis are stated.

1.1. Climate & Radiation

The Sun continuously supplies radiant energy to Earth. If the Sun is modelled as an ideal black body, the power it radiates from its surface is given by the Stefan–Boltzmann law. This law is given in equation 1.1[12]. To determine the solar radiative power incident at the top of Earth's atmosphere (TOA), the Stefan–Boltzmann law must be adjusted by a scaling factor. This factor, obtained from the equation for the surface of a sphere, is given by $\left(\frac{r_{s,e}}{R_{sun}}\right)^2$. Here, R_{sun} is the sun's radius and $r_{s,e}$ represents the average distance from the centre of the sun to the centre of the Earth. For the sun an average surface temperature of about 5800 K is assumed [13], which results in an incident solar flux at the TOA of approximately 1361 W/m^2. This value is also referred to as the solar constant [14].

$$P = \sigma T^4 \tag{1.1}$$

The parameters and constants in equation 1.1 are as follows:

- P is the radiant power emitted by a surface in W/m^2.
- σ is the Stefan-Boltzmann constant in $W/(m^2K^4)$.
- T is temperature in K.

The Earth's climate is governed by the atmospheric energy balance. In this balance the TOA solar radiation provides the energy influx. A schematic of the average atmospheric energy balance is shown in Figure 1.1. In yellow the incoming shortwave radiation from the sun is shown. The value of the incoming radiative energy is the total incident radiative energy averaged over the surface of the Earth. The total incident radiative energy is calculated by multiplying the solar constant by the cross-sectional area of the Earth. Dividing this total incident radiative energy over Earth's surface area yields the average incoming radiative flux of roughly 340 W/m^2. The incident shortwave radiation at the TOA is either absorbed by the atmosphere or the surface, or is reflected by the clouds or the surface. Albedo is defined as the fraction of radiative energy that is reflected of a surface (α) [5]. With a higher albedo, less energy enters the atmospheric energy balance [14][15]. The part of the incident shortwave radiation that is not reflected by the surface, is transmitted or absorbed. The fraction of incident radiation that is absorbed is called the absorptance (A) [12]. The absorbed radiation heats the surface of the Earth.

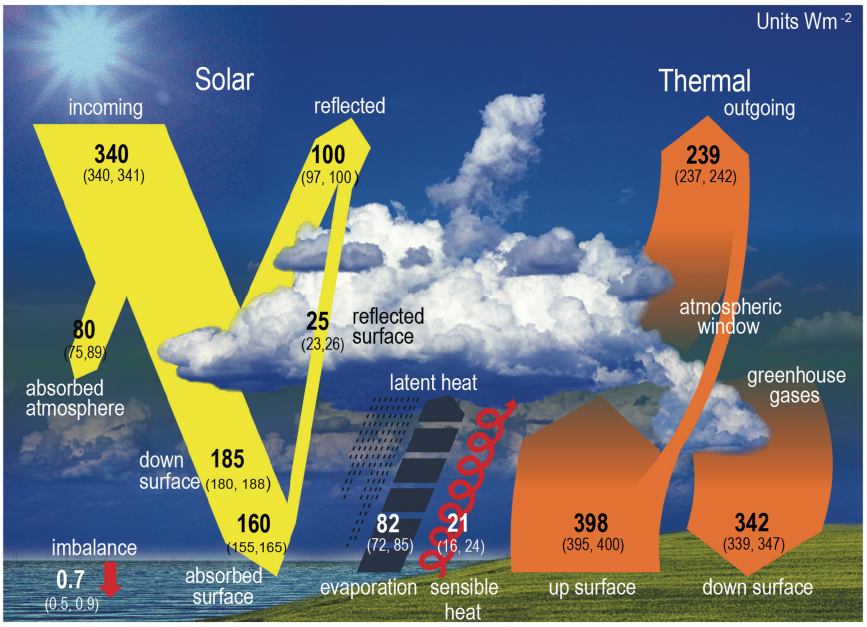

Figure 1.1: A schematic of the energy balance of the atmosphere indicating shortwave radiation in yellow, longwave radiation in orange, latent heat in dark grey and sensible heat with a curling red arrow. The imbalance in the system, which causes the atmosphere to heat, is indicated with a red downward arrow. The energy fluxes are given in units of W/m^2. The figure is adapted from IPCC Assessment Report 6 [16, p. 934].

The Earth emits radiation primarily in the longwave spectrum. Using the Stefan–Boltzmann equation (1.1) and assuming a mean surface temperature of 15 °C, the resulting upward radiative flux from Earth's surface is about $398\,W/m^2$. In the energy balance shown in Figure 1.1, the thermal longwave radiation is indicated in orange. Most of the upward thermal radiation emitted by the surface is absorbed in the atmosphere by greenhouse gases (GHGs) [14] [15]. These GHGs then release the thermal radiation again, sending part of it upward and out of the atmosphere into space, as shown in Figure 1.1 as outgoing. The remaining portion is radiated back toward the Earth's surface, which is shown in the figure as the downward surface component. The atmosphere releases more energy toward the surface than it does toward space. This follows from the fact that the atmosphere is best described as a stack of horizontal layers. Each layer emits an equal amount of radiation upward and downward, which is then absorbed by the neighbouring layers. Because the Earth's surface provides the thermal energy for these layers, their temperature decreases with increasing height. As a result, the top layer releases less radiation upward out of the atmosphere than the bottom layer emits downward back toward the surface.

As a result of human-generated GHG emissions, the amount of downward surface radiation increases and the atmospheric energy balance becomes unbalanced. This imbalance is illustrated in Figure 1.1 by a red downward arrow. As a result, the Earth's surface warms, which increases the upward longwave radiation from the surface until the energy balance is re-established with a higher surface temperature. [14] [15]

The values for incident solar radiation and for upwelling surface radiation shown in Figure 1.1 do not exactly match those determined above. This difference arises from the fact that the values shown in Figure 1.1 are based on measurements, while those obtained from the Stefan–Boltzmann equation represent theoretical estimates. The Stefan–Boltzmann equation describes objects that behave as ideal blackbodies. However, in reality, neither the sun nor the Earth acts as a perfect blackbody. Furthermore, the Stefan–Boltzmann equation is non-linear. Consequently, for a non-uniform surface, the computed mean radiation will differ depending on whether the average is taken of the emitted radiation directly or the average is taken of the surface temperature before the equation is applied.

1.2. Solar Energy

The sun radiates energy over a continuous spectrum. The spectrum of a blackbody is described by Planck's law, as given in equation 1.2 [17] [12]. Integrating Planck's law over λ yields the Stefan-Boltzmann equation. In Figure 1.2 the approximated solar spectrum scaled to the TOA is shown. Additionally, Figure 1.2 shows the measured spectrum of the sun on the surface of the Earth after passing trough 1.5 times the height of the atmosphere (AM1.5) [18] [19]. The difference between the two spectra is due to the blackbody assumption in Planck's law and due to the interaction of the atmosphere with radiation.

$$P_\lambda = \frac{2\pi hc^2}{\lambda^5} \frac{1}{e^{\frac{hc}{\lambda k_B T}} - 1} \tag{1.2}$$

The parameters and constants in equation 1.2 are as follows:

- P_λ is the spectral radiant power emitted by a surface in $\mathrm{W/m^3}$.
- h is Planck's constant in $\mathrm{J \cdot s}$.
- c is the speed of light in vacuum in m/s.
- λ is the wavelength in m.
- k_B is the Boltzmann constant in J/K.
- T is temperature in K.

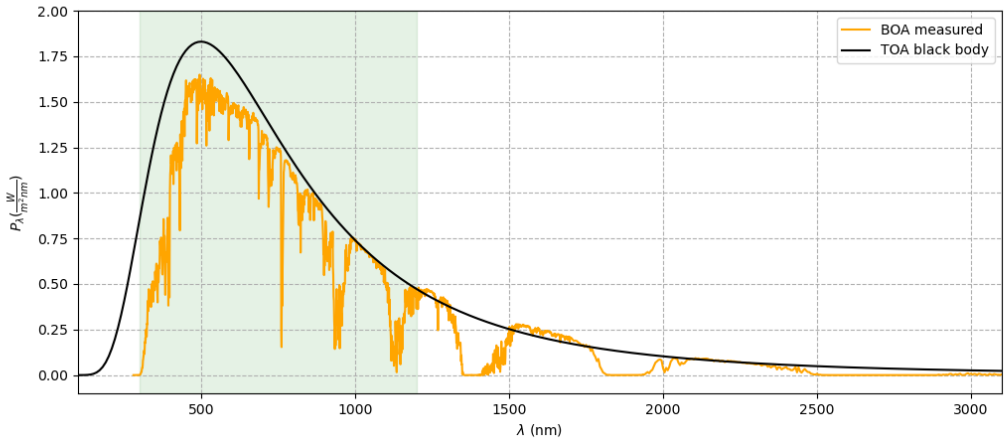

Figure 1.2: The black body radiation spectrum of the sun at the top of the atmosphere (TOA) and the measured global solar spectrum at the surface, or bottom of the atmosphere (BOA). TOA spectrum indicated in black and the BOA spectrum in yellow. BOA spectrum radiation is measured after passing trough 1.5 times the absolute air mass (AM1.5) [18] [19]. The green region indicates the photovoltaic active spectral range [20] [5].

Solar panels convert the radiative energy of the sun into electrical energy. The active layer in PV devices is made up out of semiconductor material. A photon, which is a packet of radiative energy $E_{photon} = \frac{hc}{\lambda}$, with sufficient energy creates an electron hole pair in the active layer of the solar cell. If the active layer is electrically connected the electrons and holes can be extracted and a current starts to flow. Consequently, to optimise electricity generation, PV devices are designed to have a low albedo, as to absorb as much photons as possible. In figure 1.2 the active range of PV devices is indicated as well [5] [20].

1.3. Albedo-Climate Effect

Solar farms influence the climate in several ways. In a life cycle analysis (LCA) the environmental impact of solar panels is determined based on factors like raw material used and their supply chain, water use, energy use, manufacturing, mounting, cables, inverters and all other components needed to produce electricity [21] [22, 23]. The results of a LCA is often expressed in the carbon intensity of electricity in g/kWh (CO_2-eq). Because the carbon intensity of electricity generated by solar farms is low, the GHG emissions associated with electricity production are reduced. As a result, the downwelling surface radiation decreases, as illustrated in Figure 1.1. This process reduces the Earth's energy imbalance, reducing climate warming.

Another way in which the deployment of large-scale solar farms affects the climate is through changes in the Earth's surface albedo. However, this influence is usually not included in LCA. As solar panels are designed to have a low albedo, the Earth's surface albedo is generally decreased by solar farms. A lower albedo decreases the reflected solar radiation, increasing the absorbed surface radiation, as illustrated in Figure 1.1. This effect increases the Earth's energy imbalance, leading to climate heating. This consequence of a change in albedo on the climate is called the albedo-climate effect [24].

However, not all of the energy absorbed by a solar panel is directly converted into heat, as with other surfaces. A portion of the energy is converted to electricity, depending on the panel's efficiency (η). Eventually all electricity will enter the atmospheric energy balance as dissipated heat. However, when the environmental impact of electricity generation is determined, only the means of generation are accounted for, the impact of electricity itself is not considered. Therefore, when determining the albedo-climate effect of solar farms, the effective albedo (α_{eff}) should be used [25]. The effective albedo accounts both for the fraction of energy that is converted into electricity as well as the reflected fraction [26]. The effective albedo is described in equation 1.3. In this equation η_{annu} is the solar conversion efficiency, which describes the annual average efficiency from sunrise to sunset. This will be discussed in further detail in Chapter 4.

$$\alpha_{eff} = \alpha + \eta_{annu} \tag{1.3}$$

1.4. Radiative Forcing & Carbon Break Even Time

To compare the influence of different climate factors, such as albedo and CO_2 emissions on the atmospheric energy balance, radiative forcing (RF) is used. Radiative forcing describes the net change in the atmospheric energy balance as a result of a perturbation in the system [14] [27]. RF is expressed in W/m^2, where a positive value indicates a reduction in outward radiation, and thus a warming of the atmosphere. In contrast, a negative value indicates a cooling effect [14]. The RF that results from a change in albedo can be calculated with equation 1.4 [24]. In this equation, the albedo change radiative kernel is a monthly variable that quantifies the response of the energy balance to a change in albedo [28].

$$RF_{\Delta\alpha} = \frac{\sum_{m=1}^{12} k_{\Delta\alpha}\Delta\alpha_m}{12}\frac{A_{PV}}{A_E} \tag{1.4}$$

The parameters and constants in equation 1.4 are as follows:

- $RF_{\Delta\alpha}$ is the RF due to a change in albedo in W/m^2.
- $k_{\Delta\alpha}$ is the monthly climatological albedo change radiative kernel in W/m^2.
- $\Delta\alpha_m$ is the average monthly change in albedo.
- A_{PV} is the area of the PV farm.
- A_E is the surface area of the Earth.

The RF due to the replacement of GHG emissions can be calculated with equation 1.5 [29] [30] [24].

$$RF_{CO_2}(t) = k_{CO_2} \int_{t'=0}^{t'=t} E_{CO_2}(t') IRF_{CO_2}(t - t') dt' \tag{1.5}$$

The parameters and constants in equation 1.5 are as follows:

- $RF_{CO_2}(t)$ is the RF due to the replacement of CO_2 emissions in W/m^2 as a function of time.
- k_{CO_2} is the RF of 1 kg of CO_2 at a given background concentration.
- E_{CO_2} is the amount of CO_2-eq emissions, in kg, reduced through electricity generation by PV farms.
- IRF_{CO_2} is the impulse-response function of the CO_2 emissions [30].

The RF due to the albedo change is instantaneous and therefore, after installation, a constant over time. While the RF due to the avoided CO_2 emissions is cumulative due to the long atmospheric lifetime of CO_2 and is therefore a function of time [24]. If the radiative forcing due to the albedo change is positive, heating the climate, the carbon break-even time (CBET) can be determined. The carbon break-even time is the time it takes for the negative radiative forcing due to the solar to offset the the positive radiative forcing [24].

1.5. Scale of the Albedo-Climate Effect

Because the albedo–climate effect is generally not considered in LCA, its overall magnitude remains relatively poorly investigated. Therefore, an order-of-magnitude estimate calculation was done as to estimate the relevance of the effect. In the calculations the albedo change due to large scale solar farms of 0.0128 reported by Wei et al. was used [31]. This change in albedo is equivalent to approximately 2.5 g/kWh (CO_2-eq. Appendix A shows the steps and assumptions which led to this approximation. For context, the carbon intensity of electricity of solar panels is approximately 22 g/kWh (CO_2-eq) [22]. This means the climatic effect of albedo change is in the order of 10% of that associated with PV module production.

In recent years, the carbon intensity of PV farms has decreased significantly [32]. With improvements such as increased module efficiency, enhanced manufacturing processes, and reduced material use, the carbon intensity of PV modules is expected to continue to decline [23], while the albedo penalty will remain unchanged. Consequently, the relative significance of the albedo–climate effect is expected to increase, underscoring the relevance of this research.

1.6. Previous Work & Research Gap

The estimation of albedo from satellite observations has widely been studied, primarily in the field of climate monitoring [33][34][35][36][37][38]. Changes in urban albedo resulting from the installation of PV panels have previously been examined by Zhou et al. [39]. Furthermore, a previous analysis of the impact of solar farms on surface temperature found a reduction in albedo of 0.036 [40]. Yet, that same study also documented an increase in effective albedo of 0.024. In addition, two studies were found that examine global changes in albedo caused by large-scale solar farms, using satellite data.

Xu et al. found a decrease in the annual mean surface shortwave albedo of 0.016 due to the installation of 116 large solar farms [25]. Their research did not account for either the effective albedo or PV panel degradation. Wei et al. found a slightly smaller albedo decrease with a median of 0.0128 based on 352 PV facilities globally [31]. In the study by Wei et al., changes in carbon sequestration caused by PV deployment were not considered. However, the authors stated that these effects cannot be regarded as negligible.

Both Xu et al. and Wei et al. combine PV farm data used to select the locations under consideration with satellite data to determine albedo. Xu et al. utilise the Wiki-Solar database [41]. This database is based on information from local organisations and governments and includes only solar farms with capacities greater than 40 MW. Furthermore, this dataset is updated monthly. However, it is not publicly available. Wei et al. utilise the solar farm dataset developed by Kruitwagen et al. [42]. This database was created with satellite imagery to detect solar farms through machine learning. However, it represents a snapshot of the situation at the end of 2018 and has not been updated since. In addition, not all detected solar farms in this dataset include an installation date. Both Xu et al. and Wei et al. use the NASA MODIS satellite images. The MODIS satellite has pixels of 500 m x 500 m. The satellite pixel size dictates the minimal PV farm size that can be considered in the analysis. Furthermore, the MODIS satellite has a 16-day temporal resolution.

In the current literature, estimates of the albedo-climate effect are already available. However, the impact when the effective albedo is considered and PV panel degradation has not yet been thoroughly examined in these studies. In previous analyses, the generation of electricity by PV farms has been compared with that from coal-fired power plants rather than local carbon intensity. This could lead to an underestimation of the relative effect of PV farms on climate. Additionally, the change in carbon sequestration as a result of PV farm deployment was not accounted for in these studies.

In previous work, the data used has also been a limiting factor. The satellite images used were coarse-resolution, which only allowed hundreds of the largest PV farms globally to be considered, while thousands are available in the datasets. The PV farm datasets in the previous studies were also limited. Either because the data was not being updated, or because the set only contains a small part of the total number of deployed PV farms globally.

1.7. Research Question & Goals

The research question of this thesis is:

What is the climate impact of the albedo change due to solar farms considering the effective albedo and how does this relate to other solar farm related climate impacts?

The research goal of this study, in order to address this research question, is:

To determine the albedo-climate effect of solar farms globally via satellite albedo estimation considering the effective albedo and solar panel degradation.

This goal has been divided into several more specific research sub-goals:

- Develop a model to determine the albedo anywhere on Earth's land surface at a small resolution.
- Develop a model with recent PV data to determine the change in albedo due to the deployment of a solar farm. The model will be easily updated when new solar farm data is available.
- Develop a model to estimate and analyse the albedo-climate effect of solar farms globally, that considers the effective albedo and the local carbon intensity of electricity.

1.8. Report Outline

This report is divided into the following chapters. In chapter 2, the model to determine the surface albedo will be presented. The model's results will be given and discussed. Next, in chapters 3, the model to determine the change in albedo will be presented, and different methods to do so will be discussed, and will include results. Following in chapter 4, the final model to determine the albedo-climate effect is presented. The method in which the effective albedo and PV degradation are considered will be discussed. Finally, the conclusions and recommendations of this research will be presented.

2

Albedo Model

In this chapter, the first research sub-goal is addressed: The development of a model to determine the albedo anywhere on Earth's land surface at a fine spatial resolution. The first section discusses the input data used in the model. Followed by the explanation of the procedure for deriving albedo from the input data. The next section presents the verification methods used to assess the model's accuracy. Finally, the chapter concludes with the results and key findings of the albedo model.

2.1. Input Satellite Data

For the albedo model, Sentinel-2 (S2) satellite data was used as input . The use of satellite data enabled a consistent determination of albedo for many locations distributed across the Earth's land surface and over an extended time period [43][44]. The Sentinel-2 satellites are operated as part of a program managed by the European Space Agency (ESA) [45]. Appendix Table B.1, presents a comparison of Sentinel-2 with other satellites that were considered for this study.

While earlier studies relied on satellite products with a 16-day temporal resolution, the 5-day resolution of the S2 dataset allows for the possibility of significantly more observations per month. Furthermore, the fine spatial resolution of 10 m enabled the estimation of albedo for much smaller geometries than was possible with the 500 m resolution used in earlier work. In addition, the direct availability of a surface reflectance product without the need for additional data favoured the S2 products. This section provides additional details on the Sentinel-2 satellites and their associated products.

Table 2.1 presents various key numbers and characteristics of the S2 mission [43]. To derive albedo with high accuracy, a large number of observations is required. Since images acquired under cloudy, hazy, or snowy conditions may be unsuitable, the short revisit cycle of the Sentinel-2 satellites provides a high probability of obtaining usable imagery. Furthermore, the sensors on board the S2 satellites use a push-broom principle to image the Earth's surface. With this principle, the sensor uses the satellite's forward motion to continuously bring new rows of the surface into view. Each satellite can capture a strip of the Earth's surface with a width of 290 km in a single pass, known as the swath [43]. Moreover, this scanning approach maintains a constant maximum view zenith angle (ϕ_{VZ}). The zenith is the vertical pointing up through a surface or point of interest, and therefore the view zenith angle is defined as the angle between the zenith and the line connecting the sensor to a point of interest [14]. With an average altitude of 786 km, and the assumption of a flat Earth surface across the swath, the resulting maximum VZA is approximately 11°. Appendix B, Figure B.1, presents a map illustrating the areas covered by the satellites.

Table 2.1: Sentinel-2 mission specifications [43].

Parameter	Information
Satellite Sentinel-2B	Launched in 2017, operational
Satellite Sentinel-2C	Launched in 2024, operational
Revisit cycle	5-day, 10-day per satellite
Sensor	The optical Multi-Spectral Instrument (MSI), measuring 13 bands, push-broom sensing
Orbit	Sun-synchronous, 98.62° inclinations
Local image time	10:30 am Mean Local Solar Time (MLST) at descending node
Altitude	On average 786 km
Swath width	290 km

The sun-synchronous orbit of the Sentinel-2 satellites provides consistent measurements of the same location over time. Figure 2.1 shows a sun-synchronous orbit, with the yellow line representing the satellite's trajectory. In a sun-synchronous orbit, the angle between the Sun and the orbital plane remains constant. Therefore, the mean local solar time (MLST) at any given location is identical for all images. Mean local solar time is a time definition based on the position of the sun. Local solar time is set to 12:00 when the sun reaches its highest point in the sky. For the mean local solar time, it is assumed that the sun reaches its highest point at the same time each day [46]. This constant MLST, due to the satellites orbit, reduces the effects of shadows and varying illumination when comparing time-series data, thereby ensuring more consistent observations [43].

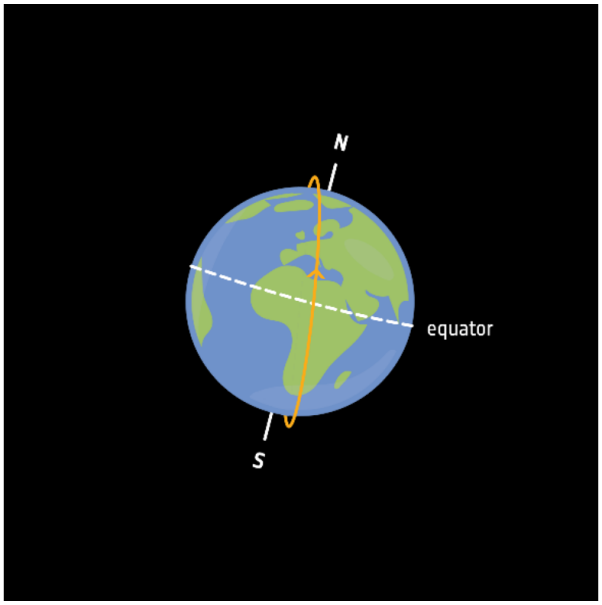

Figure 2.1: Illustration of a sun-synchronous orbit. Figure adapted from ESA [47]. Such an orbit enables images to be taken at the same local solar time.

For the albedo model, the atmospherically corrected surface reflectance (SR) products of the Sentinel-2 satellite were used [48]. The SR products are generated using TOA reflectance data and Sen2Cor, the atmospheric correction algorithm adopted by ESA [49]. Sen2Cor is an algorithm based on look-up tables generated using a radiative transfer model [50]. Among other parameters, the algorithm takes into account aerosol optical thickness, water vapour, elevation, and slope [49]. Appendix Table B.2 provides details on the SR product bands, listing the spectral range and central wavelength associated with each available spectral band.

Another Level-2A product used in the albedo model is the scene classification layer (SCL) [48][51]. The SCL identifies relevant conditions, such as the presence of clouds. It can be applied for quality control by masking pixels based on their classification. See Appendix Table B.3 for the various classification layers. The SCL is available at a spatial resolution of 20 m. In the albedo model, only pixels classified as either vegetated or non-vegetated were included. The aim of this strict filtering was to obtain high accuracy albedo values.

In this research, the satellite data was accessed trough Google Earth Engine (GEE). GEE is a cloud-based platform designed for remote sensing analysis [52]. It offers access to extensive datasets and significant computational resources, enabling large-scale geospatial analyses [53]. This makes a global analysis of a large number of locations possible. GEE was accessed via its Python application programming interface (API). Appendix B provides additional details on the GEE collection used to obtain the satellite data for the albedo model.

2.2. Albedo Determination Method

Since surface reflectance is measured in narrow spectral bands, a method is required to derive the broadband albedo. Various approaches for converting narrowband to broadband values have been developed and reported in literature. Appendix Table C.1 presents a comparison of several methods considered in this thesis. The approach proposed by Bonafoni et al. was selected because it relies on intuitive physical principles and does not require any additional input data [37]. With this approach, the albedo is obtained through a linear combination of the various Sentinel-2 surface reflectance bands, as presented in equation 2.1.

$$\alpha = \sum_{b} \rho_b \cdot w_b \tag{2.1}$$

The parameters and constants in equation 1.4 are as follows:

- α is the albedo.
- b indicate the bands taken into account.
- ρ_b is the surface reflectance per band.
- w_b is the weight per band.

To calculate the weight of each S2 band, the spectral solar radiation at the surface was used. A distinct spectral interval was assigned to each S2 band. Together, these intervals span the spectral domain from 300 nm to 3000 nm, each including its respective S2 band. This domain was chosen such that it encompasses nearly all solar radiation reaching the Earth's surface [37]. Every interval is defined by a lower (L_b) and an upper (U_b) wavelength boundary, with b indicating the S2 band the interval encompasses. Table 2.2 lists the (U_b) and (L_b) while table B.2 lists the central wavelength and the bandwidth of each S2 band. The weight of each band was determined by computing the proportion of incoming solar radiation contained within its spectral interval relative to the total incoming radiation, as described in equation 2.2 [37]. Figure 2.2 shows the defined intervals together with the corresponding S2 bands and the measured incoming solar radiation and Table 2.2 shows the weights for each S2 band. As can be seen in the table, S2 bands located near the long-wavelength end of the solar spectrum were assigned a lower weight.

$$w_b = \frac{\int_{L_b}^{U_b} I_s(\lambda) \cdot d\lambda}{\int_{0.3}^{3} I_s(\lambda) \cdot d\lambda} \tag{2.2}$$

In equation 2.2 $I_s(\lambda)$ is the at surface spectral solar irradiance at wavelength λ.

Table 2.2: Sentinel-2 Surface Reflectance spectral bands. Lower (L_b) and upper (U_b) wavelength limits (nm) and weights used for narrow-to-broadband albedo conversion [37].

Band (b)	L_b (nm)	U_b (nm)	w_b
2	300	533	0.2266
3	533	614	0.1236
4	614	730	0.1573
8	730	1226	0.3417
11	1226	1880	0.1170
12	1880	3000	0.0338

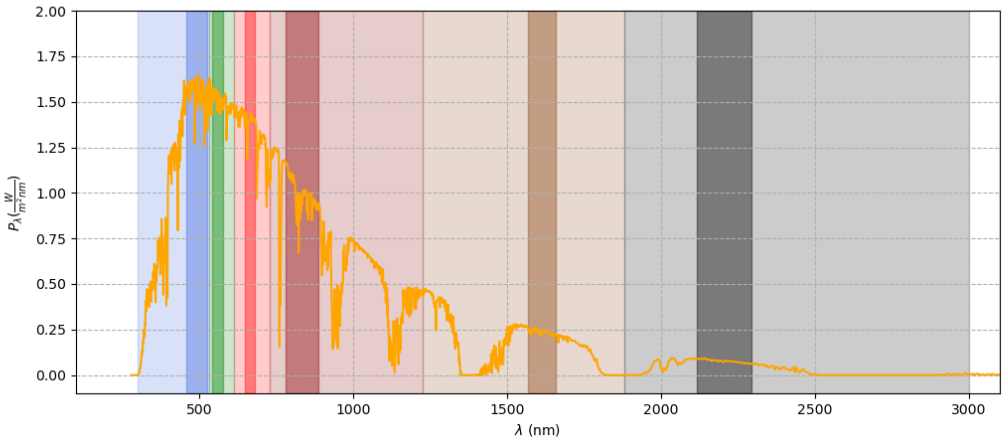

Figure 2.2: Spectral ranges of Sentinel-2 surface reflectance bands. The yellow curve shows the BOA global irradiance [18][19]. The narrow, darker bands represent the Sentinel-2 spectral bands, while the wider, lighter bands show the spectral intervals defined by Bonafoni for the albedo weighting calculation, U_b and L_b [37]. Band 2 is shown in blue, band 3 in green, band 4 in red, band 8 in dark red, band 11 in brown, and band 12 in grey.

In the Sen2Cor radiative transfer model, a Lambertian surface was assumed [49][37]. This assumption carries over to the albedo determination model. A Lambertian surface is an ideal diffuse reflector that scatters incoming light uniformly in all directions [54]. In practice, natural soils and solar panels do not exhibit this Lambertian behaviour and are considered non-Lambertian surfaces [55].

Figure 2.3 presents several reflectance profiles for a given angle of incidence, represented in a polar plot on the left and a Cartesian plot on the right. In this figure, the angle of incidence is indicated in yellow. Here the angle of incidence is equal to the solar zenith angle (θ_{SZ}), which is defined as the angle between the local zenith at the point of interest and the line extending from the sun to that same point. Furthermore, the figure displays a Lambertian reflection profile in blue and a purely specular reflection profile in red. Since the surface is not an ideal Lambertian reflector, its true reflectance profile must lie between the purely Lambertian and purely specular cases. In the literature, various choices for this intermediate profile are proposed depending on the type of surface. One example is the Phong model, in which the reflection distribution is represented by a cosine function elevated to a power determined by the surface roughness [56]. Another example describes the reflection profile using a Gaussian function together with an isotropic Lambertian component [57][58]. In the figure, a generic example of a combined profile is represented in green as a sum of two Gaussian functions. This profile is shown for illustrative purposes only. The grey area in the figure represents the range of reflection angles that can be observed by the satellite. These correspond to the view zenith angle of the satellite. A requirement for the albedo determination method by Bonafoni et al. is that the mean view zenith angle of all images remains below 20°. Since the maximum ϕ_{VZ} is about 11°, this requirement is met for all images in the dataset.

The differences between the Lambertian and combined profiles, as Figure 2.3 shows, can lead to errors in the reflectance estimates. For instance, when the combined profile lies above the Lambertian profile within the grey region, as is the case for small values of θ_{SZ}, assuming Lambertian behaviour can result in an overestimation of the reflectance. The reason is that the satellite is able to register more reflected light than the Lambertian profile would predict. Conversely, when θ_{SZ} takes on a large value, the reflectance may be underestimated because the satellite detects less light than would be expected from a Lambertian surface. For intermediate, moderate values of θ_{SZ}, the combined profile aligns most closely with the Lambertian profile, which could lead to the most accurate reflection values. Therefore, the θ_{SZ} at the time the S2 image is acquired may play an important role in the accuracy of the albedo estimation. Previous studies have also highlighted the importance of the solar zenith angle θ_{SZ} at the time of image acquisition, since a shorter atmospheric path for the light results in fewer disturbances [59]. Additionally, Bonafoni et al. found lower percentage error in their albedo determination for lower SZA [37].

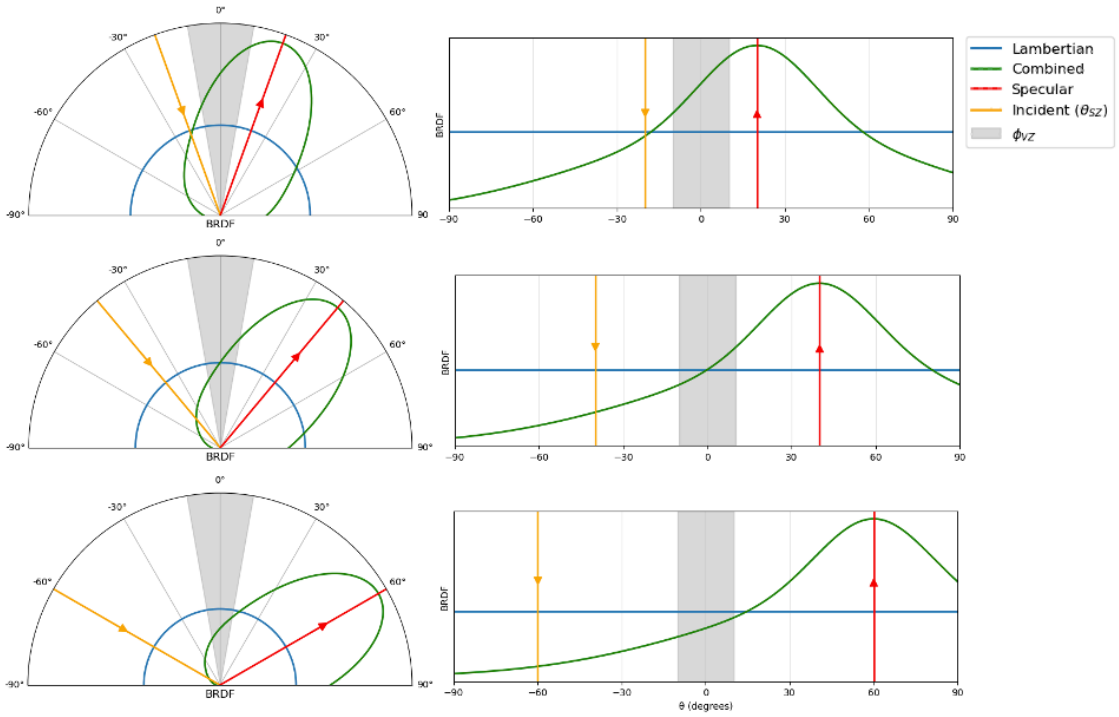

Figure 2.3: The figure is adapted from Figure 1 in [57]. It depicts various Bidirectional Reflectance Distribution Functions (BRDF), also referred to as reflection profiles. A Lambertian surface in blue, a specular reflector in red, and a possible intermediate profile that combines both behaviours in green. The incoming light is shown in yellow, while the range of angles observable by the S2 satellite is shown in grey. Each row presents a polar plot (left) and a Cartesian plot (right) corresponding to the same angle of incidence. The values on angular axis of the polar plot and the x-axis of the cartesian plot are illustrative.

To apply the narrow-to-broadband conversion, all bands used should be at the same spatial resolution. As not all SR bands used in this approach are available at the same spatial resolution, the bands need to be resampled at the same resolution. Bonafoni proposed increasing the spatial resolution of the 20 m bands to 10 m by using reprojection in GEE [60]. GEE offers three options for reprojection: nearest neighbours, bilinear interpolation, and bicubic interpolation. Additional details on the GEE reprojection methods are provided in Appendix C. In Figure 2.4, an example illustrates how the three reprojection methods are used to increase the resolution of a particular band. The area of interest (aoi) is shown as a blue square in the image. Because the bicubic reprojection method requires additional neighbouring pixels, a 2-pixel (or 20 m) buffer is applied around the aoi, represented by the red square. With each of these three reprojection methods the albedo is calculated.

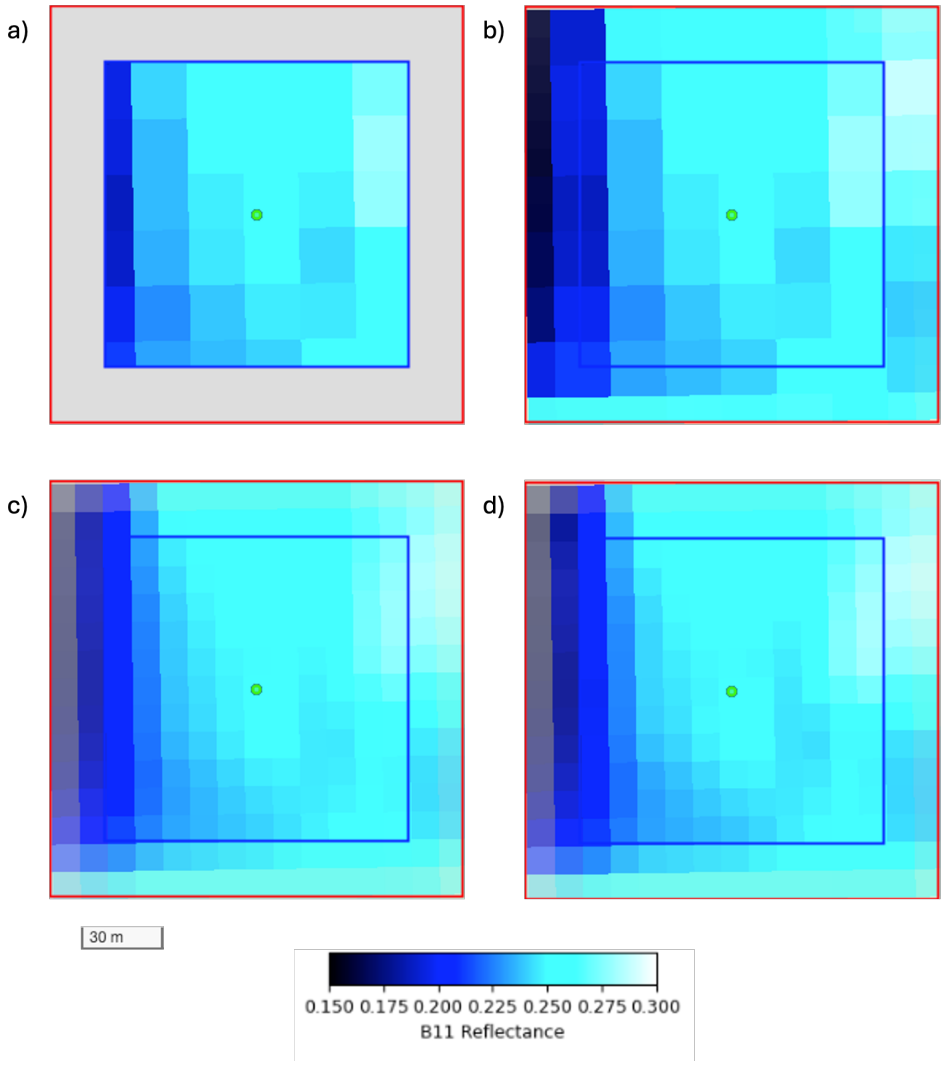

Figure 2.4: Illustration of the super-resolution process for band 11. The blue square marks the area of interest (aoi), while the red square denotes a 20 m buffer surrounding the aoi. The figure presents: a) the original image, b) the image resampled using nearest neighbour, c) the image resampled with bilinear interpolation, and d) the image resampled with bicubic interpolation.

2.3. Validation Method

To verify the albedo determination approach applied in this thesis, several tests were conducted. For these tests, seven stations from the Surface Radiation (SURFRAD) Network were used [61]. SURFRAD is a U.S. network that provides continuous, ground-based measurements of surface radiation. Additional details about SURFRAD are given in Appendix C. The validation approach followed a modified version of the SURFRAD test conducted by Bonafoni et al. [37].

For the validation, Sentinel-2 imagery was acquired for each SURFRAD station location. The pyranometer used to measure the global upwelling solar radiation flux has an approximate footprint radius of 60 m. The S2 image collection's area of interest (aoi) was specified as a circular region with a radius of 60 m, centred on the SURFRAD tower. For image extraction, an additional 20 m buffer was applied around this aoi, providing neighbouring pixels for the bicubic interpolation. All image pixels were filtered so that, as previously mentioned, only those with SCL labels indicating either vegetated or non-vegetated land were used. For each month, the image with the highest number of remaining pixels after filtering was chosen. If this maximum pixel count was below 150, that month was excluded. The image collection covered the period from 2022-10-01 to 2025-09-30.

After gathering the monthly S2 images, the SURFRAD measurement data for the matching dates were collected, and imported using the pvlib Python toolbox [19]. From these imported datasets, the upwelling and downwelling radiative fluxes corresponding to the exact acquisition time of each S2 image were extracted. Then, equation 2.3 was applied to derive the measured SURFRAD albedo values. However, if any quality control flags were triggered for a given measurement, an alternative measurement within ± 10 min of the image acquisition time and free of quality issues was searched for. If no suitable replacement was available, that month was excluded from the analysis. Using this procedure ensured that only high-quality SURFRAD albedo measurements were used in the analysis.

$$\alpha_{surf} = \frac{G_{SW}^{\uparrow}}{G_{SW}^{\downarrow}} \tag{2.3}$$

The parameters and variables in equation 2.3 are as follows:

- α_{surf} is the surface broadband shortwave albedo measured by SURFRAD (dimensionless).
- $G_{SW}^{\uparrow}$ is the upwelling global shortwave solar radiative flux at the surface, in W/m^2.
- $G_{SW}^{\downarrow}$ is the downwelling global shortwave solar radiative flux at the surface, in W/m^2.

To obtain the corresponding S2 albedo estimates, the three interpolation methods were applied to the 20 m bands of each image, yielding three S2 albedo grids per image. Figure 2.5 shows an example of a satellite image used for the S2 albedo estimation. Since the SURFRAD measurement provides a single albedo value, all albedo pixels in the S2 image are combined into one representative value. To achieve this, a weight was assigned to each pixel based on the cosine of the angle between the sensor's nadir direction and the line extending from the sensor to that pixel. Here, the nadir refers to the vertical pointing down towards a surface or from a specified point of interest. The pixel weights were determined using equation 2.4. By multiplying each albedo pixel by its corresponding weight, the Sentinel-2 albedo (α_{S2}) was estimated.

$$w_{pix,i} = \frac{\cos(\beta_i)}{\sum_{i=1}^{N} \cos(\beta_i)} \tag{2.4}$$

The parameters and variables in equation 2.4 are as follows:

- $w_{pix,i}$ is the pixel weight.
- β_i is the angle between sensor nadir and the line from the sensor through the pixel.
- i is the pixel index.
- N is the total number of pixels in the pyranometer footprint.

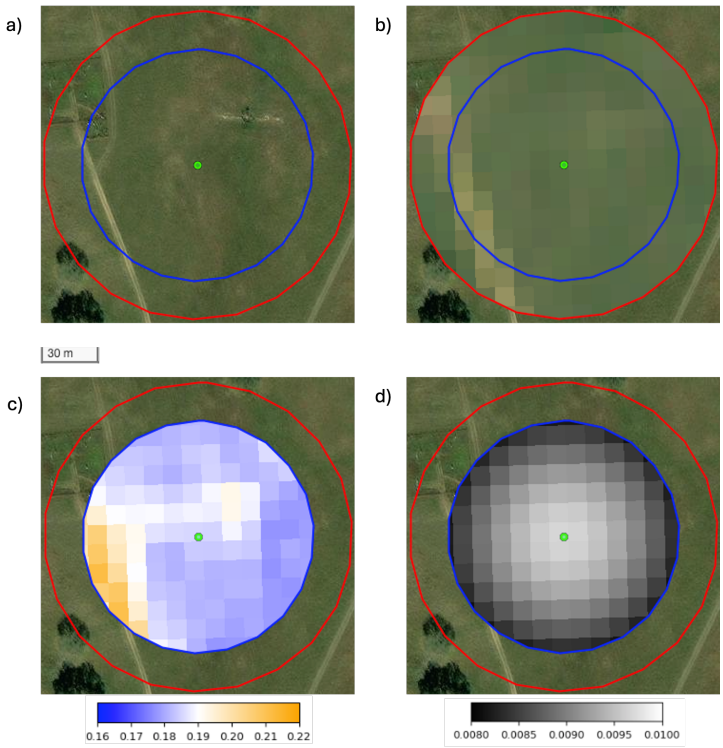

Figure 2.5: Example of albedo retrieval from Sentinel-2 at a SURFRAD station site. Panel a) shows the map view of the SURFRAD station 'bon'. Panel b) presents the Sentinel-2 scene acquired on 15 May 2023. Panel c) displays the albedo derived using nearest-neighbour interpolation, and panel d) illustrates the weights assigned to each albedo pixel to compute a single representative albedo value.

The three reprojection approaches were assessed with respect to both accuracy and computational efficiency. Accuracy was evaluated against the SURFRAD observations as previously described. To assess computational performance, all three albedo calculations were run and their execution times were recorded. For these timed runs, a 300 m by 300 m region was selected. A single image was acquired, with no pixels removed by filtering, and its albedo was computed 1000 times for each of the three projection techniques. For each method, the mean, standard deviation, minimum, and maximum calculation times were computed and then compared.

For every SURFRAD station, the land cover type was identified using the MODIS MCD12Q1 dataset accessed via GEE [62]. This dataset provides annual classifications. Data for the year 2024 were used, as it is the most recent full year within the analysed period. The spatial resolution of the dataset is 500 m by 500 m.

2.4. Validation Outcome

Figure 2.6 presents the S2 albedo estimates derived with the three interpolation methods, plotted against the SURFRAD albedo observations. After filtering of all flagged measurements 225 data points were left. All measurements and estimates lie within an albedo range of 0.1 to 0.3. In the figure, only the final albedo method, obtained with bicubic interpolation, is visible. This is because the other two methods produce almost identical results. The RMSE, bias, and correlation coefficient for each method are listed in Table 2.3. All three methods yield an overall RMSE of 0.032 and a bias of -0.008. The bilinear and bicubic approaches both achieve a correlation of 0.446, whereas the nearest neighbour albedo method yield a correlation of 0.445. This difference is correlation is deemed in significant. These results show that the interpolation method has very little to no influence on the albedo results, as also noted by Bonafoni [60].

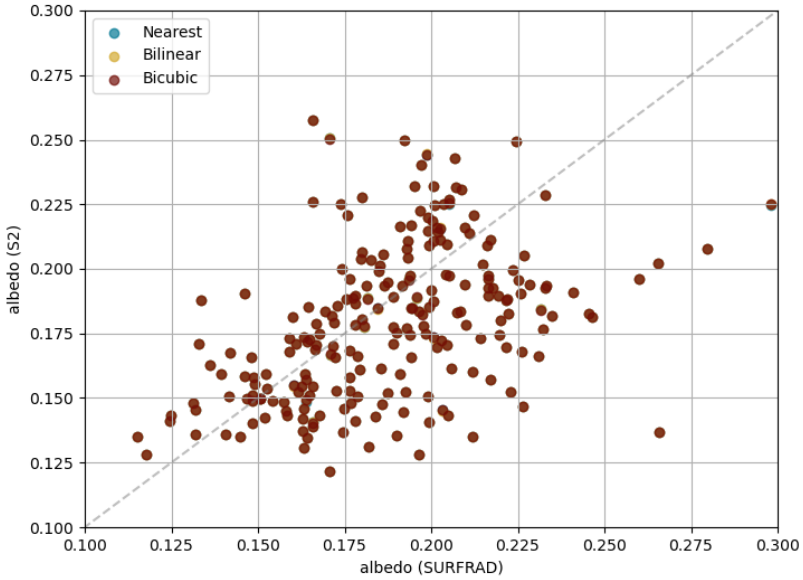

Figure 2.6: Comparison of Sentinel-2-derived albedo using three different interpolation methods, with albedo observations from all seven SURFRAD stations. All three interpolation approaches yield nearly identical values; consequently, only the final method is distinguishable in the plot. The dashed grey line represents the 1:1 line, indicating equal albedo between Sentinel-2 and SURFRAD measurements.

Since all three albedo methods produced identical results, their computational performance was also assessed. The albedo was determined 1000 times of the same image for each albedo method. The corresponding findings are summarized in Table 2.3. The differences are minor, with the bilinear approach being the fastest overall. Nevertheless, the nearest neighbour method shows the lowest standard deviation and the smallest maximum computation time, which points to higher stability. In contrast, the bilinear method is characterized by a large maximum time and a high standard deviation. Due to its greater stability and its mathematical simplicity, the nearest neighbour reprojection method was selected. All subsequent results and analyses are therefore based exclusively on the nearest neighbour reprojection approach.

Table 2.3: Performance comparison of reprojection techniques for albedo estimation. Shown are accuracy measures (RMSE, bias, and correlation) along with computational performance (in seconds).

Metric	Nearest	Bilinear	Bicubic
RMSE	0.032	0.032	0.032
Bias	-0.008	-0.008	-0.008
Correlation	0.445	0.446	0.446
Average time (s)	0.771	0.755	0.764
Std deviation (s)	0.316	0.416	0.323
Min time (s)	0.476	0.488	0.495
Max time (s)	3.421	6.553	3.588

Figure 2.7 again presents the comparison between the S2-derived albedo and the albedo measurements from SURFRAD. This figure however only shows the nearest-neighbours albedo method, representing each SURFRAD station with a different colour. Although the scatter plot shows many points clustered along the main diagonal, the results as a whole are still quite scattered. In particular, the values below the central diagonal are more widely spread, whereas the data points above the central diagonal show a tighter correlation. This aligns with the negative bias of -0.008 indicating an underestimation of the albedo. The resulting overall RMSE of 0.032 is higher than the error of 0.023 reported by Bonafoni et al. [37]. A closer examination of the images with the largest errors revealed no unusual features. It should be noted, however, that this analysis is based on 225 measurements, whereas Bonafoni et al. relied on only 42 measurements. Moreover, although Bonafoni et al. excluded station "dra" from their analysis, applying the same exclusion to these results did not lead to any improvement.

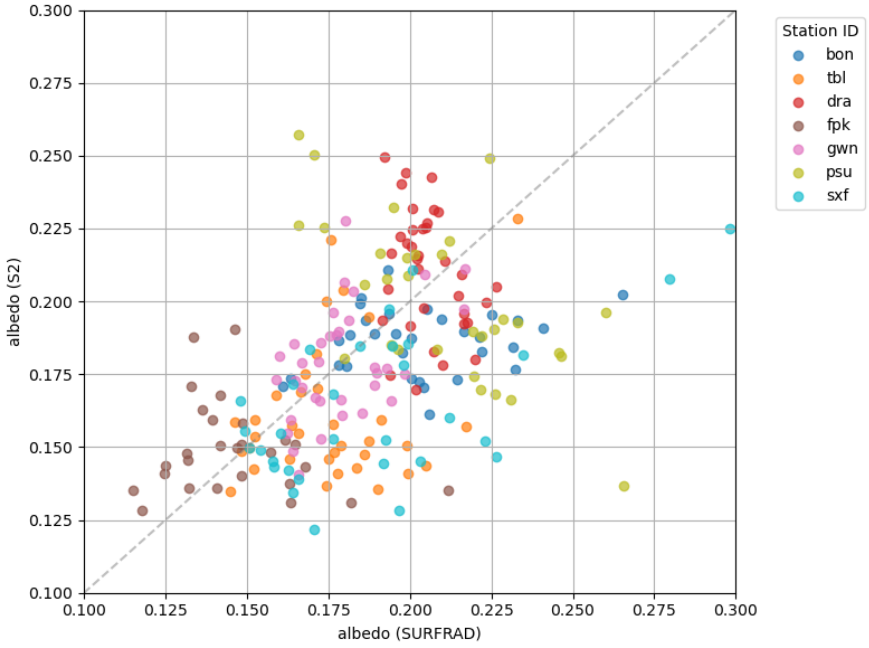

Figure 2.7: Comparison of Sentinel-2 derived albedo to albedo measured at seven SURFRAD measurement stations. The same data as shown in figure 2.6. However, only the nearest neighbour interpolation method is shown and each station is indicated in a different colour.

Table 2.4 presents the error, bias, correlation, and landcover type for each station individually, with the stations arranged in order of decreasing latitude. It is clear that the ”psu” station shows the largest error by a significant margin. This may be due to the fact that this station has the most spatially heterogeneous measurement footprint. It is located along the edge of three distinct crop fields, all of which are included in the measurement. All other stations, including those located in cropland regions, exhibit a more uniform measurement footprint. Exuding ”psu” from the graph resulted in an improved RMSE of 0.029, a equal bias of -0.008 and an improved correlation of 0.534. Furthermore, station ”gwn” exhibits the smallest error. This might be linked to the land cover type. However, since there is only one station located in the Woody Savannas, this cannot be confirmed. At stations situated at higher latitudes, fewer appropriate measurements or images were available. This is likely due to the higher likelihood of snow in these regions, since pixels classified as snow or ice were excluded from the S2 imagery.

Table 2.4: SURFRAD stations with station ID, geographic location, and land cover type. For each station, the root mean square error, correlation coefficient, and bias of the Sentinel-2 derived albedo relative to the observed albedo are reported. Stations are arranged in order of decreasing latitude.

Station id	Station location	Number of data points	Land Cover Type	Error (RMSE)	Correlation (R)	Bias
fpk	Fort Peck, Montana	27	Grasslands	0.028	-0.178	0.003
sxf	Sioux Falls, South Dakota	31	Croplands	0.039	0.583	-0.026
psu	Penn State Univ., PA	31	Croplands	0.049	-0.642	-0.010
tbl	Table Mountain, Colorado	35	Grasslands	0.030	0.260	-0.015
bon	Bondville, Illinois	31	Croplands	0.029	0.203	-0.017
dra	Desert Rock, Nevada	35	Urban and Built-up	0.025	-0.306	0.005
gwn	Goodwin Creek, Mississippi	35	Woody Savannas	0.018	0.458	0.000

As discussed earlier, the accuracy of the Lambertian assumption is expected to vary with the solar zenith angle. Accordingly, Figure 2.8 presents the results again, this time with colours indicating the mean solar zenith angle of the corresponding S2 image used. The results that appear above the central diagonal are predominantly associated with low θ_{SZ} values, whereas those below the central diagonal were obtained under conditions of a high solar zenith angle. The data points nearest to the central diagonal appear to have been obtained with a θ_{SZ} of approximately 40°. This suggests that θ_{SZ} is correlated with whether the albedo is under- or overestimated, with the bias being smallest for θ_{SZ} values around 40°.

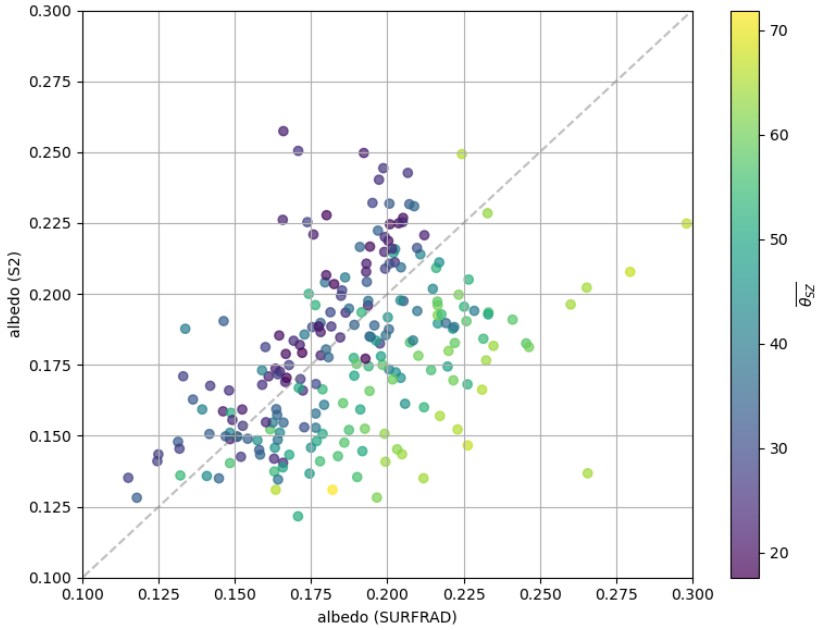

Figure 2.8: Comparison between albedo estimated from Sentinel-2 imagery and albedo measured at SURFRAD measurement stations. The colour of each data point represents the mean solar zenith angle ($\overline{\theta_{SZ}}$) of the Sentinel-2 image used for the albedo estimation.

For further analyses of this correlation, Figure 2.9 presents the error, bias, correlation, and sample size for the dataset when it is divided into mean θ_{SZ} intervals of 10°. The lowest RMSE occurs in the 30°–40° bin, and the error increases farther away from this bin. The finding that the most favourable conditions for estimating albedo from satellite data occur for θ_{SZ} between 30° and 40° is consistent with the optimal conditions reported in literature[63]. Moreover, the bias bins confirm the pattern observed in Figure 2.8. A linear relationship is observed between the bias bins and θ_{SZ}. This observation is consistent with the theoretical expectations of over- and underestimation of reflectance arising from the Lambertian assumption. The correlation bins again indicate the strongest performance for the 30° to 40° θ_{SZ} interval. As expected, a decrease in RMSE is associated with a corresponding rise in correlation.

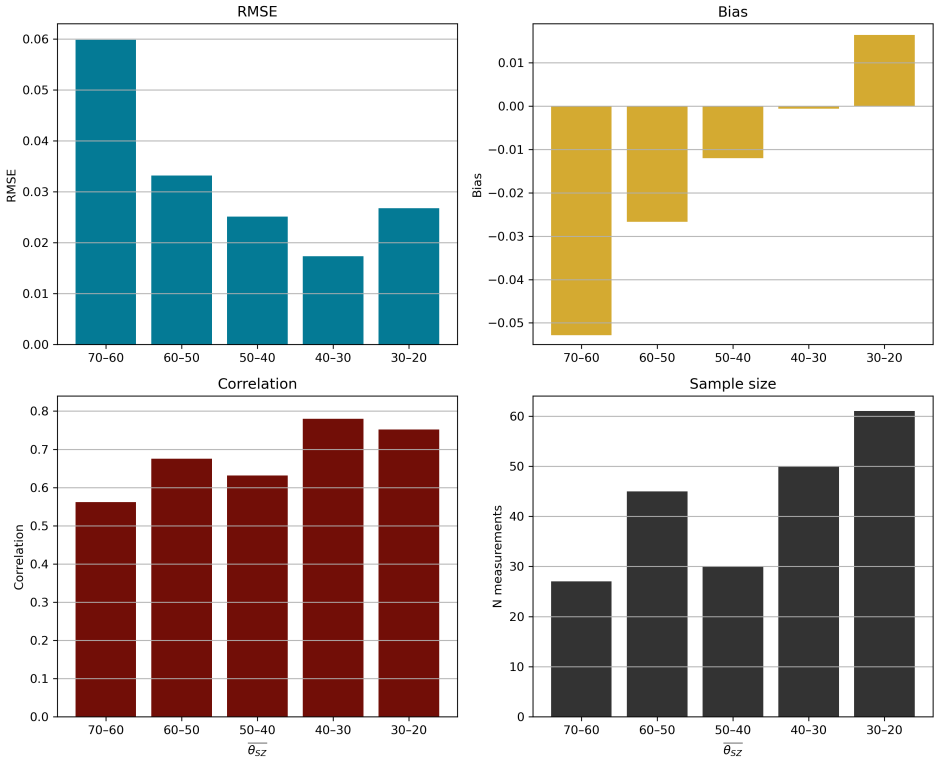

Figure 2.9: comparison between albedo estimated from Sentinel-2 imagery and albedo measured at the SURFRAD measurement stations. The root mean squared error (RMSE), bias, correlation coefficient (R), and sample size for different mean solar zenith angle ($\overline{\theta_{SZ}}$) are shown. The results are grouped in $\overline{\theta_{SZ}}$ bins spanning 10°. The $\overline{\theta_{SZ}}$ is the angle as recorded for the Sentinel-2 image used to estimate albedo.

To examine how the bias depends on θ_{SZ}, Figure 2.10 presents scatter plot of the bias of each data point against the mean solar zenith angle of the S2 image. A rough linear trend can be observed in the plot, though the data points are broadly scattered. A linear relationship was fitted to the data. The identified relationship is shown in the figure as a red dashed line. Equation 2.5 represents the identified linear relationship. The coefficient of determination (R^2) for this fit is 0.553, reflecting the wide spread of the data. This equation can be used as a bias correction on the albedo estimation data. This leads to an adapted form of Equation 2.1, which is presented in Equation 2.6.

$$bias = -0.0016 \cdot \overline{\theta_{SZ}} + 0.0549 \tag{2.5}$$

$$\alpha = \sum_b \rho_b \cdot w_b - 0.0016 \cdot \overline{\theta_{SZ}} + 0.0549 \tag{2.6}$$

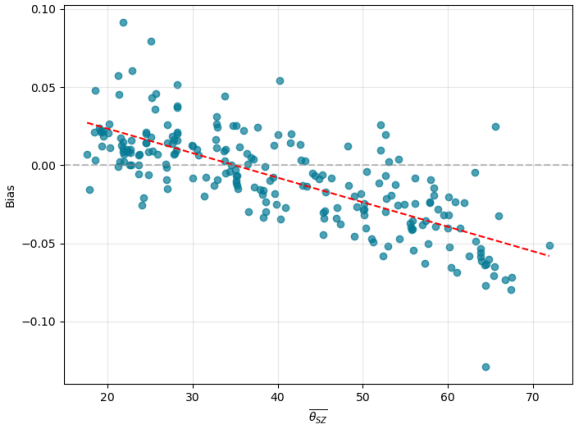

Figure 2.10: Scatter plot of the bias against the mean solar zenith angle ($\overline{\theta_{SZ}}$) of the Sentinel 2 image used in the albedo determination. The red dotted line shows the linear fit to the data given by $bias = -0.0016 \cdot \overline{\theta_{SZ}} + 0.0549$. The coefficient of determination of the linear fit is $R^2 = 0.553$.

Figure 2.11 presents the scatter plot comparing the estimated albedo with the measured albedo after the proposed bias correction was applied. The colour of each data point once more represents the value of θ_{SZ} at the moment the satellite image was taken. After applying the bias correction, the data points are more tightly grouped along the central diagonal. Moreover, after applying the bias correction, the different θ_{SZ} values are more mixed together than they were beforehand. Overall, applying the bias correction yielded an improved RMSE of 0.021, which is now lower than the error of 0.023 reported by Bonafoni et al. [37]. This is an improvement in the RMSE of more than 34%. After implementing the correction, the total bias rose to 0.00. This outcome is expected, since the correction itself was derived from the observed bias. Furthermore, and an improved correlation of 0.773 was found with the bias correction.

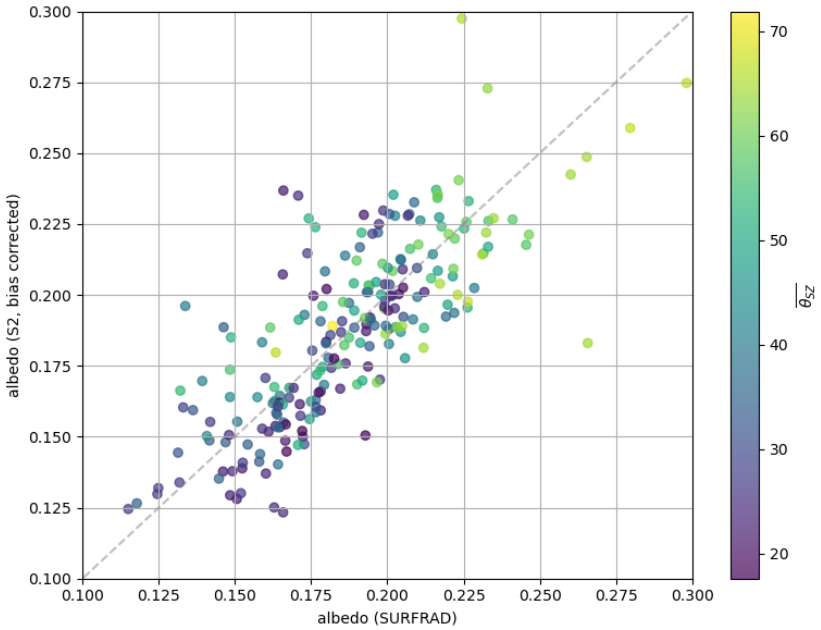

Figure 2.11: Comparison between bias corrected albedo estimated from Sentinel-2 imagery and albedo measured by SURFRAD. The colour of each data point represents the mean solar zenith angle ($\overline{\theta_{SZ}}$) of the Sentinel-2 image used for the albedo estimation.

Figure 2.12 shows the error, bias, correlation, and sample size for the corrected dataset again divided into mean θ_{SZ} intervals of 10°. In the figure shows the uncorrected results in a lighter colour for comparison. The RMSE decreased across all bins, with the largest reduction observed in those farthest from the 30° to 40° range. The bias likewise decreased in all bins. Nevertheless, for the bins between 40° and 600°, the bias was over corrected. The correlation values show a slight increase in all bins, with the exception of the 20° to 30° bin. Overall the bias corrections shows fairly good results.

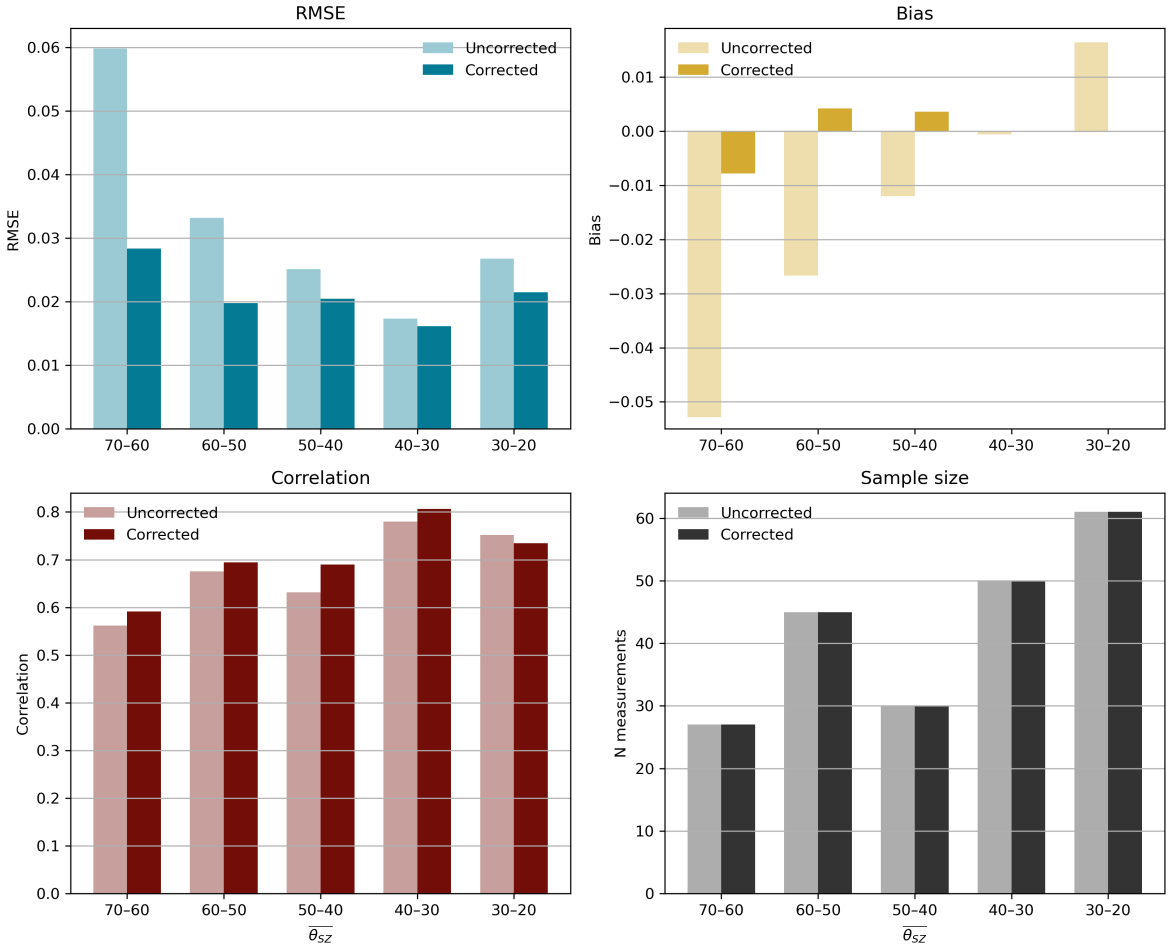

Figure 2.12: comparison between albedo estimated from Sentinel-2 imagery, both corrected and uncorrected, and albedo measured by SURFRAD. The root mean squared error (RMSE), bias, correlation coefficient (R), and sample size for different mean solar zenith angle ($\overline{\theta_{SZ}}$) bins are shown. The results of the uncorrected bins are shown in a lighter colour while the bias corrected results are shown in the darker colour in each plot.

2.5. Albedo Determination Conclusion

In this chapter, the first research sub-goal was achieved through the development of a model to determine land surface albedo at high spatial resolution using Sentinel-2 surface reflectance data. The model produces albedo estimates with a RMSE of 0.032, which is reduced to 0.021 after bias correction. This performance is slightly better than previously reported by Bonafonia et al., demonstrating the suitability of the proposed approach for high-resolution albedo estimation. The derived bias correction was based in measurement data and the Lambertian assumption of the albedo method. However, a deeper theoretically grounded bias correction, for instance one derived from the Phong model, could potentially yield even better results.

3

Albedo Change Model

In this chapter, the second research sub-goal is examined: The development of a model that uses recent PV data to determine the change in albedo due to the deployment of solar farms. The first section discusses the solar farm dataset used as model input and outlines the filtering procedure. The subsequent section details the methods applied to estimate the albedo change associated with each solar farm. The next section presents the resulting findings and their analysis. The final section provides the conclusions drawn from the albedo change model.

3.1. Input Solar Farm Data

In the selection of a solar farm database, several datasets were evaluated, including Wiki-Solar [41], Kruitwagen et al. [42], Global Renewables Watch (GRW) [64], and TransitionZero Solar Asset Mapper (TZ-SAM) [65]. Appendix Table D.1 summarises these datasets. While Xu et al. based their work on the Wiki-Solar dataset, this dataset is not publicly accessible and was therefore not used in the present study [25]. Several other studies have made use of the dataset assembled by Kruitwagen et al. However, this resource provides only a single temporal snapshot for the end of the year 2018 [31]. Given the rapid expansion of installed PV capacity in recent years, more recent data is desired [9][10][11]. The GRW and TransitionZero datasets are both relatively recent and have been updated on a quarterly basis. Unfortunately, the GRW dataset has not received any updates since Q2 2024. Consequently, this study relied on the TransitionZero Solar Asset Mapper database.

The TZ-SAM provides polygons and multi-polygons representing identified solar farms. Every farm is labelled with a unique cluster or farm ID. The metadata includes further details for each solar farm, such as estimated installed capacity, 'constructed after' and 'constructed before' dates, the central latitude and longitude, and the name of the country in which the solar farm is located. The dataset is restricted to solar farms that have an estimated installed capacity of at least 500 kW. The TZ-SAM Q3 2025 dataset release was used in this study. At this point the TZ-SAM detected a total installed capacity of 1185 GW. A limitation of the dataset is that no distinction is made between floating PV, solar thermal, stationary and tracking PV systems [65]. Additionally, the dataset does not include an estimate of the ground cover ratio, the ratio between PV area and the polygon area.

The preprocessing of the TZ-SAM data was performed in Python using GeoPandas [66]. The areas of all polygons and multi-polygons were determined through geodesic calculation using the pyproj Python package [67]. In addition, the country code associated with each solar farm was determined using the pycountry Python package, and complemented by custom mappings for country names that the package did not recognise [68][69]. Furthermore, in order to conduct a three-year analysis for each solar farm, only solar farms that were constructed before Q3 2022 were included. To keep the dataset at a manageable size, the 500 most recently constructed farms were chosen using the 'constructed after' date. The polygon geometry of one of the farms was too complex to be processed and was therefore substituted with the next most recently constructed farm. Figure 3.1 shows the locations of these 500 farms.

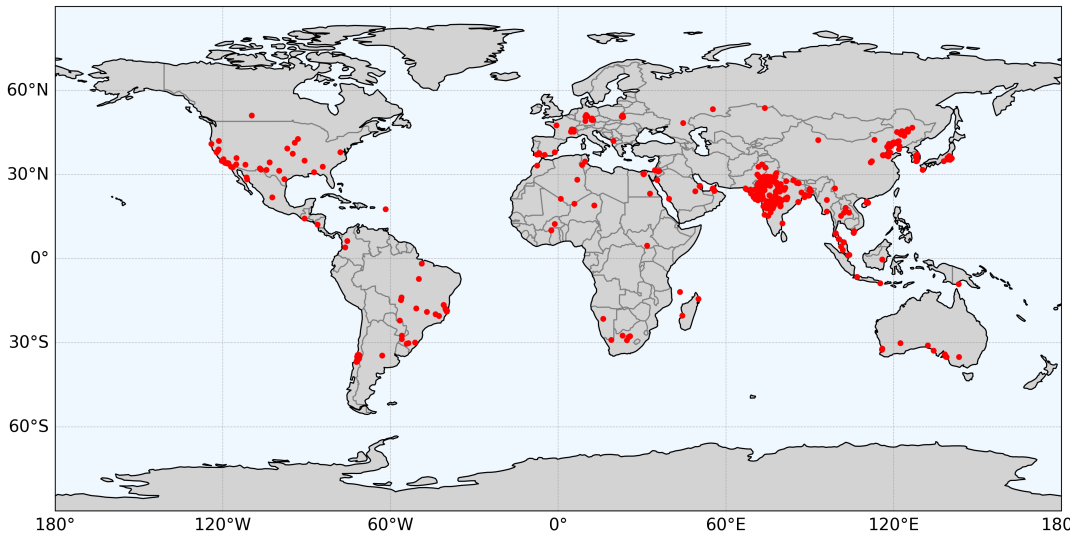

Figure 3.1: Map indicating the locations of the 500 solar farms, from the Transition Zero solar farm dataset, selected for albedo change analysis.

Once the farms for analysis were selected, a buffer polygon was created for each one. This simplified buffer polygon encloses the polygon or multi-polygon that defines each farm. A buffer of 0.0003° was used, which corresponds to approximately 20–30 m for the farms analysed, depending on their latitude. In this report, the solar farm polygon generated by TZ-SAM is referred to as aoi_{pv}, while the surrounding buffer polygon is referred to as aoi_{buf}. Figure 3.2 shows an example of the aoi_{pv} and aoi_{buf} of a selected farm.

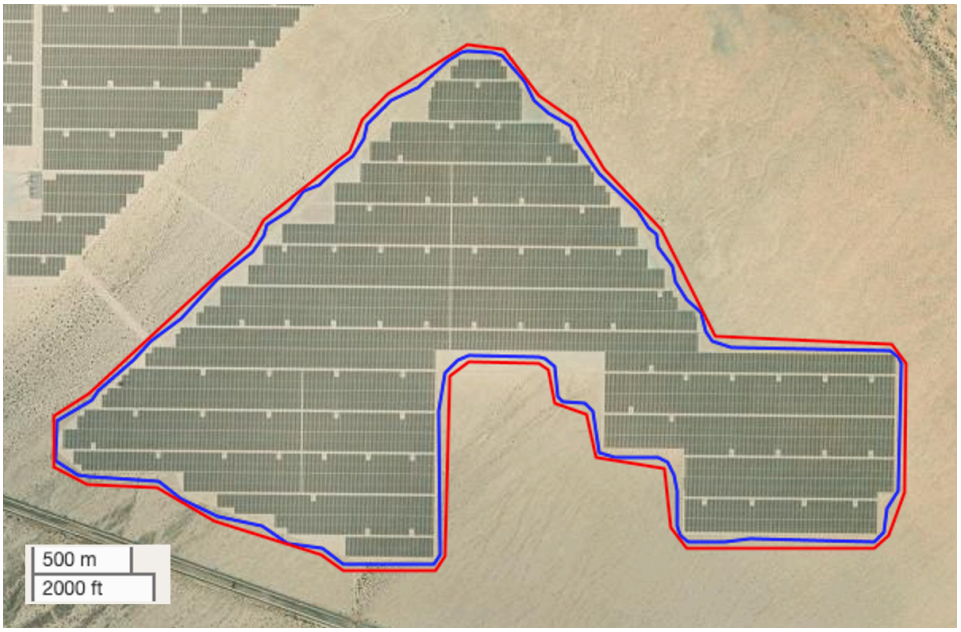

Figure 3.2: Map image of farm 14362, located in California, USA. The blue polygon indicates the solar farm region detected by the dataset (aoi_{pv}) while the red polygon indicates buffer polygon region (aoi_{buf}).

3.2. Albedo change methods

To quantify how a solar farm alters the surface albedo, the albedo of the site without the solar farm must be determined. With satellite data, this can be achieved with three year averages of images captured prior to the installation of the solar farm, or imagery from the areas surrounding the solar farm, similarly to previous work [25] [31] [24]. The use of prior satellite images has the benefit that the exact position of the farm can be used, whereas satellite imagery of the surrounding area might incorrectly include the albedo of adjacent structures. However, because the albedo calculation error differs for each image, using the albedo difference relative to the surrounding area rather than to a previous image eliminates the need to account for variations in error between images. Additionally, to enable a comparison of the albedo with images from before the solar farm was installed, an extra three years of data must be available and processed. Given that S2 SR imagery is only available from December 2018, TZ-SAM data from Q3 2025, and the analysis spans three years, the comparison of albedo before and after solar farm installation can only be conducted for farms installed between 13-12-2021 and 01-10-2022. In the Q3 2025 TZ-SAM dataset, there are no farms installed within this time period. Consequently, the albedo change was estimated using the surrounding area.

For the albedo change analysis, images were collected using the aoi_{buf} and by implementing pixel masking as described in Chapter 2. Images were gathered for the time span from 01-10-2022 to 01-10-2025. For each month, up to four images were selected in order to restrict the volume of data to be processed. Images containing less than 100 pixels were excluded from the analysis. In addition, because farm sizes differ substantially, a farm-specific threshold was applied. For each farm, the highest number of pixels observed in a single image was recorded. Any image with fewer than half of this maximum pixel count was excluded from further analysis. If there were more than four remaining images, those with the largest total number of pixels were chosen.

After all images for a given farm were collected, the change in albedo was calculated. For each farm, three masks were generated: one for all pixels located entirely within the aoi_{PV}, one for pixels within the aoi_{buf} but completely outside the aoi_{PV}, and one for the edge pixels that are only partially contained within the aoi_{PV}. Next, the albedo for every pixel in the image was computed using the approach outlined in Chapter 2. Using the masks, the albedo pixels were categorised into PV, edge, and surrounding regions. Figure 3.3 presents an example albedo map for a farm alongside the corresponding masks for that farm. For the PV and surroundings region the average of all the albedo pixels was determined. The albedo change caused by the solar farm was obtained by calculating the difference between these two albedo values.

However, as Figure 3.2 shows, some of the pixels within the aoi_{pv} do not actually correspond to PV panels. Since the ground cover ratio is unknown, and it is not clear in advance whether the albedo of the surroundings or that of the PV surface is lower, the pixels used to determine the PV albedo cannot be selected precisely. To still obtain an estimate of the PV albedo, it was assumed that at least 75% of the pixels within each aoi_{pv} actually correspond to the PV surface. Under this assumption, the pixel albedo values of aoi_{pv} that fall within the interquartile range should contain only PV pixels, as long as there is a sufficiently strong contrast between PV pixels and the surrounding pixels. Additionally, if this contrast is weak, the PV albedo value should likewise not be affected substantially. Therefore, the mean value of the albedo pixels within the interquartile range was was taken as the albedo estimate.

In Chapter 2, it was shown that using the derived bias correction enhances the accuracy of the S2 albedo estimates. To assess whether the bias correction could be applied to the solar farm results, both the Lambertian assumption and the surface orientations were considered. It was assumed that the Lambertian reflection component of natural surfaces is higher than that of PV panels. Conversely, for PV panels, the specular reflectance component is taken to be greater than the specular reflectance component of natural surfaces. This assumption was based on the dominant market share of glass front cover PV [22][70], the non Lambertian behaviour of glass and other smooth man-made materials [71][72], and that only highly rough materials exhibit Lambertian behaviour [72]. Under this assumption, the bias correction applied to PV pixels should be even more pronounced than the correction for natural surfaces, such as the SURFRAD measurement stations on which the correction is originally based. However, it remains unclear to what extent the bias correction should be adjusted, since there is no validation data available for this adjustment.

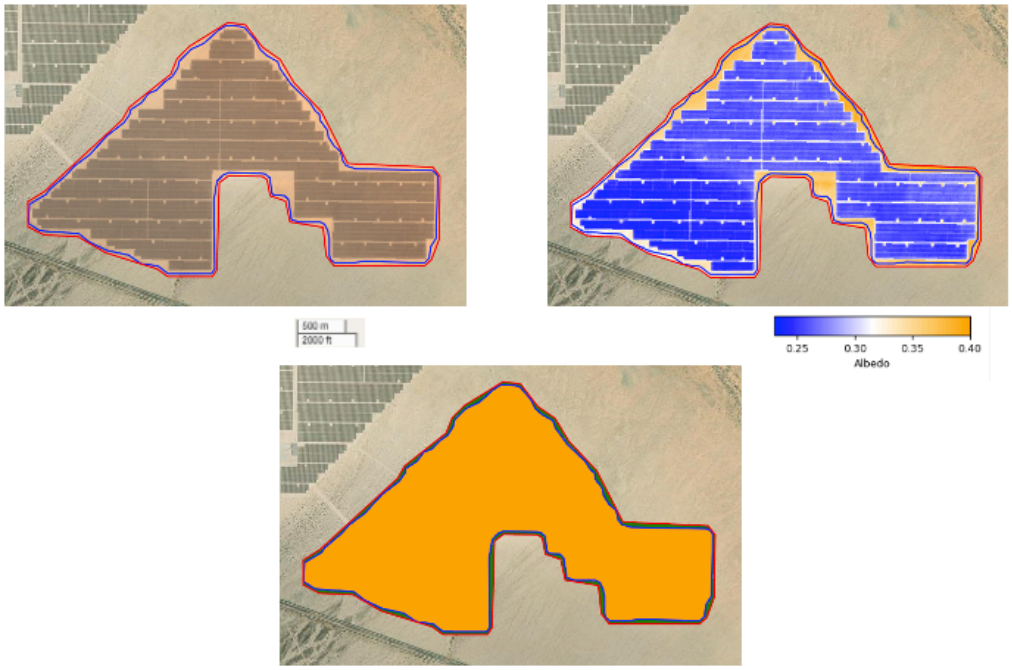

Figure 3.3: Satellite image (top left), albedo map (top right), and region masks (bottom centre) for farm 14362. In the bottom centre map, the orange pixels represent the PV mask and the green pixels the surroundings mask. The blue polygon indicates the solar farms area of interest aoi_{pv}, and the red polygon indicates the buffer area of interest aoi_{buf}. Satellite image dated 2023-05-05.

Another factor that influences the bias correction is the slope and orientation of the surface. For PV modules this is the tilt and azimuth angle. The bias correction was derived with measurement data from the predominantly flat SURFRAD station locations [61]. As the bias correction depends on the relative angle between the sun and the measured surface, it could be adapted for known slopes and orientations or tilt and azimuth angles. However, this information is not included in the TZ-SAM dataset. Furthermore, the modified bias correction functions could not be verified with the data available. Consequently, the bias correction was left unadjusted.

Although the bias correction itself was not modified, the initial correction was applied to both the PV and the surrounding region in each image. This approach was chosen because the Lambertian assumption is still weak in both regions as discussed before. The bias correction is identical for both regions within a given image, since it depends on the value of θ_{SZ} at the time the image was acquired. Therefore, the albedo change, determined from the difference between the two regions in each image, was unaffected by the application of the bias correction.

3.3. Results & Analysis

Figure 3.4 presents results for an example farm located in California, USA. The example farms used is the farms shown in Figure 3.2. The mean albedo value from each available image of the farm is used. For both the PV region and the surrounding region, three-year monthly albedo averages are computed and visualized. The albedo of the PV region is denoted by α_{PV}, while the albedo of the surrounding region is represented by α_{SUR}. The figure also displays the bias corrected albedo values for both the PV region and surroundings region. The albedo difference, shown in blue, is defined as $\alpha_{PV} - \alpha_{SUR}$ and yields negative values when the solar farm leads to a decrease in surface albedo.

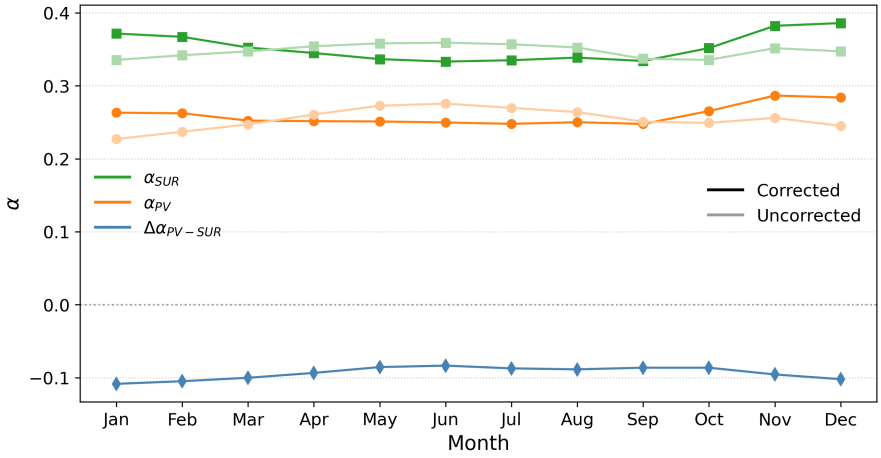

Figure 3.4: Monthly mean albedo (α) of farm 14362 in California, USA. The albedo of the surroundings (α_{SUR}) in green, the albedo of the solar farm (α_{PV}) in orange and the albedo difference ($\Delta\alpha_{PV-SUR}$) in blue. The light-coloured lines show the uncorrected data, while the dark-coloured lines indicate the bias-corrected data. The monthly values represent the average of all analysed images acquired during that month across a 3-year period.

The albedo difference is the same for both the corrected and uncorrected data. This outcome is expected, since the applied bias correction is identical in both regions. Both regions exhibit a similar seasonal pattern in albedo values, which leads to a nearly constant albedo difference throughout the year. If the surrounding areas consist of natural surfaces, seasonal variation is to be expected. This applies to the example farm shown in Figure 3.4. The seasonality of the albedo in the PV region could be attributed to the natural surface area between the PV modules. This would mean a less strong seasonality in the PV region. The absolute value of the difference increases in winter for the example farm. This is when both the PV albedo and the surroundings albedo increases, indicating that the PV farm seasonality is slightly less pronounced. Another possible explanation for the seasonality in the PV region is that the bias correction is not optimal. An alternative relationship between the bias in albedo estimation and the solar zenith angle could result in a more stable PV albedo value throughout the year.

To examine the expected seasonal behaviour, Figure 3.5 presents the three-year average monthly albedo measured at the SURFRAD stations. This is the same measurement data that was used in Chapter 2. A seasonal trend is evident, with albedo rising approaching winter and declining approaching summer. Figure 3.4 presents the same seasonal pattern after applying the bias correction. Consequently, the bias correction was implemented in all subsequent analyses in this chapter.

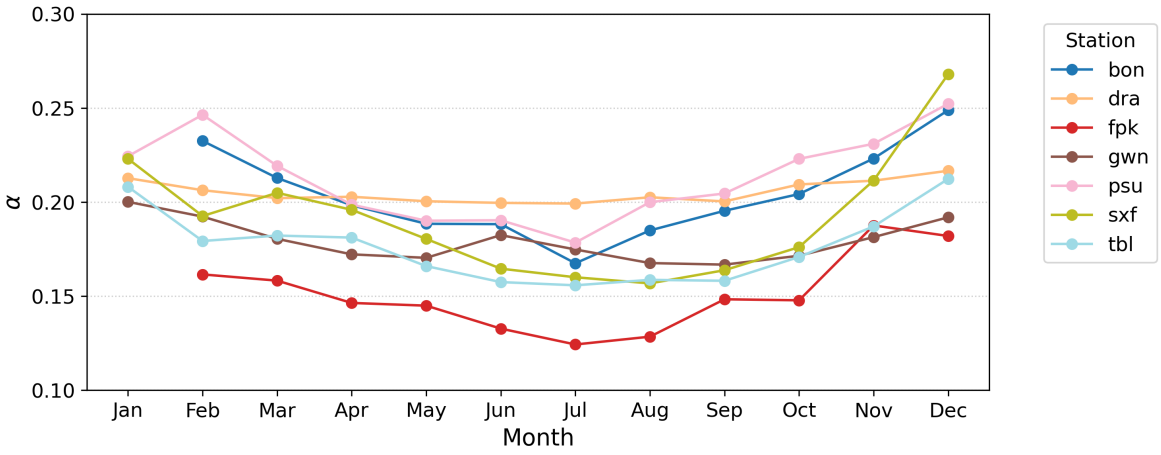

Figure 3.5: Three year monthly surface albedo averages for the SURFRAD stations measurements. The y-axis shows the measured albedo (α) and the x-axis the month. For each month between 2022-10-01 and 2025-10-01 a maximum of one albedo measurement is considered. Note that the spacing of the y-axis differs from that in Figure 3.4. A seasonal pattern of lower albedo in the summer months and higher albedo in the winter months can be observed.

Figure 3.6 shows the monthly IQR mean and the monthly mean of PV region albedo pixels. The albedo values are from the PV region of farm 14362 in California. In the top graph, the blue line displays the mean albedo value of all pixels within the PV region of the satellite image, while the purple line indicates the mean of the IQR of the albedo pixels in the same PV region. In the lower graph, the red line represents the monthly difference between the IQR mean and the overall mean albedo values. For every month, the mean albedo values based on the IQR are lower than the overall monthly mean values. This can by explain by the fact that the IQR omits certain high outlier albedo pixels. These high outliers could arise either because of glare or because of higher albedo surfaces between the PV modules. However, the darkest pixels are also excluded. If the excluded dark pixels are actual PV pixels, the true PV albedo could be even lower than the IQR mean suggests.

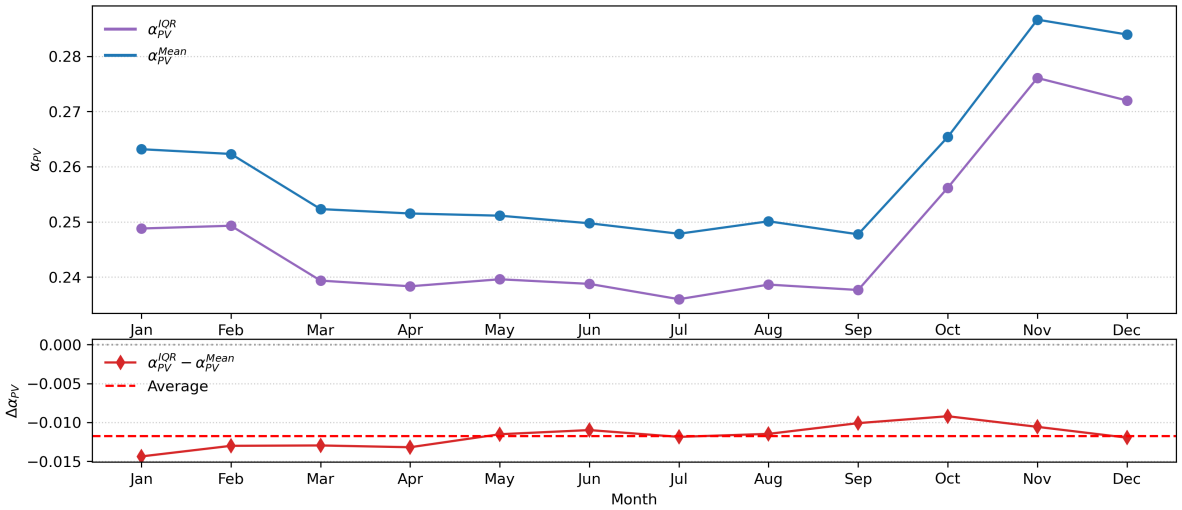

Figure 3.6: Monthly averages values of the PV albedo (α_{PV}) calculated as the mean of the interquartile range pixels within the PV region (α_{PV}^{IQR}) in purple and the overall mean of all pixels within the PV region (α_{PV}^{Mean}) in blue. Below the difference between these values is shown ($\Delta\alpha_{PV}$) in red. The average difference over all months is indicated with the dashed red line. The monthly values represent the average of all analysed images acquired during that month across a 3-year period. The values for farm 14362 are displayed.

While Figure 3.6 illustrates the difference between the IQR mean and the overall mean of albedo pixels for an individual farm, Figure 3.7 presents a box plot of these differences across all farms averaged over the entire analysis period. On the left in red are the differences for the PV region, and on the right are the results for the surrounding region. As illustrated by the PV region box plot, in over 75% of farms the IQR mean yields a lower albedo value than the overall mean. Since the expected PV albedo is low, outliers with high albedo values can show large difference, influence the overall mean more strongly than outliers with low albedo values. The green box plot representing the surrounding region shows a broader spread for all its data points, with its centre located closer to 0. For most of the farms, the difference between the IQR mean and the overall mean falls within the range of +0.01 to −0.01, indicating a more uniform distribution of surrounding albedo pixels. However, the outliers shown in the box plot reveal that the IQR mean omits very high and very low albedo pixel values in the surrounding region. A high variety in albedo for the surrounding region pixels could be explained by the surface types. While some farms are situated in uniform grassland areas, others are established on large rooftops in urban areas, surrounded by highly diverse environments. Excluding the farms in urban areas could improve the results.

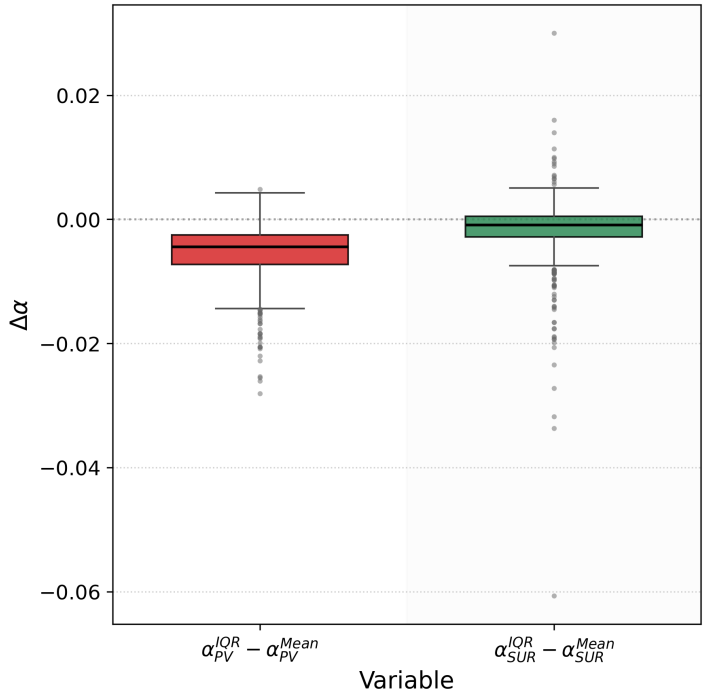

Figure 3.7: Box plot illustrating the difference between the mean albedo calculated from pixels within the interquartile range and the mean albedo calculated from all pixels for the PV area ($\alpha_{PV}^{IQR} - \alpha_{PV}^{Mean}$) and for the surroundings area ($\alpha_{SUR}^{IQR} - \alpha_{SUR}^{Mean}$) across all farms. The change is albedo ($\Delta\alpha$)is shown on the y-axis.

Although farm 14362 in Figure 3.4 exhibits the expected behaviour, not all farms follow this pattern. Figure 3.8 presents an example of a farm that displays unanticipated behaviour. The upper panel in the figure presents the monthly albedo for both the PV area and the surrounding area of farm 108224 in California, USA. In October, the albedo over the PV site displays a pronounced peak, resulting in a positive albedo difference as indicated in blue. The lower panel of the figure displays six satellite images of the farm. The top row images from 2022-10-23, 2023-10-23, and 2024-10-22 display satellite observations that produced elevated albedo values in the PV region. In contrast, the satellite images in the bottom row from 2022-10-25, 2023-02-05, and 2024-10-19 provide views that are more representative of the farm. The top row of satellite images suggest high specular reflectance. All three images were taken on the same date, considering that 2024 was a leap year, suggesting the relevance of the exact position of the sun in the sky. It seems that the tilt and orientation of the solar farm, together with the sun's azimuth and zenith angles, result in specular reflection directed toward the S2 satellite. This could explain why only the PV albedo shows a peak, while the surrounding albedo remains relatively unaffected. This effect has also been observed for other farms.

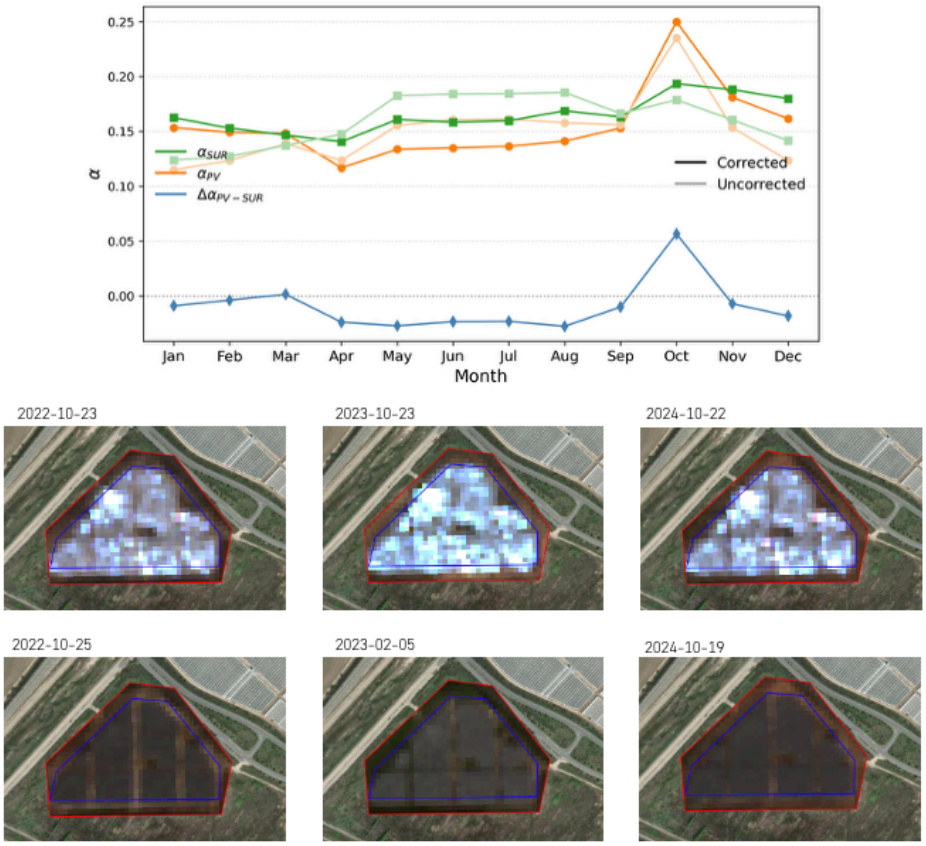

Figure 3.8: Example albedo (α) values of farm 108224 in California, USA. The top panel displays the monthly albedo time series of the PV region (α_{PV}) and its surroundings (α_{sur}), along with their difference ($\Delta\alpha_{PV-SUR}$) for each month. The light-coloured lines show the uncorrected data, while the dark-coloured lines indicate the bias-corrected data. The monthly values represent the average of all analysed images acquired during that month across a 3-year period. A strong peak in the PV albedo is observed in October. The bottom panel presents six sample satellite images of the farm. The three images in the top row of this panel correspond to the same day, taking leap years into account, in each of the three analysis years. These images exhibit pronounced glare, leading to high albedo values. The bottom row displays representative images of the farm from other times of the year.

Figure 3.9 presents a map of the mean albedo difference results per farm. The colour of each dot represents how the albedo of the PV region differs from the albedo of the surrounding area. The bias corrected values were used of the overall mean of the albedo pixels per region. In total, 104 solar farms showed higher albedo values than their surrounding pixels, whereas each of the remaining 396 farms exhibited a reduction in albedo. The greatest positive difference in albedo was observed for farm 99112 in India, where the albedo difference was 0.0686. The most pronounced negative difference in albedo was observed at farm 37405 in the USA, which exhibited an albedo difference of -0.3060. The largest and smallest albedo difference values lie outside the colour bar so that the plot remains easier to read. Although the solar zenith angle affects albedo, no latitudinal pattern can be identified. Local climate conditions and the type of land surface may be of greater impact on albedo.

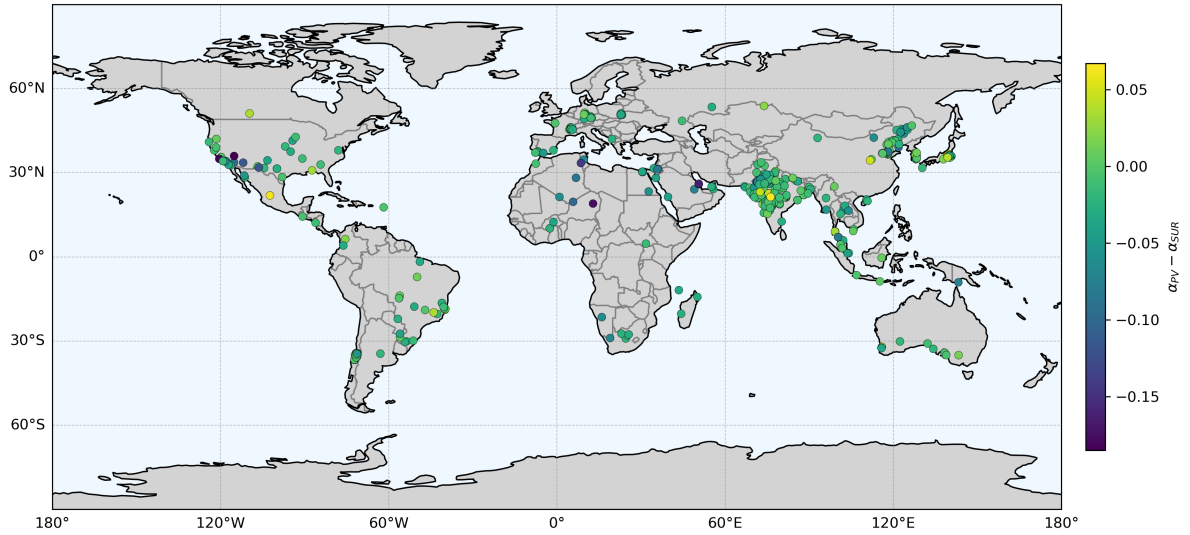

Figure 3.9: Map of the albedo difference between the PV region and surrounding region ($\alpha_{PV} - \alpha_{SUR}$) for each farm location. The minimum and maximum albedo difference values lie outside of the colour bar for readability. These values are 0.0686 for a farm in India and -0.3060 for a farm in the USA.

Figure 3.10 presents the same data as the map in Figure 3.9, but in the form of box plot. Next to the albedo difference for each farm, it also displays the box plots of the PV albedo and the albedo of the surrounding area. The median PV albedo of 0.169 is slightly lower than the surrounding value of 0.1825. Similarly, the overall mean PV albedo across all farms, 0.1799, is somewhat lower than the overall mean albedo of the surroundings, 0.1997. The larger difference in mean between the PV and the surroundings is caused by extremely high albedo outliers in the surroundings. The highest surrounding albedo value, 0.7152, was recorded at solar farm 37405, which also exhibited the greatest difference in albedo. This solar farm sits on a white flat rooftop, which accounts for its high albedo. The greatest PV albedo was observed for farm 83557, which is likewise situated on a white flat roof. The higher PV albedo of 0.4117 may be partly explained by the white surfaces between the solar panels. Additionally, increased specular reflection could also have played a role. The box plot of the albedo differences indicates a median value of -0.0152, around which most of the data points are clustered. However, there are also albedo differences which are substantially lower, resulting in a mean value of -0.0198. The largest albedo difference observed for farm 99112 in India could be attributed to the aoi_{PV}, which for a substantial part covers a light coloured rooftop without PV installation.

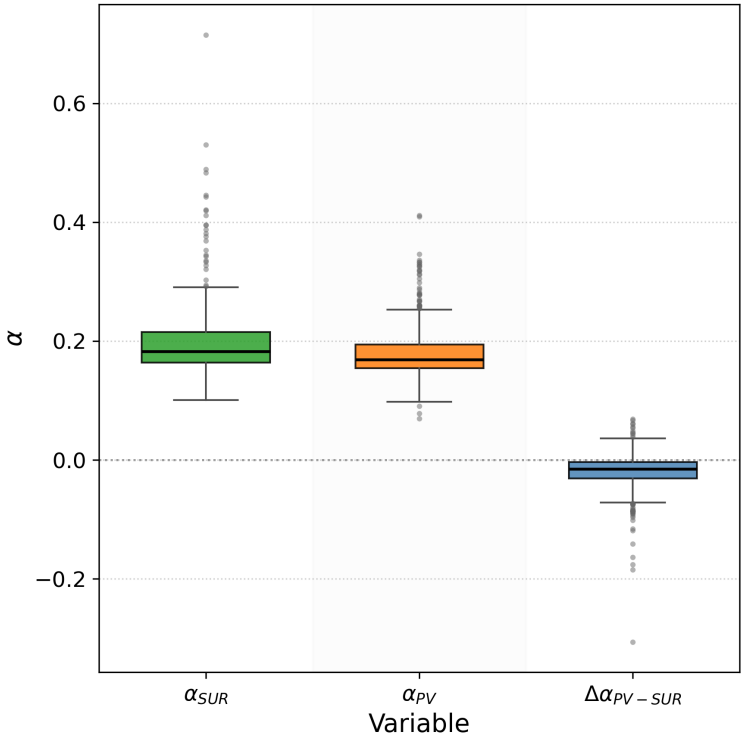

Figure 3.10: Box plot showing the PV region albedo (α_{PV}), the surrounding region albedo (α_{SUR}), and the albedo difference ($\Delta\alpha_{PV-SUR}$) for each farm, averaged over the three-year analysis period per farm.

3.4. Conclusion

In this chapter, the second research sub-goal was fulfilled: developing a model based on recent PV data which determines the change in albedo resulting from the deployment of solar farms. The model uses up-to-date solar farm data as its input, and this information can be easily revised in the future whenever a new TZ-SAM update is released. From the dataset 500 farms were analysed. The defined solar farm polygons of the TZ-SAM dataset, do not always perfectly align with the PV modules, which may introduce errors in determining the PV albedo. Because the solar farm's orientation and tilt are also unknown, it is difficult to detect and correct for any overestimation of albedo caused by direct specular reflection. The areas surrounding urban solar farms may be inappropriate for assessing albedo changes because of their heterogeneous characteristics. For most farms, the albedo difference showed a small decrease, with an average value of -0.0198. This is comparable to, but slightly larger than, the previously reported mean albedo difference of -0.016 reported by Xu et al. [25]. The median albedo difference found in this study was -0.0152, which is of the same order of magnitude but somewhat larger than the median albedo difference of -0.0128 reported by Wei et al. [31]. For further analyses drawing on these findings, limiting the dataset to farms with no detected problems could improve the quality of subsequent results.

4

Albedo-Climate Effect Model

This chapter addresses the third research sub-goal: The development of a model that can estimate and analyse the albedo–climate impact of solar farms worldwide, incorporating both their effective albedo and the local carbon intensity of electricity. The first section outlines the selection of farms that are suitable for further investigation. The second section focuses on how the effective albedo is determined. The third section describes the methods used to calculate the radiative forcing associated with a solar farm and to estimate the carbon break-even time for each solar farm. The final sections present the resulting findings and analysis, followed by the chapter's conclusion.

4.1. Farm Selection

In this chapter, only a subset of the farms analysed previously was used. This is because, despite stringent satellite image selection, some farms did not yield problem-free data. Figure 3.8 illustrates an example of such issues. To filter out farms affected by glare, such as the one shown in Figure 3.8, an upper limit was imposed on the change in albedo between consecutive months. It was assumed that, under normal conditions, the month-to-month change in albedo would not exceed 0.05. A total of 181 farms were identified with inter-month albedo differences greater than 0.05. Furthermore, the dataset was filtered based on a minimum number of images per farm. Each farm was required to have at least one image for every month within the 3-year analysis period. This requirement guarantees that each monthly average is based on a minimum of three images and that no months are missing. In total, 286 farms were found to have at least one month without any images during the 3-year period. Of these, 124 failed to satisfy either of the specified criteria. Therefore, applying these criteria yielded a subset of 157 farms. Figure 4.1 displays the locations of the selected farms in green, while the red dots represent the farms from the previous chapter that were not included. The farm subset continues to include every continent and remains fairly well spatially distributed.

A time series was generated for each farm in the subset. The starting point of this series was set exactly midway between the farm's 'constructed before' and 'constructed after' dates. For each farm, a lifetime of 25 years was assumed, so the time series extends over this 25-year period in monthly time steps. The monthly albedo values determined for each farm in the previous chapter were assigned to their corresponding months in the time series.

4.2. Effective Albedo

The previous chapter presents the absolute albedo estimates for both the PV area and the surrounding area of each farm. As the PV region contains active surface material, the effective albedo of this area was determined. Equation 4.1 was used to calculate the effective albedo of the PV region. This is the same equation as Equation 1.3 with a small adjustment. Since the polygon area of each farm is not entirely covered by PV modules, the ground cover ratio (GCR) was included in the function. Here

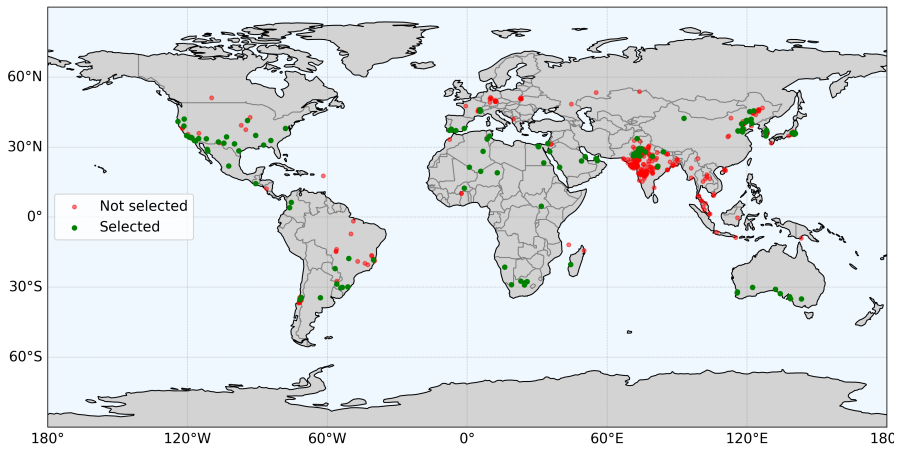

Figure 4.1: Map indicating the 157 farms out of 500 that have been selected for further analysis in chapter 4. The green indicates the selected farms while the red indicate the farms from the previous chapter that were not selected.

the GCR is the module area over the farm polygon area. Equation 4.2 was applied to compute η_{annu}. Because the effective albedo depends on the solar farm's annual efficiency, it varies over time.

$$\alpha_{eff} = \alpha + GCR \cdot \eta_{annu} \tag{4.1}$$

$$\eta_{annu}(t) = \eta_{PV} \cdot PR \cdot (1 - r_d \cdot t) \tag{4.2}$$

The parameters and constants in equation 4.2 are as follows:

- η_{PV} is the PV module efficiency.
- PR is the performance ratio of the solar farm.
- r_d is the degradation rate of the solar farm in % per year.
- t is the time is the same units as the degradation rate.

For all the parameter in Equation 4.2 a single, general estimate was applied across all farms. For the efficiency, this approach was taken because every farm was installed between 21 November 2020 and 27 September 2022. Since all installation dates fall within this two-year period, it was assumed that the efficiencies of the farms would be broadly comparable. An η_{PV} of 19.5% was selected [22] [73]. Similarly, due to the installation of the solar farms around 2021, the degradation rate was estimated at 0.5% per year [74]. Although this is an approximation, it was assumed that degradation proceeds at a constant, linear rate throughout the entire operational lifetime of the solar farm. Additionally, the PR was estimated from literature. A value of 0.75 was used for every farm [75][22].

The value of GCR varies from farm to farm and is not known. To obtain an estimate, five randomly selected farms were inspected visually. Figure 4.2 presents the set of images that were examined visually. The figure shows that only part of the area enclosed by the PV polygons represents active PV module surface. In all five images, the solar panel footprint and the farm polygon were delineated, and the number of pixels within each was determined to calculate the ground cover ratio. For the delineation the software WebPlotDigitizer was used [76]. Table 4.1 shows the ground cover ratio. The resulting average GCR was 0.58, and this value was applied to all farms.

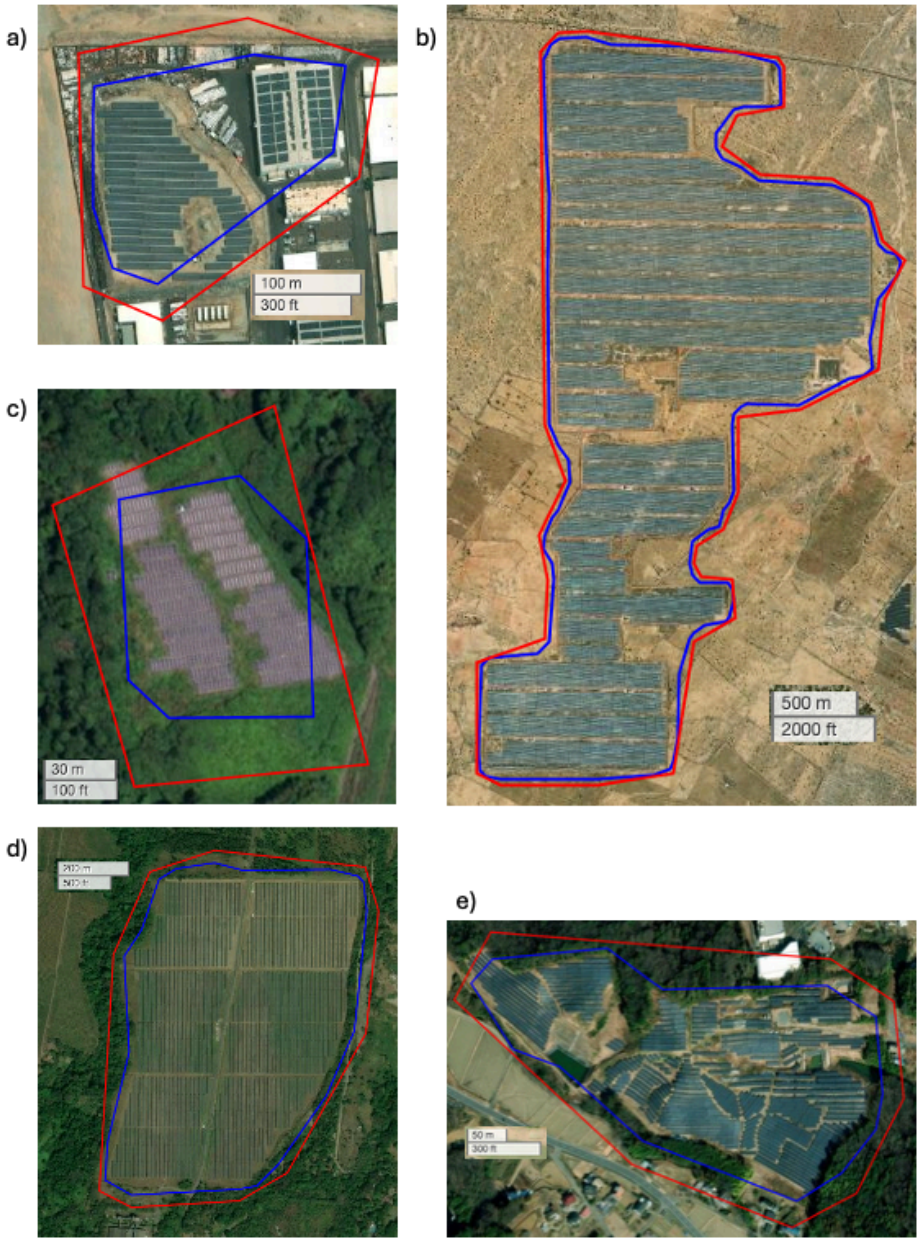

Figure 4.2: Satellite imagery of the five randomly selected farms used for the visual estimation of the ground cover ratio. The blue line represents the farm polygon. The farm IDs for these sites are: a) 1794, b) 36688, c) 25134, d) 64494, and e) 23520. Table 4.1 presents the determined ground cover ratios for each farm.

Table 4.1: The ground cover ratio (GCR) found for each of the five randomly selected farms. Figure 4.2 shows images of the farms. The average ground cover ratio across these 5 farms is 0.58.

Farm id	Figure 4.2	Country	GCR
1794	a	Saudi Arabia	0.48
36688	b	India	0.68
25134	c	Japan	0.50
64494	d	Guatemala	0.73
23520	e	Japan	0.51

4.3. Radiative Forcing & Carbon Break Even Time

Radiative Forcing due to Albedo Change

The radiative forcing associated with the albedo modification caused by the solar farms was calculated using Equation 1.4. The equation is repeated here. The calculations were performed for both the absolute and the effective albedo differences, for each month over the entire lifetime of the solar farm. Both types of albedo were examined, since earlier studies focused on absolute albedo, whereas effective albedo provides a more comprehensive representation of the climate effect. With this approach, the absolute albedo results can be compared with previous work, and the impact of using the effective albedo can be clearly demonstrated.

$$RF_{\Delta\alpha} = \frac{\sum_{m=1}^{12} k_{\Delta\alpha} \Delta\alpha_m}{12} \frac{A_{PV}}{A_E}$$

In Equation 1.4, repeated above, the radiate kernels by Huang et al. were used [77]. These kernels indicate the sensitivity of the climate to a change in albedo and represent a climatological state [78]. The kernel values by Huan et al. are based on climate data from 2011 till 2015, as these years are representative for the current climate and include a strong el niño and la niña year. The spatial resolution of the kernels is 2.5° by 2.5°. Figure 4.3 shows a map with the yearly kernel values. In this analysis the monthly values were used. The kernels all al negative as a positive change in albedo causes negative radiative forcing, cooling. In Equation 1.4 the Earth's surface was taken as $510 \times 10^{12}\,\mathrm{m}^2$ [79].

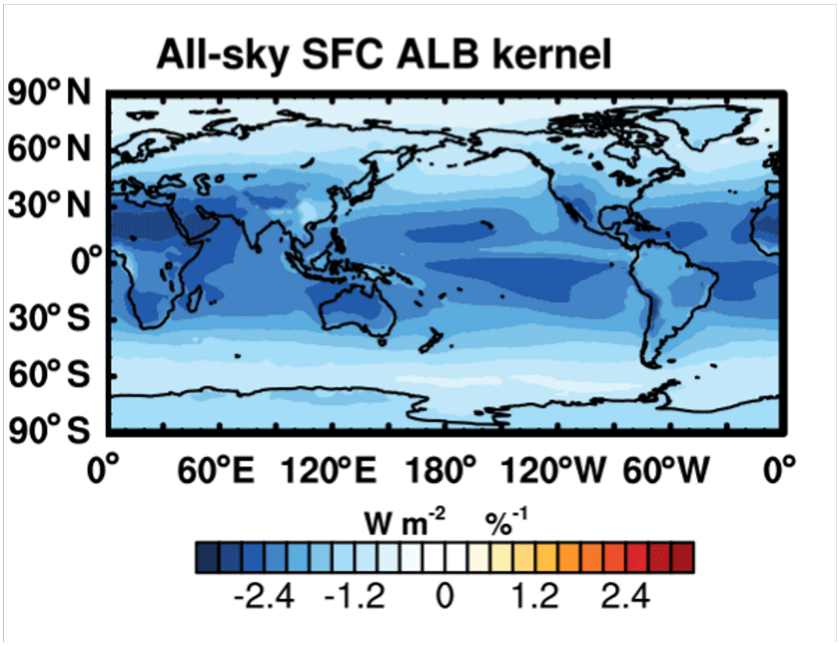

Figure 4.3: All skies radiative forcing surface (SFC) albedo (ALB) kernel yearly value in $\mathrm{W/m^2}$ %. Values represent the radiative forcing response to a change in surface albedo in $\mathrm{W/m^2}$%. The kernels are based on climate data from 2011 till 2015. The negative figures indicate a negative radiative forcing for a positive albedo change. Figure adapted from Huang et al. [78].

Radiative Forcing due to Avoided Emissions

To quantify the radiative forcing associated with the emissions avoided by the solar farm, equation 1.5, repeated below, was applied. A values was determined for each month over the entire lifetime of the solar farm. The background concentration of co_2 determines the magnitude of the climate response to additional co_2 emissions. In this work, a background concentration of 425 ppm was assumed. This value is similar to the background concentration in 2024 [80]. With large differences the background concentration will start to play a significant role. However, because future conditions are uncertain, and due to the scope of this study, here a constant background concentration was assumed. Using this background concentration yields a value of k_{CO_2} equal to $1.65 \times 10^{-15}\,\mathrm{W/m^2\,kg\ (CO_2)}$ [80]. The avoided emissions per month, $E_{CO_2}(t)$, attributable to the solar farm were calculated using equation 4.3. Here, the emissions are shown as a negative value because they were avoided rather than produced.

$$RF_{CO_2}(t) = k_{CO_2} \int_{t'=0}^{t'=t} E_{CO_2}(t') IRF_{CO_2}(t - t') dt'$$

$$E_{CO_2}(t) = -P_{inst} \cdot Y_{spec}(t) \cdot N_{days}(t) \cdot (1 - r_d \cdot t) \cdot CI_{elec} \tag{4.3}$$

The parameters and constants in equation 4.3 are as follows:

- P_{inst} is the installed capacity of the solar farm in kWp.
- Y_{spec} is the daily estimated specific yield averaged over each month kWh/kWp d.
- N_{days} the number of days in the month.
- CI_{elec} is the local carbon intensity of electricity in kg/kWh (CO_2–eq)

The installed capacity of each farm was taken from the solar farm dataset [65]. Monthly estimates of specific yield were obtained from the Global Solar Atlas, accessed through [81]. These data represent long-term averages up to 2021. The local carbon intensity of electricity provided by Ember was used [82]. Appendix Figure E.2 shows the local carbon intensity of 2024 used in this study.

To quantify the radiative forcing of the avoided emissions, the CO_2 impulse response function from Joos et al. was applied [30]. Equation 4.4 presents the function. In this study updated coefficients for a background concentration of 425 ppm were used [80]. The function is applicable for time scales between 0 and 2000 years. Table 4.2 shows the coefficients that were applied. Additionally, Figure 4.4 shows the impulse response function. The function visualises the decay of co_2 in the atmosphere.

$$IRF_{CO_2}(t) = a_0 + \sum_{i=1}^{n} a_i \exp \frac{-t}{\tau_i} \tag{4.4}$$

Table 4.2: The coefficients of the CO_2 impulse response function for a background concentration of 425 ppm of around 2024 [80]. Equation 4.4 shows the function. The a_i coefficients are dimensionless scaling factors that add up to 1, the τ_i coefficients represent characteristic time scales measured in years, and t is likewise expressed in years.

i	a_i	τ_i
0	0.2488	-
1	0.2453	6.211
2	0.2798	60.65
3	0.2261	536.3

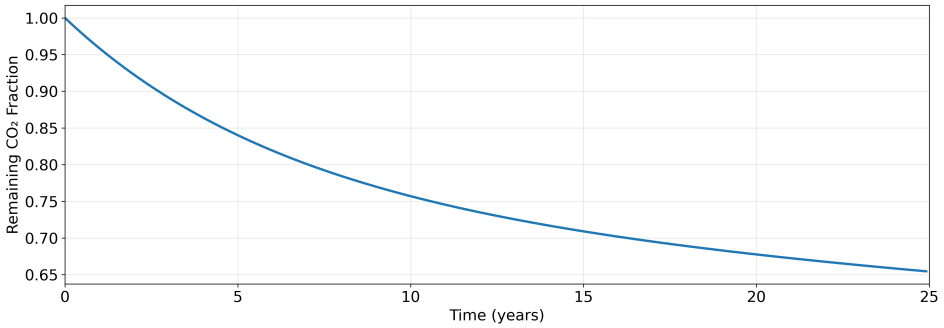

Figure 4.4: The impulse response function of CO_2 which indicates the fraction of CO_2 remaining in the atmosphere after a emission peak. Equation 4.4 show the function of the graph and Table 4.2 shows the values of the coefficients used. The x-axis shows the time in years after a emission peak.

Radiative Forcing due to Embodied Emissions

To capture the full climate impact of solar farms, the embodied emissions were also considered. A life cycle analysis was applied to derive a single representative carbon intensity value per unit of installed capacity for all farms. Because all solar farms examined in this study were installed around 2021, an LCA from 2021 was used, covering the cradle-to-grave phase while excluding balance-of-system components and maintenance. The LCA reports values for three different regions for two kinds of solar panels. The average of these six values was taken to obtain a general estimate applicable to all farms. This resulted in a value of 592 kg/kWp [22]. Using this value together with the installed capacity allowed the estimation of the embodied emissions for each farm. The radiative forcing of the embodied emissions (RF_{farm}) was calculated using equation 1.5, assuming that all embodied emissions occur as a single peak in the first month after the solar farm is installed.

Carbon Break Even Time

For every farm, the net radiative forcing per month was calculated using equation 4.5. The carbon break-even time ($CBET$) was defined as the moment when the cumulative net radiative forcing first falls below zero. The CBET was calculated as the first value of $CBET$ for which Equation 4.6 holds. At this time, the overall positive climate impacts of the solar farm outweigh the negative ones. The net radiative forcing and the carbon break even time of each farm was determined both considering the absolute albedo change and the effective albedo change.

$$RF_{net}(t) = RF_{\Delta\alpha}(t) + RF_{CO_2}(t) + RF_{farm}(t) \tag{4.5}$$

$$\sum_{i=1}^{CBET} RF_{net}(i) \leq 0 \tag{4.6}$$

Carbon Intensity of Albedo Change

To obtain a more comparable metric for the climate effect of albedo change, the carbon intensity of electricity associated with the albedo change ($CI_{\Delta\alpha,E}$) was calculated using Equation 4.7 [83] [31]. In addition, the carbon intensity per installed capacity in kWp ($CI_{\Delta\alpha,P}$) was calculated, using Equation 4.8. The results are expressed as carbon intensities, as these units are commonly applied in life cycle assessments of PV systems and the outcomes of this study represent an additional climate impact, thereby allowing direct comparison with existing LCA studies. Furthermore, in Chapter 1, an order-of-magnitude estimate indicated an expected $CI_{\Delta\alpha,E}$ of approximately 2.5 g/kWh (CO_2−eq).

$$CI_{\Delta\alpha,E} = \frac{RF_{\Delta\alpha}}{k_{CO_2} \cdot AF \cdot Y_{total}} \tag{4.7}$$

$$CI_{\Delta\alpha,P} = \frac{RF_{\Delta\alpha}}{k_{CO_2} \cdot AF \cdot P_{inst}} \tag{4.8}$$

In Equation 4.7, $RF_{\Delta\alpha}$ represents the average radiative forcing caused by the albedo change. Here too, both the absolute change in albedo and the effective change in albedo were considered. Furthermore, AF denotes the airborne fraction, representing the portion of the initial perturbation that remains after a specified number of years. Following previous studies, the value of AF used in this work is 0.44 [31][84]. The total yield (Y_{total}) of each farm was determined using Equation 4.9. Here, LT, is the lifetime of the solar farm of 25 yr.

$$Y_{total} = \sum_{t=0}^{LT} (P_{inst} \cdot Y_{spec}(t) \cdot N_{days}(t) \cdot (1 - r_d t)) \tag{4.9}$$

4.4. Validation & Sensitivity Analysis

For validation, the model's CBET results were compared with those reported by Wei et al [31]. Appendix Figure E.1 presents the CBET outcomes obtained by Wei et al. The model was executed with parameter settings chosen to mirror those used by Wei et al. as closely as possible. For the validation run, the carbon intensity of electricity from coal-fired power plants was set to 900 g/kWh (CO_2-eq.), consistent with Wei et al. In addition, because Wei et al. do not include either embodied emissions or the degradation rate of solar farms, both of these parameters were set to zero in the validation scenario. The mean absolute albedo change determined in this study was scaled to match the mean absolute albedo change reported by Wei, $\Delta\alpha_{abs} = -0.0144$. To accomplish this, all albedo changes in the present model were uniformly scaled to 48% of their value for the validation run. Since the CBET calculations by Wei et al. assume a background CO_2 concentration of 410 ppm, k_{CO_2} was chosen as 1.71×10^{-15} W/m^2 kg (CO_2), which was determined with the equations provided by Jeltsch-Thömmes et al. [80]. All other model parameters were kept unchanged. This is because some parameters were not reported by Wei et al., or were excluded due to methodological differences between this model and theirs.

To determine the robustness of the model and its results, a sensitivity analysis was carried out for both the effective albedo and the carbon break-even time (CBET) results. The CBET results considering both the effective albedo and the absolute change in albedo were evaluated. In both sensitivity analyses variations in PV module efficiency, ground cover ratio, performance ratio, degradation rate, and PV system lifetime were examined. All variables were varied by ±10% from their baseline values, except for the PV lifetime value, because the model requires lifetime to be provided as an integer value. Additionally, the sensitivity of the CBET is evaluated with respect to the CO_2 radiative kernel, the installed PV power, the specific solar farm yield, the local carbon intensity of electricity, the embodied carbon intensity of electricity of the solar farm, and both the absolute and effective albedo change due to the solar farm. All variables were again perturbed by ±10% from their baseline values, with the exception of the CO_2 radiative kernel, which was adjusted by only ±5% to better reflect realistic values of the CO_2 radiative kernel [80]. All variations were performed individually in order to assess the effect of each variable on the results.

4.5. Results

Effective Albedo

Figure 4.5 presents an example of the absolute and effective albedo of the PV region time series of a single farm. The orange line indicates the absolute albedo change and blue the effective albedo. Both lines show a repeated seasonal pattern which was determined in the previous chapter. The effective albedo shows a linearly decaying offset compared to the absolute albedo. This outcome is to be expected as the effective albedo is determined using constant parameters and a single linearly decreasing term representing degradation. In the time series were to continue the effective albedo would approach the absolute albedo. At the end of its life time the farm reaches 87.5% of its original capacity. The difference between the effective albedo and the absolute albedo in the first month is 0.085 and is identical for all farms. Averaged over all months during the PV lifetime, the offset is 0.080.

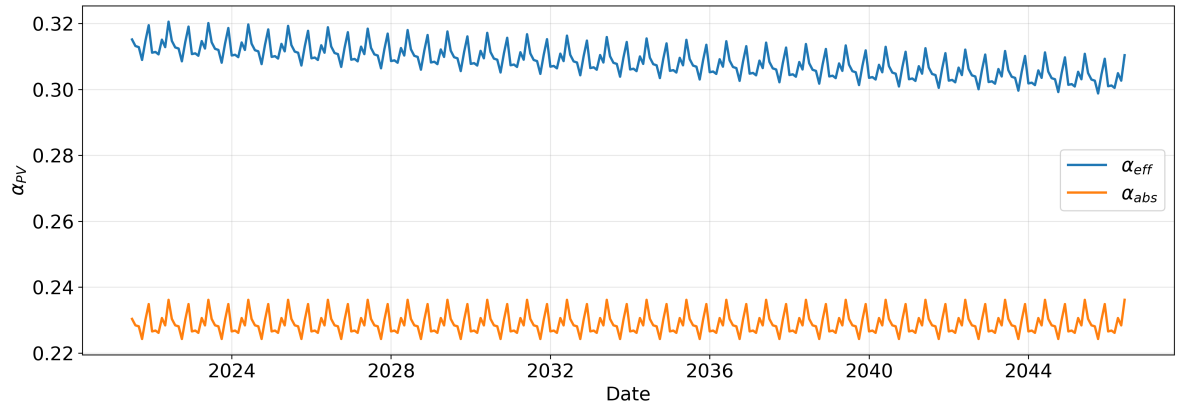

Figure 4.5: The albedo time series of a single solar farm over its modelled lifetime. The x-axis show the mean albedo of the PV region (α_{PV}) and the y-axis the date in years. The example is of farm 12351. The absolute albedo (α_{abs}) is indicated in orange and effective albedo (α_{eff}) in blue.

Figure 4.6 shows two maps displaying the mean absolute and effective albedo for all farms in the analysed subset. Both maps share the same colour bar scale to make differences between the values directly comparable. Underneath each map, a histogram illustrates the distribution of PV albedo values. The histograms show a uniform shift from the absolute PV albedo values to the effective PV albedo across all farms. The average absolute PV albedo across all 157 farms is 0.190, whereas the average effective PV albedo across all 157 farms is 0.270. This offset was modelled to be identical for all farms which can be seen clearly in the histograms in Figure 4.6. However, in reality the values of η_{PV} and GCR depend on the specific configuration of each farm and PR depends on local climate and farm configuration. Although the calculation method uses this generalization, it still provides an estimate of the effective albedo that can be incorporated into climate impact assessments, whereas previous studies have not accounted for effective albedo in such evaluations.

The top map in Figure 4.7 shows the spatial distribution of the absolute albedo change. This absolute albedo change is derived from the difference between the absolute albedo within the PV areas and that of their surrounding regions. The histogram beneath displays how this absolute albedo change is distributed across the farms. The mean absolute albedo change across the 157 farms is 0.0496. The map below illustrates the change in effective albedo, calculated as the difference between the effective albedo of the PV installations and the absolute albedo of the surrounding areas. The histogram beneath it once more displays how this effective albedo change is distributed across the various farms. The mean effective albedo change across the 157 farms is -0.0299. The albedo change values shown are time averages over the lifetime of each solar farm. The results indicate that, for the majority of solar farms, absolute albedo decreases due to solar farm deployment which suggest a warming effect. On the other hand, when the effective albedo is considered an increase is observed, which indicates that the solar farms could have a cooling effect. The results underscore the relevance of considering the effective albedo change.

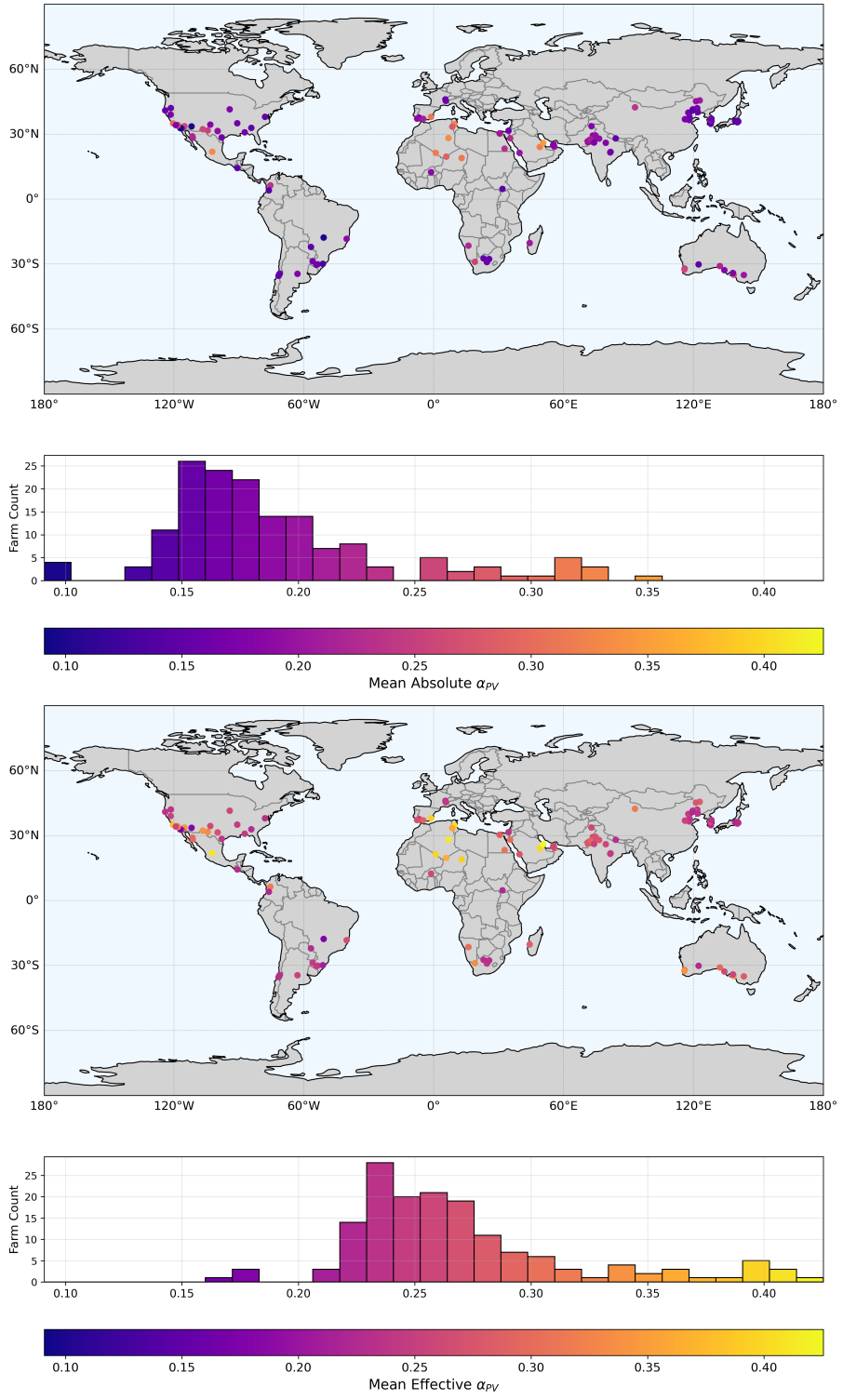

Figure 4.6: Map indicating the mean albedo of the PV region (α_{PV}) of each of the 157 farms. In the top map the mean absolute albedo is depicted and in the bottom map the mean effective albedo. Maps share a colour bar scale. Below each map a histogram shows the distribution of the PV region albedo across the farms. The albedo values presented are time averages taken over the modelled lifetime of the solar farm. Across all farms, the average absolute albedo is 0.190 and the median is 0.178, while the average effective albedo is 0.270 with a median of 0.258.

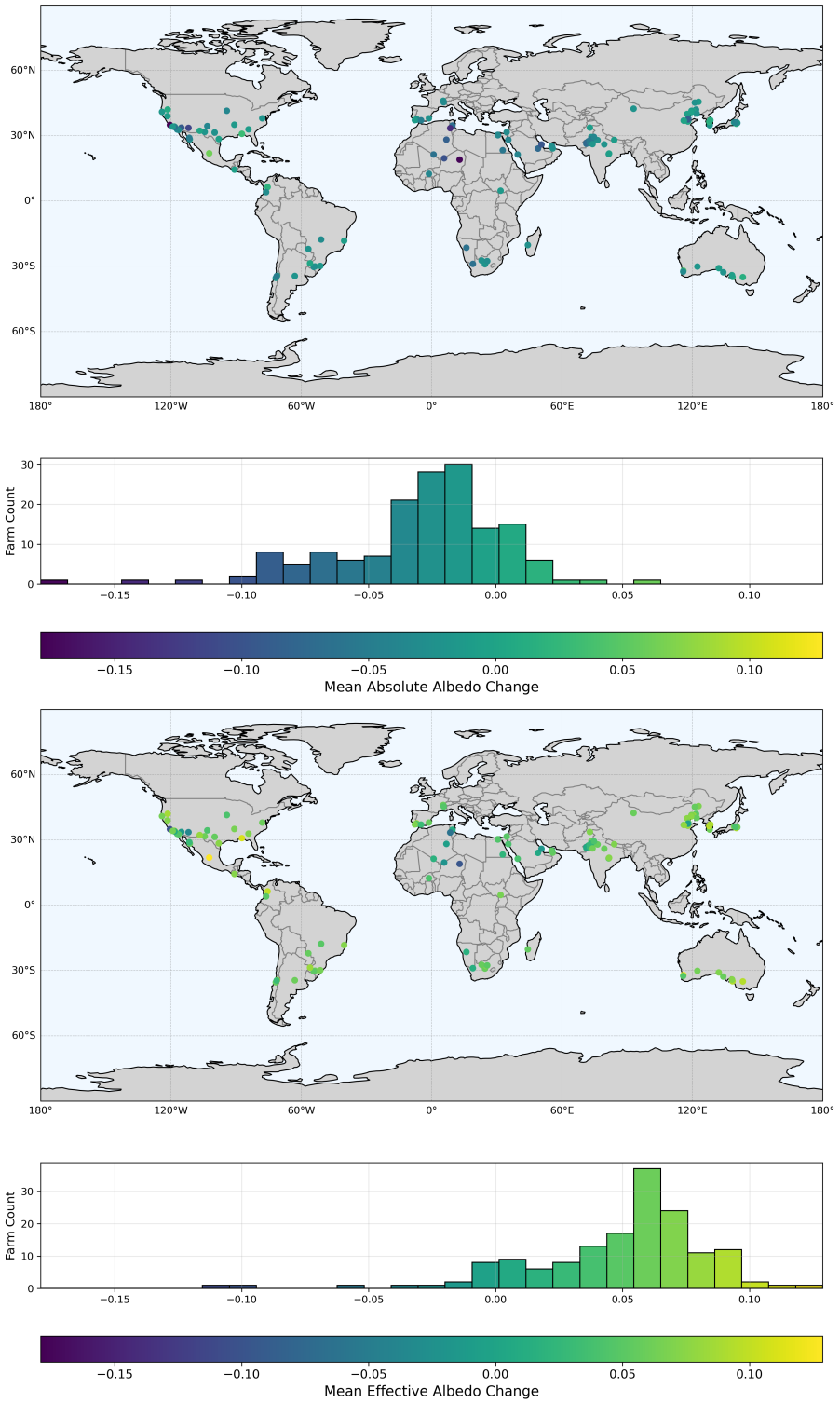

Figure 4.7: The top map shows the time-averaged absolute change in albedo for each farm, with the distribution of these values presented in the histogram below it. Across all 157 farms, the mean absolute albedo change is −0.0299 with a median of −0.0229. The lower map shows the time-averaged effective albedo for each farm, with its variability illustrated in the corresponding histogram underneath. Across all 157 farms, the mean effective albedo change is 0.0496 with a median of 0.0566. All plots use a common colour scale.

Table 4.3 reports the results of the sensitivity analysis for the time-averaged effective albedo, averaged across all farms. The parameters η_{PV}, GCR, and PR exhibit the same low sensitivity behaviour. For each of the parameters, a variation of $\pm 10\%$ results in a change of approximately $\pm 3\%$ in the calculated effective albedo. This occurs because all three parameters influence the effective albedo linearly and in an the same manner. The r_c and LT parameters exhibit an even lower sensitivity. A longer lifetime permits more extensive degradation, which leads to a reduced time-averaged effective albedo. Likewise, a higher degradation rate results in greater overall degradation by the end of the lifetime, also producing a lower time-averaged effective albedo.

Table 4.3: Results of the sensitivity analysis of the effective albedo (α_{eff}) of the PV region of the solar farms. The effective albedo values are presented as averages calculated over each farm's full operational lifetime and then averaged across all farms. The first row in the table represents the base scenario. The sensitivity of the following variables were analysed: the PV module efficiency (η_{PV}) in (%), the ground cover ratio (GCR), the performance ratio (PR) and the degradation rate (r_d) in % per year. All variables used in this sensitivity analysis are fixed constants that apply uniformly across all farms. The percentage variation in the effective albedo relative to the baseline, caused by changes in the variables, is presented in the $\Delta\alpha_{eff}$ (%) column.

Variable	Base Value	Δ Variable (%)	α_{eff}	$\Delta\alpha_{eff}$ (%)
-	-	-	0.270	-
η_{PV}	19.5	+10	0.278	+2.95
η_{PV}	19.5	-10	0.262	-2.95
GCR	0.58	+10	0.278	+2.95
GCR	0.58	-10	0.262	-2.95
PR	0.75	+10	0.278	+2.95
PR	0.75	-10	0.262	-2.95
r_d	0.5	+10	0.269	-0.20
r_d	0.5	-10	0.270	+0.20
LT	25	+12	0.269	-0.24
LT	25	-12	0.271	+0.24

Radiative Forcing & Carbon Break Even Time

Figure 4.8 presents the results of the time average radiative forcing due to the change in albedo for each farm in W/m^2. The upper map presents the $RF_{\Delta\alpha}$ linked to the absolute albedo change, with a histogram beneath it illustrating the distribution of the results. The lower map displays the $RF_{\Delta\alpha}$ based on the effective albedo change, and the histogram below this map shows the corresponding result distribution. The maps and histograms share a colour bar scale to enable direct comparison of the values. The RF values are averaged over the whole earth. Among all RF values linked to both effective and absolute albedo changes, the 20% extremes fall outside the colour bar range. This enhances the map's readability by preventing the most extreme values from overshadowing the rest of the data. The radiative forcing associated with the absolute PV albedo is largely positive, whereas the forcing related to the effective PV albedo is predominantly negative. Across the 157 farms, the average radiative forcing linked to the absolute change in albedo is 2.032×10^{-8} W/m^2, while the average radiative forcing linked to the effective change in albedo is -1.227×10^{-8} W/m^2. This shows that when the absolute albedo is considered, the albedo change primarily leads to climate warming, whereas when the effective albedo is considered, the albedo change instead results in a cooling effect. It is apparent that, unlike the PV-region albedo values shown in Figure 4.6, the difference between the two maps is no longer represented by a uniform offset. Some farms show strongly positive RF when absolute albedo is used, but strongly negative RF when effective albedo is considered. This may occur because the farm size is factored into the RF, so even a small difference between absolute and effective albedo change can result in a large difference in RF.

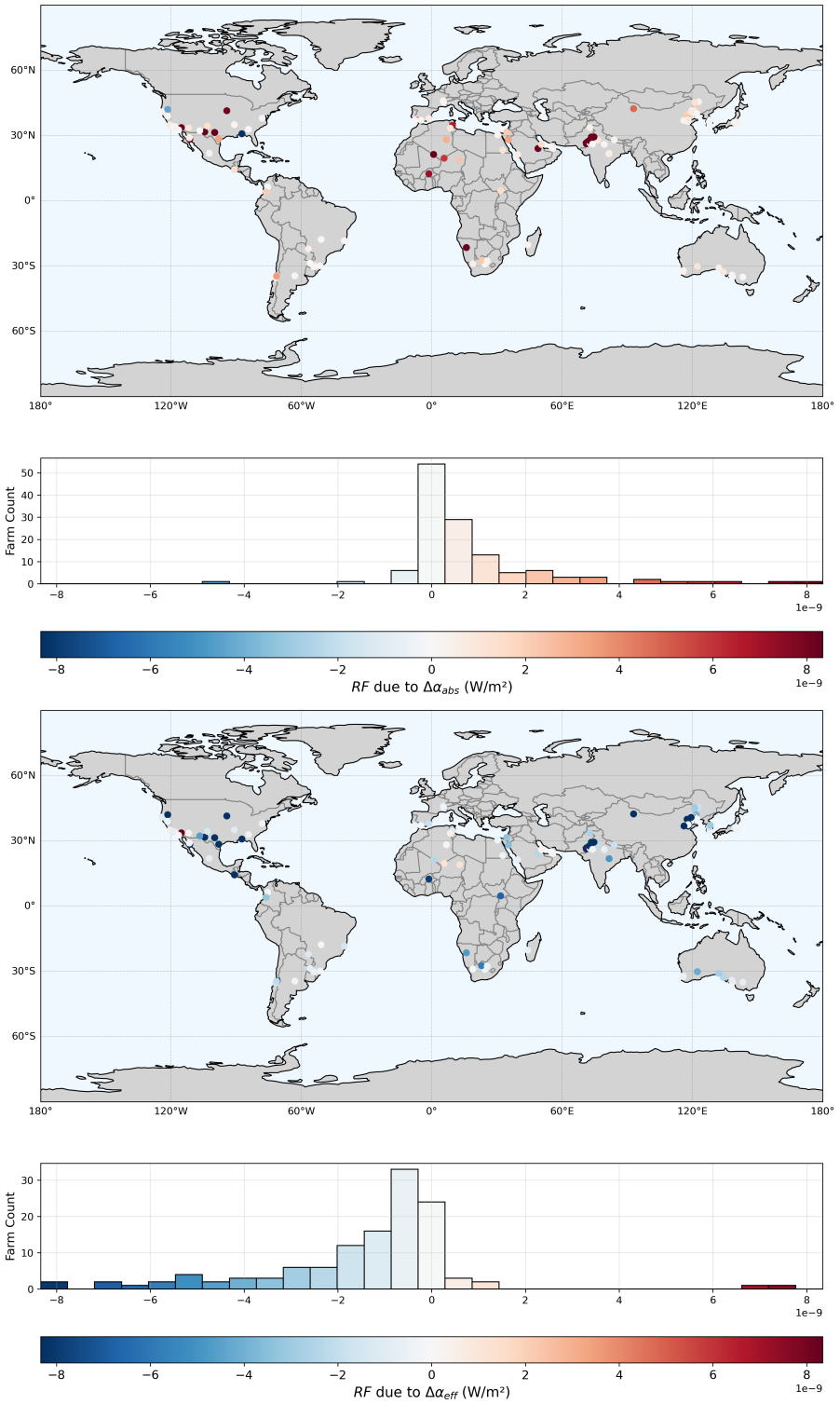

Figure 4.8: The top map displays the radiative forcing resulting from the absolute albedo change (RF due to $\Delta\alpha_{abs}$) caused by solar farm deployment, averaged over time for each individual farm. The accompanying histogram below depicts the distribution of these values. The bottom map presents the radiative forcing due to the effective albedo change (RF due to $\Delta\alpha_{eff}$) associated with solar farm deployment, also averaged over time for each individual farm. The histogram underneath shows the distribution of these corresponding results. The colour scale is identical across all plots to allow direct comparison. For clarity, the 20% most extreme values in the combined datasets are excluded from the colour bar range. Across all 157 farms, the mean radiative forcing associated with the absolute albedo change is $2.032 \times 10^{-8}\,\mathrm{W/m^2}$ with a median of $4.941 \times 10^{-10}\,\mathrm{W/m^2}$, whereas the mean radiative forcing associated with the effective albedo change is $-1.227 \times 10^{-8}\,\mathrm{W/m^2}$ with a median of $-1.222 \times 10^{-9}\,\mathrm{W/m^2}$.

Figure 4.9 depicts the time evolution of the various radiative forcing components associated with a solar farm. The upper panel shows the RF arising from $\Delta\alpha_{abs}$ together with RF_{farm}, RF_{CO_2}, and the corresponding RF_{net}. The lower panel presents the RF due to $\Delta\alpha_{eff}$, again plotted alongside RF_{farm}, RF_{CO_2}, and the corresponding RF_{net}. The RF values indicate averages computed over the surface of the Earth. The RF associated with $\Delta\alpha_{eff}$ is offset relative to the RF associated with $\Delta\alpha_{abs}$ because of how the effective albedo is computed. The linear increase observed in the RF from $\Delta\alpha_{eff}$ arises from the linear degradation rate applied in the effective albedo calculation. The seasonal cycle of the absolute-albedo-related RF differs from that of the effective-albedo-related RF because, in the latter case, the seasonal variation of the albedo-change radiative kernel also plays a role. Both graphs display the same RF_{farm} and RF_{CO_2}, since these radiative forcing effects are not affected by albedo. When the effective albedo is considered, the net radiative forcing of the example farm is already negative from its installation data, signifying a cooling influence over the entire farm lifetime.

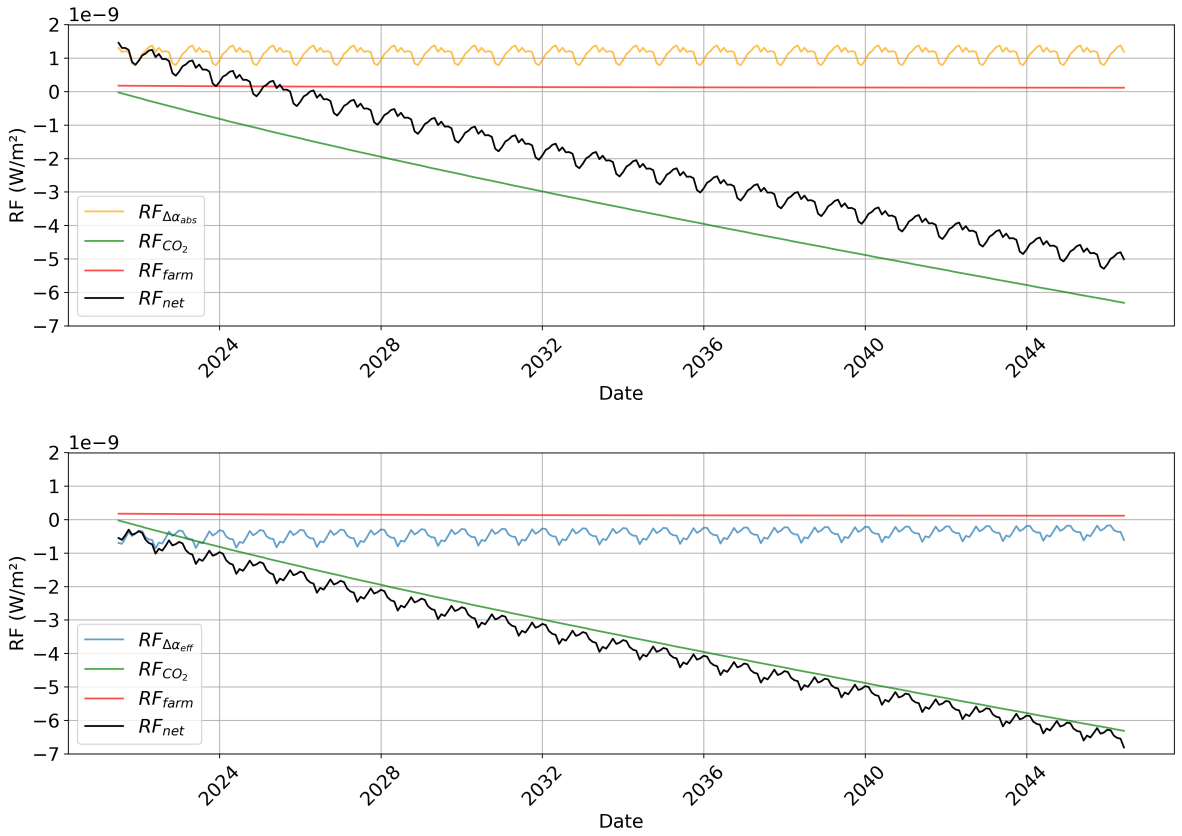

Figure 4.9: Radiative forcing time series of example farm 12351 considering the absolute PV region albedo in the top graph and the effective PV region in the bottom graph. The radiative forcing associated with the absolute albedo change $RF_{\Delta\alpha_{abs}}$, the effective albedo change $RF_{\Delta\alpha_{eff}}$, the embodied emissions RF_{farm}, the avoided emissions RF_{CO_2}, and the net radiative forcing RF_{net} are shown. The x-axis shows the date in years and the y-axis the radiative forcing (RF) in W/m^2. The RF values represent averages taken across the surface of the Earth.

The maps in Figure 4.10 show the carbon break-even time for each farm. The top map illustrates the CBET calculated from the absolute albedo change, with a histogram below indicating the distribution of these values. The bottom map presents the CBET derived from the effective albedo change, again accompanied by a histogram underneath that depicts the distribution of the results. The maps and histograms share a common colour bar scale, to allow the results to be compared directly. Farms that failed to achieve their CBET within the 25-year lifespan were nonetheless treated as having a 25-year CBET. This was the case for 12 farms in the top map considering the absolute albedo. This can occur when there is a substantial change in albedo, for example due to a highly reflective surrounding surface, and when the local electricity supply has a low carbon intensity. An example of such a farm in farm 14362 located in California, USA, also shown in Figure 3.3. The average CBET computed with the absolute albedo was found to be 7.79 yr in this study, with a median of 4.92 yr. The large difference between mean and median value indicates a large influence of outliers on the mean. When the effective albedo is considered, most farms achieve break-even instantly, implying a net cooling effect over their entire operational lifetime. In the bottom map, all farms reach break-even during their lifetime. The CBET of considering the effective albedo change resulted in an average value of 0.41 yr with a median of 0.00 yr. This shows that most farms immediately reach their carbon break even when the effective albedo is considered.

The resulting average carbon intensity of electricity, attributed solely to the change in absolute albedo, was 9.72 g/kWh (CO_2 – eq). This value provides an estimate of the climate impact arising exclusively from the change in absolute albedo. This value is in the same order magnitude as the value of 2.5 g/kWh (CO_2 – eq) found in Chapter 1. The discrepancy may stem from the different values for the albedo change found in this study compared with those reported by Wei et al. Moreover, this study and that of Wei et al. are based on different farms and methods to compute $RF_{\Delta\alpha}$. Furthermore, for the absolute albedo change, the value of $CI_{\Delta\alpha,P}$ was determined to be 397 kg/kWp (CO_2 – eq). This value is similar in magnitude to the embodied emissions of PV systems of 592 kg/kWp (CO_2 – eq) reported in the literature [22]. On the other hand, when only the variation in effective albedo was taken into account, the average total $CI_{\Delta\alpha,E}$ amounted to -14.09 g/kWh (CO_2 – eq). For this change in effective albedo, the carbon intensity per unit of installed capacity was calculated as -529 kg/kWp (CO_2 – eq). This shows that the effective albedo implies a cooling impact associated with the albedo change caused by solar farms.

The average CBET computed with the absolute albedo in this study resulted in 7.79 yr. This is considerably longer than the values reported by Wei et al. [31]. In their study, all farms achieve break-even in less than eight months as shown in Figure E.1. To verify the model used in this study, a validation run was conducted with the parameters configured to align as closely as possible with those used by Wei et al. In this validation run the model found an average CBET, considering the absolute albedo change, of 1.24 yr. Although the average CBET does not fully align with the values reported by Wei et al., it is substantially closer. The remaining difference between the validation run and the results of Wei et al. may be attributable to differences in the research methodology. The discrepancy between the results of this study and those of the validation run is considerable. In this study, an average electricity carbon intensity of 494 g/kWh (CO_2 – eq) was applied, whereas Wei et al. employed a value of 900 g/kWh (CO_2 – eq). This substantial discrepancy is proposed as the primary explanation for the large difference between this study and the validation run.

The results of the sensitivity analysis of the carbon break even time are presented in table 4.4. The η_{PV} and PR ratio influence the CBE_{eff} via the effective albedo calculation. In reality these variables would also influence the $CBET_{abs}$ through the yield calculations. However, in the model, the specific yield estimates are obtained from a dataset as a single value, without separate specifications for η_{PV} and PR. In the model, farms that only break even after their full lifetime are still treated as if they reach break even exactly at the end of their life. This is why changes in LT affect the average $CBET$. The $CBET_{eff}$ shows strong sensitivity to η_{PV}, GCR and PR. This arises because these variables directly control the offset of the $RF_{\Delta\alpha}$ through the change in effective albedo. In turn, this offset has a strong impact on the zero crossing of the net RF. Both the $CBET_{eff}$ show the least sensitivity to the degradation rate. The model applies a simplified linear approximation of the degradation. Adopting a more realistic degradation model could affect any design criteria derived from the results. Nevertheless, this impact is expected to remain small.

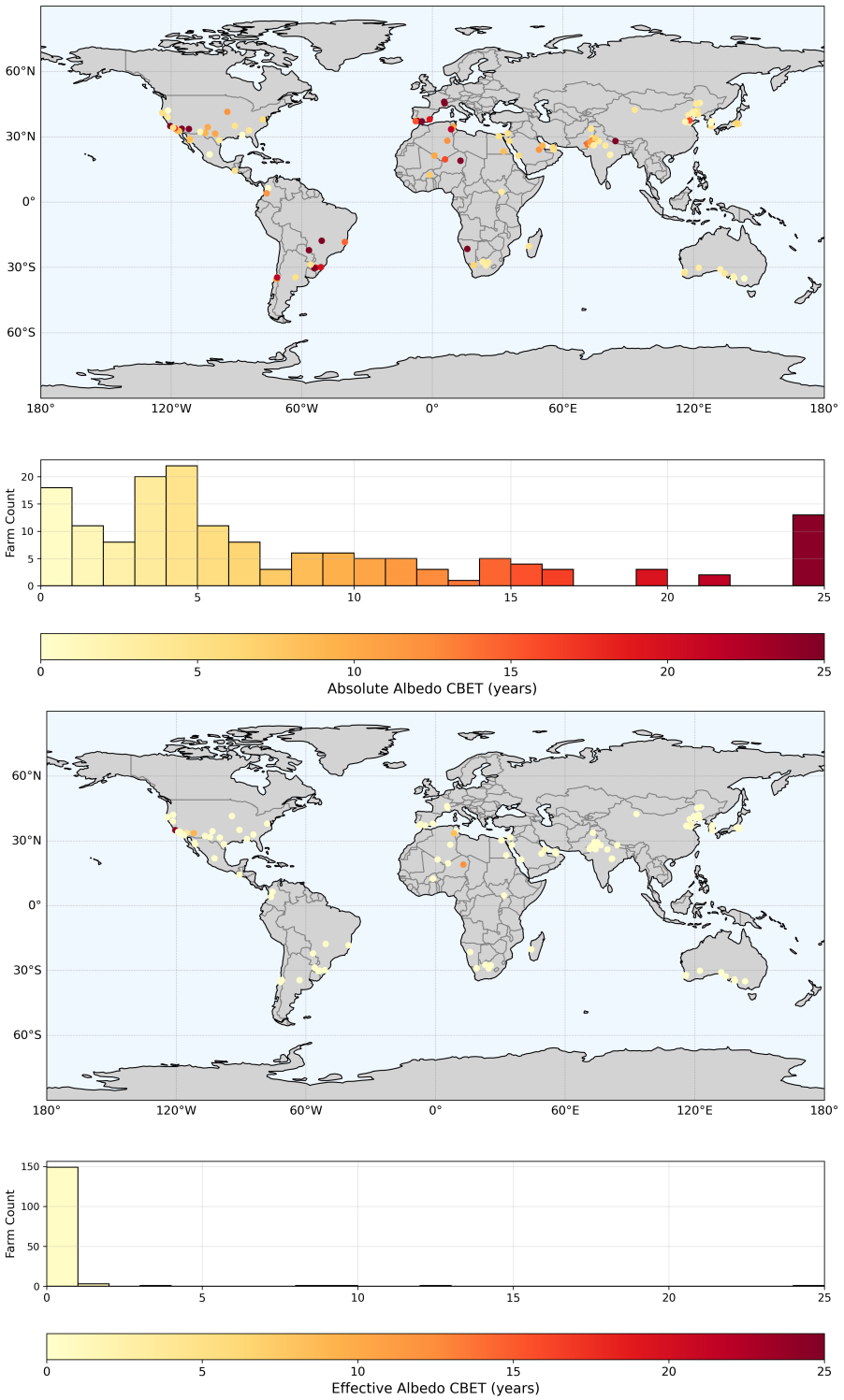

Figure 4.10: Maps showing the carbon break even time (CBET) of each solar farm. The results displayed in the top map were obtained using the absolute albedo, whereas the results in the bottom map were derived from the effective albedo. The histograms below each map show the distribution of the CBET outcomes. Farms that did not reach their CBET within their lifetime where considered as reaching their CBET at the end of their life. All maps and histograms share a colour bar scale. The average CBET considering the absolute albedo change is 7.79 yr with a median of 4.92 yr. The average CBET considering the effective albedo change is 0.41 yr with a median of 0.00 yr.

Table 4.4: Results of the sensitivity analysis of the carbon break even time (CBET) in years. The carbon break even time is given as the average over all 157 analysed farms in years. The carbon break even time considering the absolute albedo change ($CBET_{abs}$) and the carbon break even time considering the effective albedo change ($CBET_{eff}$) are analysed. The column describing the type of variable shows whether the variable is specific to each farm or a general constant that is the same for all farms. For farm specific variables, the value shown represents the average across all farms. The first row in the table represents the base scenario. The sensitivity of the following variables were analysed: the PV module efficiency (η_{PV}) in (%), the ground cover ratio (GCR), the performance ratio (PR), the degradation rate (r_d) in % per year, the PV life time (LT) in years, the CO_2 radiative kernel (k_{CO_2}) in W/m^2 kg (CO_2), the installed power estimation P_{inst} in MW, the specific yield (Y_{spec}) in kWh/kWp yr, the local carbon intensity of electricity (CI_{elec}) in g/kWh (CO_2−eq), the carbon intensity of electricity due to the embodied emissions of the solar farm (CI_{emb}) in kg/kWp (CO_2−eq), the difference between the absolute albedo of the PV region and the albedo of the surrounding region ($\Delta\alpha_{abs}$) and the difference between the effective albedo of the PV region and the albedo of the surrounding region ($\Delta\alpha_{eff}$). The percentage variation in carbon break-even time relative to the baseline, caused by changes in the variables, is presented in the $\Delta CBET_{abs}$ (%) and $\Delta CBET_{eff}$ (%) columns.

Variable	Type of variable	Base Value	Δ Variable (%)	$CBET_{abs}$	Δ $CBET_{abs}$ (%)	$CBET_{eff}$	Δ $CBET_{eff}$ (%)
-	-	-	-	7.79	-	0.41	-
η_{PV}	general	19.5	+10	7.79	-	0.31	-24.11
η_{PV}	general	19.5	-10	7.79	-	0.61	+46.12
GCR	general	0.58	+10	7.79	-	0.31	-24.11
GCR	general	0.58	-10	7.79	-	0.61	+46.12
PR	general	0.75	+10	7.79	-	0.31	-24.11
PR	general	0.75	-10	7.79	-	0.61	+46.12
r_d	general	0.5	+10	7.80	+0.18	0.42	+0.52
r_d	general	0.5	-10	7.78	-0.11	0.41	-0.64
LT	general	25	+12	8.01	+2.95	0.41	-
LT	general	25	-12	7.54	-3.17	0.40	-3.72
k_{CO_2}	general	1.65×10^{-15}	+5	7.48	-3.93	0.39	-5.38
k_{CO_2}	general	1.65×10^{-15}	-5	8.11	+4.23	0.43	+4.61
P_{inst}	specific	33	+10	7.33	-5.84	0.38	- 8.46
P_{inst}	specific	33	-10	8.33	+7.02	0.44	+7.18
Y_{spec}	specific	1649	+10	7.20	-7.54	0.37	-10.11
Y_{spec}	specific	1649	-10	8.48	+8.97	0.45	+8.97
CI_{elec}	specific	494	+10	7.20	-7.54	0.36	-10.11
CI_{elec}	specific	494	-10	8.48	+8.97	0.45	+8.97
CI_{emb}	general	592	+10	7.93	+1.86	0.42	+2.19
CI_{emb}	general	592	-10	7.63	-1.67	0.41	-1.67
$\Delta\alpha_{abs}$	specific	-0.0299	+10	8.28	+6.37	0.41	-
$\Delta\alpha_{abs}$	specific	-0.0299	-10	7.28	-6.51	0.41	-
$\Delta\alpha_{eff}$	specific	0.0496	+10	7.79	-	0.44	+5.63
$\Delta\alpha_{eff}$	specific	0.0496	-10	7.79	-	0.38	-9.09

4.6. Conclusion

In this chapter, the albedo climate effect was examined. A model was developed to estimate and evaluate the global albedo–climate impact of solar farms, taking into account both their effective albedo and the local carbon intensity of electricity generation. The embodied emissions excluding, those of the balance of system, were considered. The local monthly specific yield and the local carbon intensity of electricity were included in order to account for farm-specific climatic effects. Overall assumption were done about the farms efficiency and degradation, as all farms analysed were deployed within a two year region. The change in albedo associated with the 157 analysed solar farms was evaluated. Both the absolute albedo and the effective albedo were considered. The average absolute change in albedo was determined to be -0.0299, whereas the average effective change in albedo was 0.0496. This study identified a carbon break-even time of 7.79 yr when accounting for absolute albedo changes, with 12 farms failing to reach break-even within their lifetime. This is considerably higher than found in previous research. The largest reason found for this difference with previous work was carbon intensity of electricity considered in the avoided emissions determination. This study found that considering the effective albedo most solar farms instantly reach their carbon break even time with an average carbon break even time of 0.41 yr. The results indicate a potential cooling effect for solar farms when the effective albedo is considered.

5

Conclusion

The goal of this thesis was to determine the albedo-climate effect of solar farms globally considering the effective albedo and solar panel degradation. The research was divided into three sub-objectives. First, a model was developed to determine surface albedo. Second, another model was created to quantify the change in albedo resulting from solar farm deployment. Finally, a third model evaluated how these solar farm–driven albedo changes affect the climate.

In Chapter 2, the model was developed to derive surface albedo with the use of Sentinel-2 satellite imagery as input. This model can produce albedo estimates with a root-mean-square error (RMSE) of 0.032. A bias correction was derived as a function of the solar zenith angle at the time of Sentinel-2 image acquisition. The correction is theoretically based on the expected error that arises when assuming the surface behaves as a Lambertian reflector. With the application of the correction the albedo estimation RMSE was decreased to 0.021. The findings highlighted how the Lambertian assumption affects the derived albedo values and showed that applying a bias correction is an effective approach to enhance albedo estimation.

Chapter 3 introduced the second model designed to quantify how solar farm deployment alters surface albedo. To determine the change in albedo, the difference of the solar farm polygon albedo with the surrounding albedo was taken of 500 farms. For most farms, the albedo difference was small and negative with an average value of -0.0198. This suggests that, overall, the alteration of surface albedo caused by solar farm installation causes a warming effect. The results of the second model presented in this thesis align with previous research, but they exhibited larger albedo changes.

Thirdly, Chapter 4 developed the model to assess the climatic impact of the estimated change in albedo due to 157 of the solar farms. In this model, the degradation of the solar farms and the local carbon intensity of electricity was incorporated into the analysis. Both the absolute and effective changes in albedo due the solar farms were examined. On average an absolute albedo change of -0.0299 and effective albedo change of 0.0496 was found. This study identified an average carbon break-even time of 7.79 yr when accounting for absolute albedo changes, with 12 farms failing to reach break-even within their lifetime. This is considerably higher than found in previous research. The main explanations suggested for this discrepancy with earlier studies are, first, that the earlier work assumed a higher carbon intensity for electricity when calculating avoided emissions, and second, that it reported a smaller absolute change in albedo. This study found that, when the effective albedo is taken into account, most solar farms achieve their carbon break-even point almost immediately, with an average carbon break-even time of 0.41 yr. The analysis shows that the effective albedo implies a cooling rather than warming influence of solar farms on the climate, thereby reducing their overall climate impact.

6

Discussion & Recommendations

This chapter provides a reflection on the research conducted in this report. It addresses the methodology used, the practical limitations encountered, and potential ways to improve the project. In addition, it presents suggestions for future research. The recommendations are organized according to the various research objectives discussed in this report.

About the Determination of the Albedo

It was noticed that the Sentinel 2 masking, for example on the presence of clouds in an image, can be faulty. The presence of clouds may have caused an overestimation of albedo, whereas cloud shadows may have resulted in an underestimation of albedo. Due to the large number of processed images, visual inception for all was not an option. If just a small portion of the images are faulty, and this can be treated as random error, reviewing a larger number of images will reduce the impact of that error. To enable the analysis of a larger volume of data, the model would require further optimisation and access to greater computational power.

To decrease the required computational resources, the analysis could be carried out at a coarser resolution. If a lower spatial resolution were selected, a dataset such as Harmonized Landsat Sentinel-2 could be employed [85]. This dataset provides surface reflectance data at a spatial resolution of 30 m by 30 m, with observations every 2 to 3 days. The use of this dataset would improve the chance of to obtain sufficient high-quality observations for each farm. Conversely, a smaller resolution enables the analysis of finer spatial geometries, making it possible to include smaller farms in the study.

Further research is recommend for the bias correction in albedo estimation model. The current correction implies a linear relationship between the difference separating the true reflection profile and the Lambertian assumed profile, and the solar zenith angle. However, since the actual reflection profile is unknown, the appropriate correction is as well. A theoretical analysis of more realistic reflection profiles could lead to a different bias correction approach that would further enhance the results.

About the Albedo Change due to Solar Farms

With the method employed in this research it is not possible to analyse the albedo change when snow has fallen. This is because the albedo determination method by Bonafoni et al. employed in this work does not work on snow or ice [37]. However, solar farms constructed in regions that regularly receive snowfall, or in areas with permanent snow cover, can significantly alter the albedo, leading to a stronger warming effect. This is under the assumption that the PV panels will be kept snow free. Including these farms in the analysis would result in a more comprehensive few of the albedo climate effect of solar farm. To achieve this, the albedo determination approach needs to be broadened so that it can accurately estimate albedo under all conditions. The literature presents several glacier albedo determination methods that could be appropriate for this model extension [86].

In addition to high-resolution surface reflectance data, precise delineation of solar farms is required to obtain good albedo change estimates. With a more accurate delineation, pixels can be attributed

more accurately either to the PV area or to the surrounding region. This could diminish the currently observed seasonality in the albedo of the PV region, since misclassified pixels are suspected to be the cause for this seasonality. Improved delineation has been demonstrated in the literature, but is not yet available in global PV datasets [87]. This study highlights the importance of the development of such high-quality datasets.

Beyond the refinement of the absolute albedo values, better delineation would also improve estimates of effective albedo and energy yield. In this study, the ground cover ratio used to adjust for delineation errors was assumed to be a uniform constant for all farms. However, this ratio varies strongly from farm to farm, as could be seen in Table 4.1. Without improved delineation, outcomes could be improved with a ground cover ratio value specific to each country or to each farm.

About the Albedo Climate Effect of Solar Farms

In this model the degradation rate is assumed to be constant over space and time. However, both are no really true. In practice, the degradation typically shows an initial non-linear decline, followed by a more stable, linear phase [74]. Additionally, degradation occurs unevenly across space because it depends on local climate and weather conditions. The integration of these effects in the model could make the carbon break-even time more sensitive to degradation.

In this study, additional parameters were also treated as constants, even though in reality they vary with location, time, or with both location and time. For example, the performance ratio could be assessed at each location by estimating it from specific yield and climatological GHI data [88][75]. Also the degradation, which is highly climate dependent, was assumed to be constant. Differentiation of these parameters could improve the results and lead to meaningful design recommendations for solar farms.

As with most data analysis studies, the analysis of a larger volume of data has the potential to yield better results. Extending the carbon break even time analysis to include more than 157 farms would enhance the results, as they would be less sensitive to outliers. Collecting additional information on farm types, such as whether they are floating, rooftop, or tracking systems, could create opportunities to identify correlations between farm design and climate impact, leading to improved design recommendations.

In the model, any carbon break-even time that is longer than the 25-year lifetime is now capped at 25 years, since the analysed time series is also limited to this duration. This approach, however, may result in an underestimation of the carbon break-even time. A possible improvement would be to extrapolate the cumulative net radiative forcing beyond the modelled period in order to estimate carbon break-even times that extend past the defined lifetime.

Literature suggests that approaches for estimating equivalent CO_2 emissions from $RF_{\Delta\alpha}$ are subject to inherent limitations [83]. Bright et al. emphasize numerous difficulties in defining and interpreting CO2-equivalent metrics for albedo change, including the challenge of determining the airborne fraction [83][84]. Consequently, the carbon-equivalent values reported in this study should be interpreted with care. Additional research is recommended to develop robust methods for incorporating albedo change into the life cycle assessment of solar farms.

The life cycle analysis applied in this study does account for balance-of-system components as well as maintenance. Likewise any changes in carbon sequestration due to the land used to solar farm deployment should be taken into account [31]. These aspects need to be included to provide a comprehensive analysis of the climate impact of solar farms. Accounting for them may result in a longer carbon break even time for the solar farms.

In comparing different electricity generation methods, it is assumed that the electricity must be generated one way or the other. However, this analysis does not take into account that, in order to meet the same electricity demand, intermittent generation must produce more electricity to offset storage losses. To account for this, the avoided emissions could be reduced, implying a smaller amount of carbon-intensive generation being displaced when compared to the electricity produced by the solar farm.

References

[1] Intergovernmental Panel On Climate Change (Ipcc). *Climate Change 2022 – Impacts, Adaptation and Vulnerability: Working Group II Contribution to the Sixth Assessment Report of the Intergovernmental Panel on Climate Change*. 1st ed. Cambridge University Press, June 2023. ISBN: 978-1-009-32584-4. DOI: 10.1017/9781009325844. URL: https://www.cambridge.org/core/product/identifier/9781009325844/type/book (visited on 11/20/2025).

[2] United Nations Framework Convention on Climate Change (UNFCCC). *Paris Agreement*. English. 2015. URL: https://unfccc.int/sites/default/files/english_paris_agreement.pdf (visited on 10/29/2025).

[3] Intergovernmental Panel On Climate Change (Ipcc), ed. *Climate Change 2022 - Mitigation of Climate Change: Working Group III Contribution to the Sixth Assessment Report of the Intergovernmental Panel on Climate Change*. 1st ed. Cambridge University Press, Aug. 2023. ISBN: 978-1-009-15792-6. DOI: 10.1017/9781009157926. URL: https://www.cambridge.org/core/product/identifier/9781009157926/type/book (visited on 11/20/2025).

[4] Marc Perez and Richard Perez. "Update 2022 – A fundamental look at supply side energy reserves for the planet". en. In: *Solar Energy Advances* 2 (2022), p. 100014. ISSN: 26671131. DOI: 10.1016/j.seja.2022.100014. URL: https://linkinghub.elsevier.com/retrieve/pii/S266711312200002X (visited on 11/20/2025).

[5] Arno Smets. *Solar Energy: The Physics and Engineering of Photovoltaic Conversion, Technologies and Systems*. eng. London: Bloomsbury Publishing Plc, 2016. ISBN: 978-1-906860-32-5.

[6] Mladen Bošnjaković et al. "Environmental Impact of PV Power Systems". en. In: *Sustainability* 15.15 (Aug. 2023), p. 11888. ISSN: 2071-1050. DOI: 10.3390/su151511888. URL: https://www.mdpi.com/2071-1050/15/15/11888 (visited on 10/31/2025).

[7] S. Schlömer. "Annex III: Technology-specific cost and performance parameters". In: *Climate change 2014: mitigation of climate change: Working Group III contribution to the Fifth Assessment Report of the Intergovernmental Panel on Climate Change*. Ed. by Intergovernmental Panel on Climate Change and O. Edenhofer. New York, NY: Cambridge University Press, 2014, pp. 1329–1356. ISBN: 978-1-107-05821-7.

[8] T. Gibon, Á. H. Menacho, and M. Guiton. *Life Cycle Assessment of Electricity Generation Options*. Tech. rep. Geneva: United Nations Economic Commission for Europe, 2021. URL: https://unece.org/sites/default/files/2021-09/202109_UNECE_LCA_1.2_clean.pdf.

[9] Julian Prime et al. *Renewable Capacity Statistic 2024*. Tech. rep. Abu Dhabi: International Renewable Energy Agency, 2024. URL: https://www.irena.org/publications/2024/Apr/Renewable-Capacity-Statistics-2024 (visited on 06/12/2025).

[10] Gaëtan Masson et al. *Snapshot of Global PV Markets: 2024*. Tech. rep. IEA PVPS, 2024. URL: https://iea-pvps.org/wp-content/uploads/2024/04/Snapshot-of-Global-PV-Markets_20241.pdf (visited on 12/06/2025).

[11] Michael Schmela et al. *Global Market Outlook for Solar Power 2025–2029*. Tech. rep. SolarPower Europe, May 2025. URL: https://www.solarpowereurope.org/insights/global-market-outlook-2025 (visited on 06/12/2025).

[12] Anthony F. Mills. *Basic heat and mass transfer*. eng. Third edition. OCLC: 954592884. San Diego, California: Prentice Hall, 2015. ISBN: 978-0-9963053-0-3.

[13] Mariana Sendova and Isaac Moncada-Almendarez. "Mathematical forms of Planck's thermal radiation law and photobiological biomass adaptations". en. In: *Academia Biology* 3.1 (Jan. 2025). ISSN: 2837-4010. DOI: 10.20935/AcadBiol7513. URL: https://www.academia.edu/127386940/Mathematical_forms_of_Planck_s_thermal_radiation_law_and_photobiological_biomass_adaptations (visited on 12/02/2025).

[14] Edmond A. Mathez and Jason E. Smerdon. *Climate change: the science of global warming and our energy future*. eng. Second edition. New York: Columbia University Press, 2018. ISBN: 978-0-231-17283-7.

[15] Intergovernmental Panel On Climate Change (IPCC), V. Masson-Delmotte, and P. Zhai. "The Earth's Energy Budget, Climate Feedbacks and Climate Sensitivity". en. In: *Climate Change 2021 – The Physical Science Basis: Working Group I Contribution to the Sixth Assessment Report of the Intergovernmental Panel on Climate Change*. IPCC Sixth Assessment Report. Cambridge University Press, July 2023. ISBN: 978-1-009-15789-6. DOI: 10.1017/9781009157896. URL: https://www.cambridge.org/core/product/identifier/9781009157896/type/book (visited on 04/23/2025).

[16] Intergovernmental Panel On Climate Change (Ipcc). *Climate Change 2021 – The Physical Science Basis: Working Group I Contribution to the Sixth Assessment Report of the Intergovernmental Panel on Climate Change*. 1st ed. Cambridge University Press, July 2023. ISBN: 978-1-009-15789-6. DOI: 10.1017/9781009157896. URL: https://www.cambridge.org/core/product/identifier/9781009157896/type/book (visited on 01/08/2026).

[17] Max Planck. *The Theory of Heat Radiation*. Trans. by Morton Masius. second edition. 1914. URL: https://www.yaaka.cc/wp-content/uploads/2018/02/the-theory-of-heat-radiation.pdf.

[18] G03 Committee and American Society for Testing and Materials. *Tables for Reference Solar Spectral Irradiances: Direct Normal and Hemispherical on 37 Tilted Surface*. en. 2003. DOI: 10.1520/G0173-23. URL: http://www.astm.org/cgi-bin/resolver.cgi?G173-23 (visited on 11/28/2025).

[19] Kevin S. Anderson et al. "pvlib python: 2023 project update". In: *Journal of Open Source Software* 8.92 (Dec. 2023), p. 5994. ISSN: 2475-9066. DOI: 10.21105/joss.05994. URL: https://joss.theoj.org/papers/10.21105/joss.05994 (visited on 11/28/2025).

[20] Osbel Almora et al. "Device Performance of Emerging Photovoltaic Materials (Version 1)". en. In: *Advanced Energy Materials* 11.11 (Mar. 2021), p. 2002774. ISSN: 1614-6832, 1614-6840. DOI: 10.1002/aenm.202002774. URL: https://advanced.onlinelibrary.wiley.com/doi/10.1002/aenm.202002774 (visited on 11/28/2025).

[21] A. Danelli et al. *Environmental Life Cycle Assessment of Passivated Emitter and Rear Contact (PERC) Photovoltaic Module Technology*. en. Tech. rep. IEA Photovoltaic Power Systems Programme (PVPS), 2024. DOI: 10.69766/EEMP5995. URL: https://iea-pvps.org/key-topics/environmental-life-cycle-assessment-of-passivated-emitter-and-rear-contact-perc-photovoltaic-module-technology/ (visited on 11/06/2025).

[22] Amelie Müller et al. "A comparative life cycle assessment of silicon PV modules: Impact of module design, manufacturing location and inventory". en. In: *Solar Energy Materials and Solar Cells* 230 (Sept. 2021), p. 111277. ISSN: 09270248. DOI: 10.1016/j.solmat.2021.111277. URL: https://linkinghub.elsevier.com/retrieve/pii/S0927024821003202 (visited on 11/06/2025).

[23] Brittany Smith et al. *An Updated Life Cycle Assessment of Utility-Scale Solar Photovoltaic Systems Installed in the United States*. en. Tech. rep. NREL/TP–7A40-87372, 2331420, MainId:88147. Mar. 2024, NREL/TP–7A40–87372, 2331420, MainId:88147. DOI: 10.2172/2331420. URL: https://www.osti.gov/servlets/purl/2331420/ (visited on 11/06/2025).

[24] Georg Wohlfahrt, Enrico Tomelleri, and Albin Hammerle. "The albedo–climate penalty of hydropower reservoirs". en. In: *Nature Energy* 6.4 (Feb. 2021), pp. 372–377. ISSN: 2058-7546. DOI: 10.1038/s41560-021-00784-y. URL: https://www.nature.com/articles/s41560-021-00784-y (visited on 04/15/2025).

[25] Zhengjie Xu et al. "A global assessment of the effects of solar farms on albedo, vegetation, and land surface temperature using remote sensing". en. In: *Solar Energy* 268 (Jan. 2024), p. 112198. ISSN: 0038092X. DOI: 10.1016/j.solener.2023.112198. URL: https://linkinghub.elsevier.com/retrieve/pii/S0038092X23008320 (visited on 04/29/2025).

[26] Haider Taha. “The potential for air-temperature impact from large-scale deployment of solar photovoltaic arrays in urban areas”. en. In: *Solar Energy* 91 (May 2013), pp. 358–367. ISSN: 0038092X. DOI: 10.1016/j.solener.2012.09.014. URL: https://linkinghub.elsevier.com/retrieve/pii/S0038092X12003386 (visited on 11/07/2025).

[27] G. Myhre et al. “Anthropogenic and Natural Radiative Forcing”. In: *Climate Change 2013: The Physical Science Basis*. IPCC Fifth Assessment Report. Cambridge, United Kingdom and New York, NY, USA: Cambridge University Press, 2013, pp. 659–740. ISBN: 978-1-107-66182-0. URL: https://www.ipcc.ch/site/assets/uploads/2018/02/WG1AR5_Chapter08_FINAL.pdf (visited on 04/23/2025).

[28] Ryan M. Bright and Thomas L. O’Halloran. “Developing a monthly radiative kernel for surface albedo change from satellite climatologies of Earth’s shortwave radiation budget: CACK v1.0”. en. In: *Geoscientific Model Development* 12.9 (Sept. 2019), pp. 3975–3990. ISSN: 1991-9603. DOI: 10.5194/gmd-12-3975-2019. URL: https://gmd.copernicus.org/articles/12/3975/2019/ (visited on 01/09/2026).

[29] Ryan M. Bright et al. “Carbon-equivalent metrics for albedo changes in land management contexts: relevance of the time dimension”. en. In: *Ecological Applications* 26.6 (Sept. 2016), pp. 1868–1880. ISSN: 1051-0761, 1939-5582. DOI: 10.1890/15-1597.1. URL: https://esajournals.onlinelibrary.wiley.com/doi/10.1890/15-1597.1 (visited on 11/05/2025).

[30] F. Joos et al. “Carbon dioxide and climate impulse response functions for the computation of greenhouse gas metrics: a multi-model analysis”. en. In: *Atmospheric Chemistry and Physics* 13.5 (Mar. 2013), pp. 2793–2825. ISSN: 1680-7324. DOI: 10.5194/acp-13-2793-2013. URL: https://acp.copernicus.org/articles/13/2793/2013/ (visited on 11/05/2025).

[31] Sihuan Wei et al. “Small reduction in land surface albedo due to solar panel expansion worldwide”. en. In: *Communications Earth & Environment* 5.1 (Aug. 2024), p. 474. ISSN: 2662-4435. DOI: 10.1038/s43247-024-01619-w. URL: https://www.nature.com/articles/s43247-024-01619-w (visited on 04/23/2025).

[32] M. Stucki et al. “Environmental Life Cycle Assessment of Electricity from PV systems – 2023 data update”. en. In: *IEA* (May 2024). URL: https://iea-pvps.org/wp-content/uploads/2024/05/Slides_IEA-PVPS-T12_Fact-Sheet-update-2023_v2.0.pdf.

[33] Xingwen Lin et al. “Estimating 10-m land surface albedo from Sentinel-2 satellite observations using a direct estimation approach with Google Earth Engine”. en. In: *ISPRS Journal of Photogrammetry and Remote Sensing* 194 (Dec. 2022), pp. 1–20. ISSN: 09242716. DOI: 10.1016/j.isprsjprs.2022.09.016. URL: https://linkinghub.elsevier.com/retrieve/pii/S092427162200260X (visited on 08/13/2025).

[34] Shunlin Liang. “Narrowband to broadband conversions of land surface albedo I Algorithms”. en. In: (May 2001). DOI: https://doi.org/10.1016/S0034-4257(00)00205-4. URL: https://www.sciencedirect.com/science/article/pii/S0034425700002054.

[35] Masahiro Tasumi, Richard G. Allen, and Ricardo Trezza. “At-Surface Reflectance and Albedo from Satellite for Operational Calculation of Land Surface Energy Balance”. en. In: *Journal of Hydrologic Engineering* 13.2 (Feb. 2008), pp. 51–63. ISSN: 1084-0699, 1943-5584. DOI: 10.1061/(ASCE)1084-0699(2008)13:2(51). URL: https://ascelibrary.org/doi/10.1061/%28ASCE%291084-0699%282008%2913%3A2%2851%29 (visited on 09/02/2025).

[36] Zhan Li et al. “Preliminary assessment of 20-m surface albedo retrievals from sentinel-2A surface reflectance and MODIS/VIIRS surface anisotropy measures”. en. In: *Remote Sensing of Environment* 217 (Nov. 2018), pp. 352–365. ISSN: 00344257. DOI: 10.1016/j.rse.2018.08.025. URL: https://linkinghub.elsevier.com/retrieve/pii/S0034425718304024 (visited on 12/24/2025).

[37] Stefania Bonafoni and Aliihsan Sekertekin. “Albedo Retrieval From Sentinel-2 by New Narrow-to-Broadband Conversion Coefficients”. en. In: *IEEE Geoscience and Remote Sensing Letters* 17.9 (Sept. 2020), pp. 1618–1622. ISSN: 1545-598X, 1558-0571. DOI: 10.1109/LGRS.2020.2967085. URL: https://ieeexplore.ieee.org/document/8974188/ (visited on 08/19/2025).

[38] Giorgio Baldinelli, Stefania Bonafoni, and Antonella Rotili. “Albedo Retrieval From Multispectral Landsat 8 Observation in Urban Environment: Algorithm Validation by in situ Measurements”. en. In: *IEEE Journal of Selected Topics in Applied Earth Observations and Remote Sensing* 10.10 (Oct. 2017), pp. 4504–4511. ISSN: 1939-1404, 2151-1535. DOI: 10.1109/JSTARS.2017.2721549. URL: https://ieeexplore.ieee.org/document/7976307/ (visited on 09/02/2025).

[39] Yilong Zhou et al. “Assessing the dual radiative consequences of urban PV integration: Albedo change and radiative forcing dynamics”. en. In: *Applied Energy* 401 (Dec. 2025), p. 126544. ISSN: 03062619. DOI: 10.1016/j.apenergy.2025.126544. URL: https://linkinghub.elsevier.com/retrieve/pii/S0306261925012747 (visited on 12/09/2025).

[40] Xunhe Zhang and Ming Xu. “Assessing the Effects of Photovoltaic Powerplants on Surface Temperature Using Remote Sensing Techniques”. en. In: *Remote Sensing* 12.11 (June 2020), p. 1825. ISSN: 2072-4292. DOI: 10.3390/rs12111825. URL: https://www.mdpi.com/2072-4292/12/11/1825 (visited on 01/10/2026).

[41] Philip Wolfe. *Utility-scale Solar Installations Worldwide*. English. July 2025. URL: https://wiki-solar.org/map/world.html.

[42] L. Kruitwagen et al. “A global inventory of photovoltaic solar energy generating units”. en. In: *Nature* 598.7882 (Oct. 2021), pp. 604–610. ISSN: 0028-0836, 1476-4687. DOI: 10.1038/s41586-021-03957-7. URL: https://www.nature.com/articles/s41586-021-03957-7 (visited on 04/15/2025).

[43] Copernicus Sentinel Data Hub. *Sentinel 2 Mission*. URL: https://sentiwiki.copernicus.eu/web/s2-mission (visited on 12/09/2025).

[44] *Harmonized Sentinal-2 MSI: Multi Spectral Insstrument, Level-2A (SR)*. Catalog. URL: https://developers.google.com/earth-engine/datasets/catalog/COPERNICUS_S2_SR_HARMONIZED (visited on 11/13/2025).

[45] Sentinel Hub. *Sentinel-2 L2A*. URL: https://docs.sentinel-hub.com/api/latest/data/sentinel-2-l2a/#about-sentinel-2-l2a-data (visited on 11/13/2025).

[46] Kevin Hamilton and Takatoshi Sakazaki. “A note on apparent solar time and the seasonal cycle of atmospheric solar tides”. en. In: *Quarterly Journal of the Royal Meteorological Society* 143.706 (July 2017), pp. 2310–2314. ISSN: 0035-9009, 1477-870X. DOI: 10.1002/qj.3076. URL: https://rmets.onlinelibrary.wiley.com/doi/10.1002/qj.3076 (visited on 12/17/2025).

[47] ESA. *Sun-synchronous orbit*. ESA. URL: https://www.esa.int/ESA_Multimedia/Images/2020/03/Polar_and_Sun-synchronous_orbit (visited on 12/16/2025).

[48] Copernicus Sentinel Data Hub. *Sentinel 2 Products*. URL: https://sentiwiki.copernicus.eu/web/s2-products (visited on 10/08/2025).

[49] R. Richter, J. Louis, and U. Müller-Wilm. *Sentinel-2 MSI – Level 2A Products Algorithm Theoretical Basis Document*. English. Sept. 2012. (Visited on 12/17/2025).

[50] Jerome Louis et al. “Sentinel-2 Global Surface Reflectance Level-2a Product Generated with Sen2Cor”. en. In: *IGARSS 2019 - 2019 IEEE International Geoscience and Remote Sensing Symposium*. Yokohama, Japan: IEEE, July 2019, pp. 8522–8525. ISBN: 978-1-5386-9154-0. DOI: 10.1109/IGARSS.2019.8898540. URL: https://ieeexplore.ieee.org/document/8898540/ (visited on 12/17/2025).

[51] *Sentinel 2 - MSI - Level 2A Products*. English. Product description. URL: https://s2.pages.eopf.copernicus.eu/msi/s2msi/main/PDFS_ADFS/L2/PDFS_S2_MSI_L2.html (visited on 12/18/0205).

[52] Noel Gorelick et al. “Google Earth Engine: Planetary-scale geospatial analysis for everyone”. en. In: *Remote Sensing of Environment* 202 (Dec. 2017), pp. 18–27. ISSN: 00344257. DOI: 10.1016/j.rse.2017.06.031. URL: https://linkinghub.elsevier.com/retrieve/pii/S0034425717302900 (visited on 11/28/2025).

[53] Carlo Barletta, Alessandra Capolupo, and Eufemia Tarantino. “Extracting Land Surface Albedo from Landsat 9 Data in GEE Platform to Support Climate Change Analysis”. en. In: *Geomatics and Environmental Engineering* 17.6 (Oct. 2023), pp. 35–75. ISSN: 2300-7095, 1898-1135. DOI: 10.7494/geom.2023.17.6.35. URL: https://www.gaee.agh.edu.pl/gaee/article/view/538 (visited on 05/13/2025).

[54] Nathaniel J. Field and Joseph A. A. Shaw. “Lambertian surfaces with over- and under-filled field of view”. In: *Optics Education and Outreach VII*. Ed. by G. Groot Gregory and Anne-Sophie Poulin-Girard. San Diego, United States: SPIE, Oct. 2022, p. 12. ISBN: 978-1-5106-5410-5. DOI: 10.1117/12.2633738. URL: https://www.spiedigitallibrary.org/conference-proceedings-of-spie/12213/2633738/Lambertian-surfaces-with-over--and-under-filled-field-of/10.1117/12.2633738.full (visited on 12/29/2025).

[55] C. H. Liu, A. J. Chen, and G. R. Liu. “Variability of the bare soil albedo due to different solar zenith angles and atmospheric haziness”. en. In: *International Journal of Remote Sensing* 15.13 (Sept. 1994), pp. 2531–2542. ISSN: 0143-1161, 1366-5901. DOI: 10.1080/01431169408954264. URL: https://www.tandfonline.com/doi/full/10.1080/01431169408954264 (visited on 12/29/2025).

[56] Alain Fournier. “Separating Reflection Functions for Linear Radiosity”. en. In: *Rendering Techniques ’95*. Ed. by Patrick M. Hanrahan and Werner Purgathofer. Series Title: Eurographics. Vienna: Springer Vienna, 1995, pp. 296–305. ISBN: 978-3-211-82733-8. DOI: 10.1007/978-3-7091-9430-0_28. URL: http://link.springer.com/10.1007/978-3-7091-9430-0_28 (visited on 01/19/2026).

[57] M. Ben Yaala et al. “Bidirectional reflectance measurement of tungsten samples to assess reflection model in WEST tokamak”. en. In: *Review of Scientific Instruments* 92.9 (Sept. 2021), p. 093501. ISSN: 0034-6748, 1089-7623. DOI: 10.1063/5.0046140. URL: https://pubs.aip.org/rsi/article/92/9/093501/1030719/Bidirectional-reflectance-measurement-of-tungsten (visited on 01/11/2026).

[58] M. E. Thomas et al. “A general BRDF/BSDF model including out-of-plane dependence”. In: ed. by Zu-Han Gu and Leonard M. Hanssen. San Diego, California, United States, Aug. 2010, p. 77920I. DOI: 10.1117/12.861046. URL: http://proceedings.spiedigitallibrary.org/proceeding.aspx?doi=10.1117/12.861046 (visited on 01/11/2026).

[59] Xuanlong Ma et al. “Sun-Angle Effects on Remote-Sensing Phenology Observed and Modelled Using Himawari-8”. en. In: *Remote Sensing* 12.8 (Apr. 2020), p. 1339. ISSN: 2072-4292. DOI: 10.3390/rs12081339. URL: https://www.mdpi.com/2072-4292/12/8/1339 (visited on 12/29/2025).

[60] Stefania Bonafoni. *Email correspondence with S.Bonafoni*. English. Oct. 2025.

[61] National Oceanic and Atmospheric Administration (NOAA). *SURFRAD—Surface Radiation Budget Network*. Tech. rep. U.S.: NOAA Global Monitoring Laboratory. URL: https://gml.noaa.gov/grad/surfrad/index.html (visited on 12/30/2025).

[62] Mark Friedl and Damien Sulla-Menashe. *MODIS/Terra+Aqua Land Cover Type Yearly L3 Global 500m SIN Grid V061*. 2022. DOI: 10.5067/MODIS/MCD12Q1.061. URL: https://www.earthdata.nasa.gov/data/catalog/lpcloud-mcd12q1-061 (visited on 02/27/2026).

[63] D.S. Kimes and P.J. Sellers. “Inferring hemispherical reflectance of the earth’s surface for global energy budgets from remotely sensed nadir or directional radiance values”. en. In: *Remote Sensing of Environment* 18.3 (Dec. 1985), pp. 205–223. ISSN: 00344257. DOI: 10.1016/0034-4257(85)90058-6. URL: https://linkinghub.elsevier.com/retrieve/pii/0034425785900586 (visited on 01/05/2026).

[64] Caleb Robinson et al. *Global Renewables Watch: A Temporal Dataset of Solar and Wind Energy Derived from Satellite Imagery*. en. arXiv:2503.14860 [cs]. Mar. 2025. DOI: 10.48550/arXiv.2503.14860. URL: http://arxiv.org/abs/2503.14860 (visited on 07/31/2025).

[65] TransitionZero. *Solar Asset Mapper TransitionZero*. May 2025. URL: https://www.transitionzero.org/products/solar-asset-mapper (visited on 07/29/2025).

[66] Joris Van den Bossche et al. *geopandas/geopandas: v1.1.1*. June 2025. DOI: 10.5281/ZENODO.15750510. URL: https://zenodo.org/doi/10.5281/zenodo.15750510 (visited on 01/13/2026).

[67] Jeff Whitaker. *pyproj*. 2024. URL: https://pypi.org/project/pyproj/.

[68] Christian Theune. *pycountry*. 2024. URL: https://pypi.org/project/pycountry/.

[69] International Organization for Standardization. *Codes for the representation of names of countries and their subdivisions — Part 1: Country codes*. Tech. rep. ISO 3166-1. Geneva, Switzerland: International Organization for Standardization, 2020. URL: https://www.iso.org/iso-3166-country-codes.html.

[70] VDMA Photovoltaics Equipment. *International Technology Roadmap for Photovoltaics (ITRPV): Results 2024*. Tech. rep. 16. Frankfurt am Main, Germany: VDMA Photovoltaics Equipment, 2024. URL: https://www.vdma.eu/en-GB/international-technology-roadmap-photovoltaic.

[71] K. P. Sreejith et al. "Comprehensive Glare Hazard Analysis of Ethylene Tetrafluoroethylene (ETFE) Based Frontsheet for Flexible Photovoltaic Applications". en. In: *IEEE Journal of Photovoltaics* 14.6 (Nov. 2024), pp. 930–936. ISSN: 2156-3381, 2156-3403. DOI: 10.1109/JPHOTOV.2024.3463961. URL: https://ieeexplore.ieee.org/document/10717448/ (visited on 12/29/2025).

[72] K.L. Seow et al. "Spectral BRDF of common urban materials". In: *2012 4th Workshop on Hyperspectral Image and Signal Processing (WHISPERS)*. Shanghai, China: IEEE, June 2012, pp. 1–4. ISBN: 978-1-4799-3406-5. DOI: 10.1109/WHISPERS.2012.6874250. URL: https://ieeexplore.ieee.org/document/6874250 (visited on 01/17/2026).

[73] Martin A. Green et al. "Solar cell efficiency tables (Version 60)". en. In: *Progress in Photovoltaics: Research and Applications* 30.7 (July 2022), pp. 687–701. ISSN: 1062-7995, 1099-159X. DOI: 10.1002/pip.3595. URL: https://onlinelibrary.wiley.com/doi/10.1002/pip.3595 (visited on 02/19/2026).

[74] Dirk C. Jordan et al. "Compendium of photovoltaic degradation rates". en. In: *Progress in Photovoltaics: Research and Applications* 24.7 (July 2016), pp. 978–989. ISSN: 1062-7995, 1099-159X. DOI: 10.1002/pip.2744. URL: https://onlinelibrary.wiley.com/doi/10.1002/pip.2744 (visited on 01/27/2026).

[75] Cem Haydaroğlu, Heybet Kılıç, and Bilal Gümüş. "Performance Analysis and Comparison of Performance Ratio of Solar Power Plant". en. In: *Turkish Journal of Electrical Power and Energy Systems* 4.3 (Sept. 2024), pp. 190–199. ISSN: 2791-6049. DOI: 10.5152/tepes.2024.24009. URL: https://tepesjournal.org/index.php/pub/article/view/74 (visited on 02/16/2026).

[76] Ankit Rohatgi. *WebPlotDigitizer*. Jan. 2026. URL: https://wpd.starrydata2.org.

[77] Han Huang. *Data for ERA5 radiative kernels*. June 2023. DOI: 10.17632/VMG3S67568.4. URL: https://data.mendeley.com/datasets/vmg3s67568/4 (visited on 01/20/2026).

[78] Han Huang and Yi Huang. "Radiative sensitivity quantified by a new set of radiation flux kernels based on the ECMWF Reanalysis v5 (ERA5)". en. In: *Earth System Science Data* 15.7 (July 2023), pp. 3001–3021. ISSN: 1866-3516. DOI: 10.5194/essd-15-3001-2023. URL: https://essd.copernicus.org/articles/15/3001/2023/ (visited on 01/20/2026).

[79] Britannica Editors. *How Big Is Earth?* July 2025. URL: https://www.britannica.com/science/How-Big-Is-Earth (visited on 02/21/2026).

[80] Aurich Jeltsch-Thömmes et al. "The influence of varying atmospheric CO_2 on global warming potentials and carbon emission impulse response functions". In: *Environmental Research Letters* 20.6 (June 2025), p. 064032. ISSN: 1748-9326. DOI: 10.1088/1748-9326/add54b. URL: https://iopscience.iop.org/article/10.1088/1748-9326/add54b (visited on 01/20/2026).

[81] Samapriya Roy. *Global Solar Atlas – GEE Community Catalog*. Oct. 2021. URL: https://gee-community-catalog.org/projects/gsa/ (visited on 02/14/2026).

[82] Hannah Ritchie, Pablo Rosando, and Max Roser. *Lifecycle carbon intensity of electricity generation*. Energy. 2023. URL: https://ourworldindata.org/grapher/carbon-intensity-electricity (visited on 02/20/2026).

[83] Ryan M. Bright and Marianne T. Lund. "CO_2 -equivalence metrics for surface albedo change based on the radiative forcing concept: a critical review". en. In: *Atmospheric Chemistry and Physics* 21.12 (July 2021), pp. 9887–9907. ISSN: 1680-7324. DOI: 10.5194/acp-21-9887-2021. URL: https://acp.copernicus.org/articles/21/9887/2021/ (visited on 02/20/2026).

[84] T. M. Lenton and N. E. Vaughan. "The radiative forcing potential of different climate geoengineering options". en. In: *Atmospheric Chemistry and Physics* 9.15 (Aug. 2009), pp. 5539–5561. ISSN: 1680-7324. DOI: 10.5194/acp-9-5539-2009. URL: https://acp.copernicus.org/articles/9/5539/2009/ (visited on 02/21/2026).

[85] Belen Franch et al. "A Method for Landsat and Sentinel 2 (HLS) BRDF Normalization". en. In: *Remote Sensing* 11.6 (Mar. 2019), p. 632. ISSN: 2072-4292. DOI: 10.3390/rs11060632. URL: https://www.mdpi.com/2072-4292/11/6/632 (visited on 12/29/2025).

[86] Kathrin Naegeli et al. "Cross-Comparison of Albedo Products for Glacier Surfaces Derived from Airborne and Satellite (Sentinel-2 and Landsat 8) Optical Data". en. In: *Remote Sensing* 9.2 (Jan. 2017), p. 110. ISSN: 2072-4292. DOI: 10.3390/rs9020110. URL: https://www.mdpi.com/2072-4292/9/2/110 (visited on 05/20/2025).

[87] Siyuan Hu et al. "Quantifying land-use metrics for solar photovoltaic projects in the western United States". en. In: *Communications Earth & Environment* 6.1 (Dec. 2025), p. 1006. ISSN: 2662-4435. DOI: 10.1038/s43247-025-02862-5. URL: https://www.nature.com/articles/s43247-025-02862-5 (visited on 02/26/2026).

[88] Manjunath Basappa Ayanna et al. "Effect of Using Global Horizontal or Plane of Array Irradiance for Monitoring Sun Tracking Solar Photovoltaic Plants Performance". en. In: (2018). URL: https://researchspace.csir.co.za/server/api/core/bitstreams/1afca60d-c55e-4cab-8e46-2e26d6b30b92/content.

[89] Crystal Schaaf and Zhuosen Wang. *MCD43A1 MODIS/Terra+Aqua BRDF/Albedo Model Parameters Daily L3 Global - 500m V006*. 2015. DOI: 10.5067/MODIS/MCD43A1.006. URL: https://lpdaac.usgs.gov/products/mcd43a1v006/ (visited on 04/30/2025).

[90] U.S. Geological Survey (USGS). *Landsat 7*. URL: https://www.usgs.gov/landsat-missions/landsat-7 (visited on 11/14/2025).

[91] U.S. Geological Survey (USGS). *Landsat 8*. URL: https://www.usgs.gov/landsat-missions/landsat-8 (visited on 11/14/2025).

[92] Google Earth Engine Team. *Resampling*. URL: https://developers.google.com/earth-engine/guides/resample (visited on 01/03/2026).

[93] C.M.G. Lee. *Comparison of 1D and 2D interpolation*. 2020. URL: https://en.wikipedia.org/wiki/Bicubic_interpolation#/media/File:Comparison_of_1D_and_2D_interpolation.svg (visited on 01/03/2026).

[94] Mason Phillpott et al. *Solar Asset Mapper: A continuously-updated global inventory of solar energy facilities built with satellite data and machine learning*. en. Tech. rep. Transition Zero, 2024. URL: https://blog.transitionzero.org/hubfs/Data%20Products/TZ-SAM/tz-sam-scientific-methodology-Q12024.pdf.

A

Scale of the Albedo-Climate Effect

The albedo change due to solar farm deployment of 0.0128 is equivalent to 2.77 Tg (C−eq) carbon emissions according to Wei et al. [31]. These emissions are attributed to 352 PV farms, representing approximately 24% of the total PV area detected in the 2018 dataset by Kruitwagen [31] which Wei et al. used in their analysis. It is assumed that the fraction of installed area corresponds to the fraction of installed capacity.

The total detected installed PV capacity in 2018 is

$$C_{\text{tot}} = 423\,\text{GW}. \tag{A.1}$$

The capacity associated with the 352 PV farms is therefore

$$C_{\text{PV}} = 0.24 \times C_{\text{tot}} = 0.24 \times 423\,\text{GW} = 101.5\,\text{GW}. \tag{A.2}$$

Dividing the carbon equivalent emissions by the associated installed capacity yields the carbon footprint per installed capacity:

$$\frac{2.77 \times 10^{12}\,\text{g}}{1.015 \times 10^{11}\,\text{W}} \approx 27\,\text{kg/kW (C−eq)} \tag{A.3}$$

This is equal to CO_2−eq emissions per installed capacity of:

$$101\,\text{kg/kW (CO}_2\text{−eq)} \tag{A.4}$$

Assuming a PV lifetime of 25 years and an average energy yield of 1600 kWh/(kWp · yr) [21], the lifetime electricity generation per unit of installed capacity is:

$$E_{\text{life}} = 25 \times 1600\,\text{kWh/kWp} = 40\,000\,\text{kWh/kWp}. \tag{A.5}$$

Dividing the CO_2−eq emissions per installed capacity due to albedo change by E_{life} results in the carbon intensity due to albedo change is therefore:

$$CI_{\Delta\alpha} = \frac{101\,\text{kg/kWp}}{40\,000\,\text{kWh/kWp}} \approx 2.5\,\text{g/kWh (CO}_2\text{−eq)} \tag{A.6}$$

For comparison, a life cycle assessment by Müller reports a carbon intensity for PV electricity generation, accounting for the production of PV panels [22], of approximately:

$$CI_{\text{LCA}} \approx 22\,\text{g/kWh (CO}_2\text{−eq)} \tag{A.7}$$

The climatic effect of albedo change is therefore on the order of 10% of that associated with PV module production.

B

Satellite data

Satellite Product Comparison

Table B.1: Satellite products considered for this research. Compared on product type, temporal coverage and resolution and on, spatial coverage and resolution.

Name	MODIS [89]	Landsat 7 [90]	Landsat 8 [91]	Sentinel 2 [48][44][45]
Product name	MCD43A1 & MCD43A3	SR Collection 2 Level-2	SR Collection 2 Level-2	Level-2A SR
Type of product	A1: BRDF parameters and A3: calculated albedo	Surface Reflectance	Surface Reflectance	Surface Reflectance
Temporal coverage	Since 2000	From 1999 till 2024	Since 2013	Since December 13th 2018 global coverage
Temporal resolution	Daily, based on 16 days	16 days	16 days	5 days
Spatial coverage	Global	Global	Global	Land and coastal areas between latitudes 56°S and 83°N
Spatial resolution	500m	30m	30m	10m for B2, B3, B4, B8 20m for B11, B12
Comment	Terra and Aqua satellite	The spatial resolutions vary across bands, 30m for most bands and in the visible spectrum.	The spatial resolutions vary across bands, 30m for most bands and in the visible spectrum.	The spectral resolution is only mentioned for bands that are used. Two satellites are used.

Sentinel-2 additional information

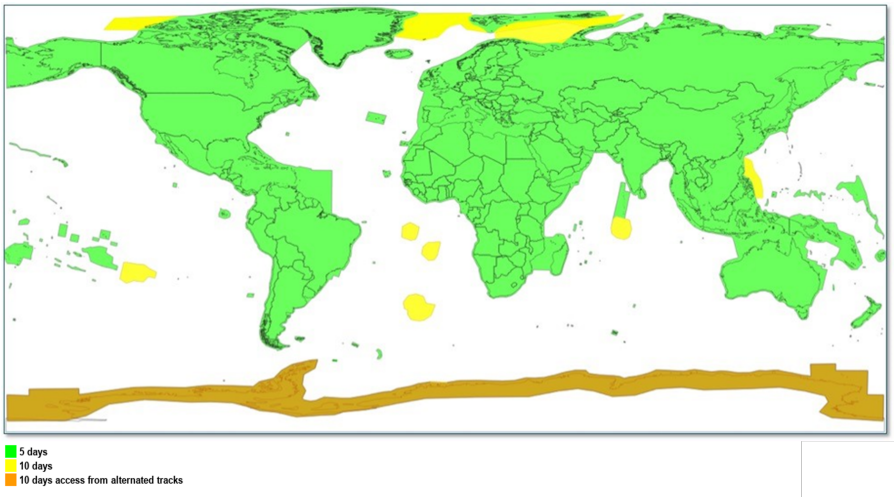

Figure B.1: Map showing the areas of the Earth's surface observed by the Sentinel-2 satellites [43], along with their revisit frequency.

Table B.2: The available surface reflectance bands in the Sentinel-2 Level-2A products are summarised [43]. Note that the wavelengths given are those of the Sentinel-2B satellite, the values for Sentinel-2C satellite can differ slightly. Also note that the bandwidth given are the values measured at Full Width Half Maximum and the centre wavelength is the weighted average wavelength of the spectral response function of the sensor. Band 10 has been omitted as this is the cirrus band which does not contain any surface information. The following abbreviations are used: Near Infra-Red (NIR), Visible and Near Infra-Red (VNIR) and Short-Wave Infra-Red (SWIR). The bands in the table are also depicted in Figure 2.2

Band number	Centre wavelength (nm)	Bandwidth (nm)	Spatial resolution (m)	Spectrum name or detection aim
1	442.2	20	60	Aerosols
2	492.3	65	10	Blue
3	558.9	35	10	Green
4	664.9	31	10	Red
5	703.8	15	20	VNIR
6	739.1	14	20	VNIR
7	779.7	20	20	VNIR
8	832.9	115	10	NIR
9	943.2	20	60	Water vapour
11	1610.4	93	20	SWIR
12	2185.7	181	20	SWIR

Table B.3: Scene classification layer (SCL) of the Sentinel-2 surface reflectance products [51]. The SCL has a spatial resolution of 20 m.

Value	Name	Description
0	NO_DATA	No data
1	SATURATED_DEFECTIVE	Saturated or defective pixel
2	DARK_AREA_PIXELS	Dark area pixels (e.g., shadows)
3	CLOUD_SHADOWS	Cloud shadows
4	VEGETATION	Vegetation
5	NOT_VEGETATED	Not vegetated (bare soils, rocks)
6	WATER	Water (ocean, lakes, rivers)
7	UNCLASSIFIED	Unclassified
8	CLOUD_MEDIUM_PROB	Cloud medium probability
9	CLOUD_HIGH_PROB	Cloud high probability
10	THIN_CIRRUS	Thin cirrus
11	SNOW_ICE	Snow or ice

Google Earth Engine Sentinel-2 Surface Reflection Collection

From 2022-01-25 onward the processing baseline of Sentinel-2 changed. This resulted in a offset for the the new surface reflectance scenes of +0.1 spectral reflectance or +1000 digital number. As to provide a continuous dataset, correcting the offset, for analyses spanning over 2022-01-25, GEE provides the "COPERNICUS/S2_SR_HARMONIZED" dataset. This dataset was used for the albedo change model.

C

Albedo Determination Method

Albedo determination methods

Table C.1: Albedo estimation methods considered for this research. The methods are compared on albedo spectral range, required inputs and the ease of use.

Name	Liang [34]	Tasumi et al. [35]	Li et al. [36]	Bonafoni et al. [37]
Year	2001	2008	2018	2020
Satellite	Landsat 7	Landsat 7	Sentinel 2	Sentinel 2
Method	Statistical, regression	Physical, radiative transfer model	Statistical, regression	Physical, Solar power fraction
Albedo spectral range end product	Broadband shortwave	Entire shortwave spectrum	Visible and near-infrared broadband	Broadband shortwave
Additional input required	None	Air-humidity and digital elevation model	BRDF parameters	Resolution enhancement package
Comment	-	Low haze, cloud free conditions with a sensor view angles less than 20°.	Developed for 20 m resolution albedo.	Resolution enhancement package is outdated.

SURFRAD stations

Table C.2: Station information on the SURFRAD network stations used in this study. All station are located in the United States [61].

Code	Station Name	Latitude	Longitude	Elevation (m)	Installation date
bon	Bondville, Illinois	40.05155	-88.37325	230	April 1994
tbl	Table Mountain, Colorado	40.12557	-105.23775	1689	July 1995
dra	Desert Rock, Nevada	36.62320	-116.01962	1007	March 1998
fpk	Fort Peck, Montana	48.30798	-105.10177	634	November 1994
gwn	Goodwin Creek, Mississippi	34.25470	-89.87290	98	December 1994
psu	Penn State Univ., PA	40.72033	-77.93100	376	June 1998
sxf	Sioux Falls, South Dakota	43.73431	-96.62334	473	June 2003

The Surface Radiation Budget Network (SURFRAD) is a U.S.-based network of seven ground stations established in 1993 to provide accurate, continuous, long-term measurements of the surface radiation budget in support of climate research and satellite validation [61]. The stations are located in climatologically diverse regions across Montana, Colorado, Illinois, Mississippi, Pennsylvania, Nevada, and South Dakota, chosen to represent a wide range of U.S. climates and relatively homogeneous land surfaces. The stations are summarised in Table C.2. Each station independently measures upwelling and downwelling solar and infrared radiation, along with ancillary meteorological and spectral observations, producing a complete surface radiation budget. Data are quality controlled and distributed in near real time. Measurement are perfomed each minute. In Figure C.1 a schematic of the measurement setup is shown. Measurement of upwelling radiation are preformed from a 10 m high tower. On the other hand, measurement of downwelling radiation are preformed from a platform at approximately 1.5 m height, to prevent shading.

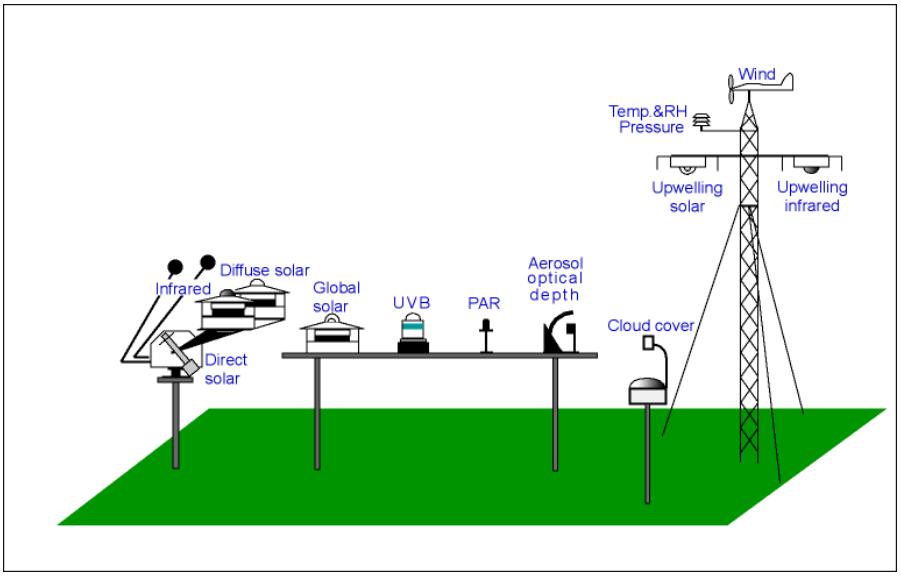

Figure C.1: Schematic of SURFRAD mearument station set up. Downwelling solar radiation is measured from a 10 m high tower. Upwelling solar radiation is measured from an approximately 1.5 m high platform. Image taken from the SURFRAD overview page [61].

Interpolation Methods

In Google Earth Engine (GEE), three reprojection methods are available. Figure C.2 provides a conceptual illustration of these three methods. Each pin in the figure represents the centre of a pixel, and the black pin marks the new pixel value that is to be determined. The first reprojection method, which is the default option in GEE, uses nearest-neighbour resampling [92]. This method simply assigns each new high-resolution pixel the value of the original pixel whose centre lies closest to it. The second reprojection method uses bilinear interpolation. In this method the surrounding pixels are used to determine a linear relationship onto which the new pixel values are projected. Finally, the third method uses bicubic interpolation to reproject the pixel values. In this case, the surrounding pixels are used to determine a cubic relationship, onto which the new pixel values are mapped. As illustrated in Figure C.2, cubic interpolation requires more neighbouring pixels to establish a relationship than the other two methods. Consequently, a buffer zone around the region of interest is necessary to accommodate all three reprojection methods.

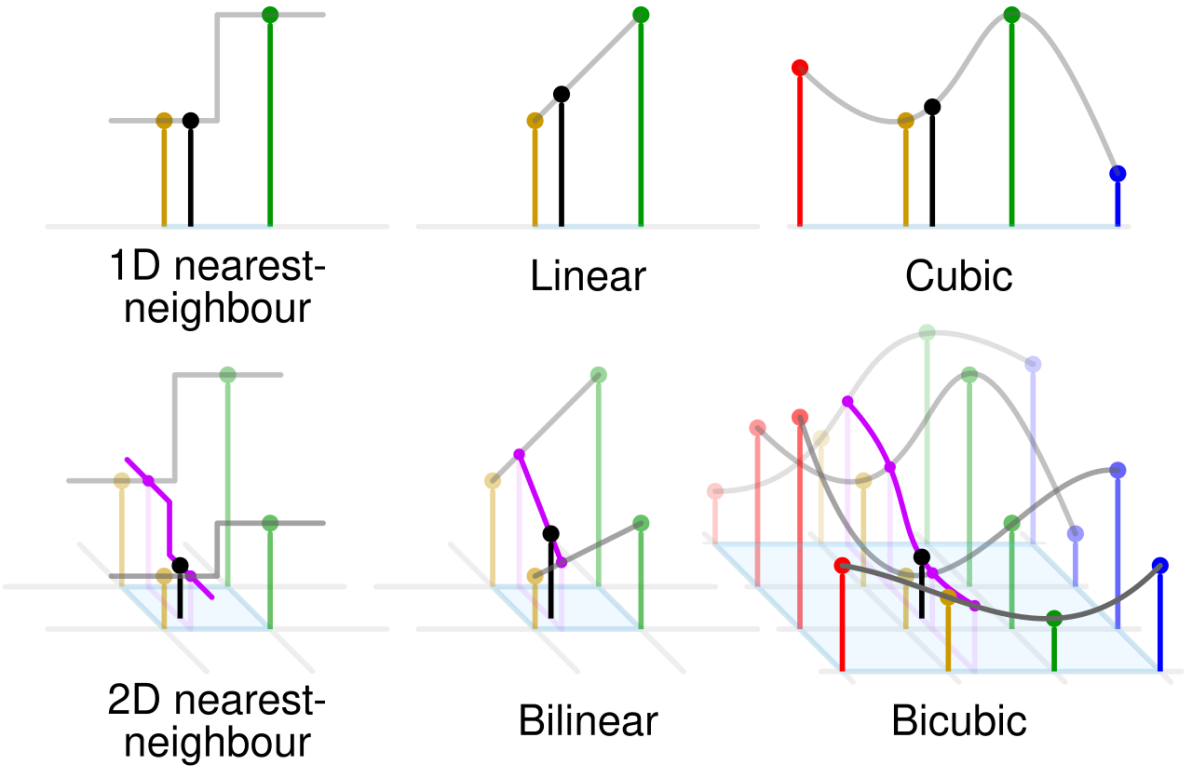

Figure C.2: Image illustrating nearest neighbour, bilinear and bicubic interpolation in 1D on the top row and 2D on the bottom row. Each pin indicates the value of a pixel. The black pin indicates the new pixel value to be determined. [93]

RMSE, Bias & Correlation Coefficient

The root mean square error (RMSE) was computed as:

$$\text{RMSE} = \sqrt{\frac{1}{n}\sum_{i=1}^{n}\left(\hat{y}_i - y_i\right)^2} \tag{C.1}$$

The bias was computed as the mean error between predictions and observations:

$$\text{Bias} = \frac{1}{n}\sum_{i=1}^{n}\left(\hat{y}_i - y_i\right) \tag{C.2}$$

The linear association between predictions and observations was quantified using the Pearson correlation coefficient:

$$R = \frac{\sum_{i=1}^{n}\left(\hat{y}_i - \overline{\hat{y}}\right)\left(y_i - \overline{y}\right)}{\sqrt{\sum_{i=1}^{n}\left(\hat{y}_i - \overline{\hat{y}}\right)^2}\sqrt{\sum_{i=1}^{n}\left(y_i - \overline{y}\right)^2}} \tag{C.3}$$

The parameters and variables in equations C.1–C.3 are as follows:

- n is the number of paired observations.
- $\hat{y}_i$ is the predicted value for the i-th observation.
- y_i is the observed (reference) value for the i-th observation.
- $\overline{\hat{y}}$ is the mean of the predicted values.
- $\overline{y}$ is the mean of the observed values.

D

PV Dataset

PV farm datasets

Table D.1: PV datasets considered in this study. The datasets are evaluated based on their update frequency, total detected capacity, minimum detectable system size, data accessibility, and whether they include information on installation date.

Name	Wiki-Solar [41]	Kruitwagen [42]	Global Renewables Watch [64]	TransitionZero [94]
Date	2012–2025	2018	2018–2024	2017–2025
Updates	Monthly	Snapshot	Quarterly, not any more	Yearly till 2022, now quarterly
Data source	Local organisations and government	Satellite data	Satellite data	Satellite data
Total capacity	$1,000GW_{AC}$	$423GW$	-	$1055GW_{AC}$
Minimal detection size	$> 4MW$	$> 10kW$	-	$> 500kW$
Number of sites	25 000	68 655	86 410	102 862
Accessibility	Behind Paywall	Publicly available	Available in an interactive map	Publicly available
Installation date information	Scheduled or actual coming-online date	Partly available	Construction date estimation	Installed before date for all locations
Comment	-	Most extensive of its time, not grouped	Claims open to the public, download not found	Pre-grouped, solar thermal facilities also

E

Albedo Climate Effect

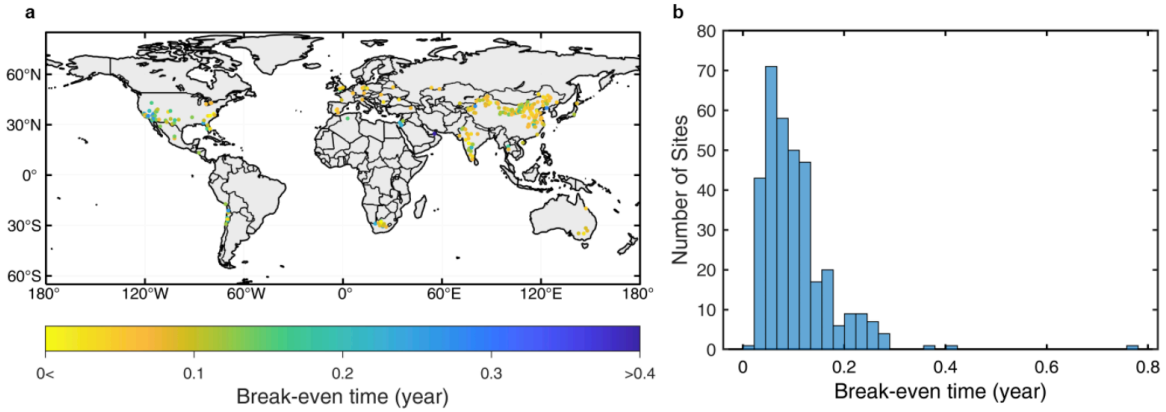

Figure E.1: Carbon break even time results reported by Wei et al. The spatial pattern of the sites and their break even times (a) and the frequency distribution histogram of the break even times. Only the positive values are shown. Figure for the supplementary materials [31].

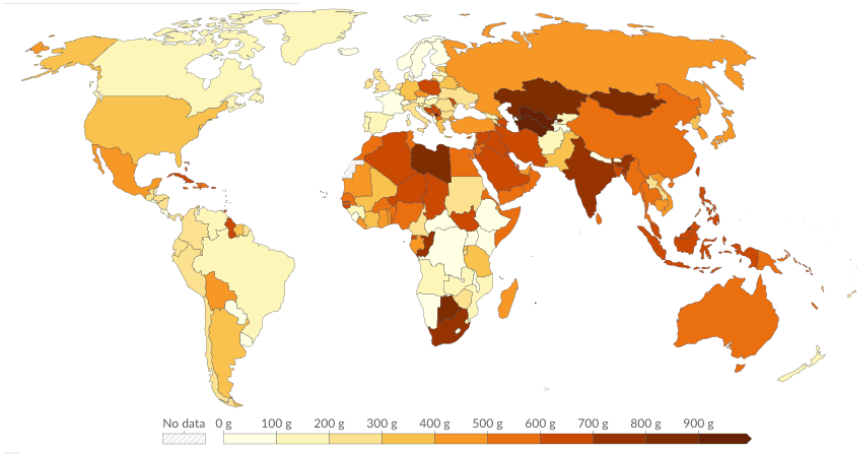

Figure E.2: Map indicating the local carbon intensity of electricity per country of 2024. Images from Our World in Data [82].